



PROCEEDING

**2022 3rd International Conference
on Applied Electromagnetic Technology**

AEMT

1-3 November 2022

Organized by:
**Center of Excellence in Science and Technology
"Geomagnetic", University of Mataram**



Technically co-sponsored by



2022 3rd International Conference on Applied Electromagnetic Technology (AEMT)




1-3 November 2022
Mataram, Indonesia

COPYRIGHT AND REPRINT PERMISSION:



This work is licensed under a Creative Commons Attribution-NonCommercial-NoDerivatives 4.0 International License. This license allows reusers to copy and distribute the material in any medium or format in unadapted form only, for noncommercial purposes only, and only so long as attribution is given to the creator.

CC BY-NC-ND includes the following elements:

- BY  - Credit must be given to the creator
- NC  - Only noncommercial uses of the work are permitted
- ND  - No derivatives or adaptations of the work are permitted

All rights reserved. Copyright ©2023 by PUI Geomagnetik



Table of Contents

Table of Contents	i
Sponsors & Contributors	iii
List of Committee	iv
Program	vii
Speech from Vice Rector	xiii
Speech from General Chair	xv
Keynote Speakers	xvi
Author Index	xxii
Evaluation of Earth's Magnetic Field Anomalies over Sembalun Geothermal Prospect Khilda Ayu Safitri, Teti Zubaidah*, Rosmaliati and Cipta Ramadhani	1-6
Time-frequency Analysis of Normal and Abnormal Lung Breath Sounds with Short-time Fourier Bulkis Kanata and Sabhan Kanata	7-13
Optimization of Patch E-Shape Array Microstrip Antenna 2.45 GHz Using Double Reflector Cahyo Mustiko Okta Muvianto, Buyung Satrya Anugrah, Suthami Ariessaputra and Sareh Malekpour	14-18
Detrended Fluctuation Analysis Associated with the M5.1 Earthquake Precursor in Banten, Indonesia Cinantya Nirmala Dewi, Febty Febriani, Titi Anggono, Syuhada, Aditya Dwi Prasetio, Mohammad Hasib, Hendra Suwarta Suprihatin, Suaidi Ahadi, Muhamad Syirojudin, Hasanudin, Indah Marsyam, Muhammad Nafian and Suwondo	19-24
LoRa Technology for Communication in Blankspot Areas L. Ahmad S. Irfan Akbar, Misbahuddin, Muhamad Syamsu Iqbal, A. Sjamsjiar Rachman, Djul Fikry Budiman and Giri Wahyu Wiriasto	25-29



The 3rd International Conference on Applied Electromagnetic Technology 2022

D-Vote: Decentralized Voting System Using Ethereum Blockchain	30-36
Darrell Yonathan, Galih Damar Jati, Geraldly Christanto, Kenya Damayanti, Jauzak Hussaini Windiatmaja and Riri Fitri Sari	
Clippo: a Speaker Clip on Mask	37-40
Erwin Sanjaya Loeminto and Felix Pasila	
NebulaX: A Therapeutic Mechanism Against Corona Virus	41-45
Felix Pasila*, Erandaru, Hestiasari Rante, Handry Khoswanto, Rhema Adhi and Henricus Soehartono	
Control System Design to Increase Low Voltage Ride Through (LVRT) Capacity in Wind Turbine Using STATCOM Base on Control Linear Quadratic Regulator (LQR)	46-50
Nurul Chairunnisa Noor, Indar Chaerah Gunadin and Ansar Suyuti	
Design of Sepic Converter for Renewable Energy System	51-55
Ratna Ika Putri, Ika Noer Syamsiana, Ferdian Ronilaya, Surya Nata and Septyana Riskitasari	
Business and Sociological Perspective Review for Smart Farming Application	56-60
Insani Sekar Wangi and Catur Apriono	
Clustering of the 2018 Lombok Earthquakes Using an Agglomerative Hierarchical Clustering Algorithm	61-65
Cipta Ramadhani, Abdullah Zainuddin, Abdul Natsir, Rosmaliati and Teti Zubaidah	
Calcium Carbonate Scale Inhibition Program on Two-Phase Geothermal Well in Indonesia	66-72
Nur Choiri Amin, Kuzey Karasu, Abdurahman Unal and Yasemine Tugce Yuksel	



The 3rd International Conference on Applied Electromagnetic Technology 2022

Sponsors



Contributors





List of Committee

General Chair

Dr. Rosmaliati, S.T., M.T. (University of Mataram, IEEE member)

Vice Chair

A. Sjamsiar Rachman, S.T., M.T. (University of Mataram, IEEE member)

Advisors

Prof. Ir. Bambang Hari Kusumo, M.Agr.St., Ph.D. (Rector, University of Mataram)

Dr. H. Zulkieflimansyah, S.E., M.Sc. (Governor of West Nusa Tenggara Province)

Yusron Saadi, S.T., M.Sc., Ph.D. (Vice Rector, University of Mataram)

Muhamad Ali, S.Pt., M.Si., Ph.D. (Head of LPPM, University of Mataram)

Zainal Abidin, M.Si (Head of Energy & Mineral Resources Office of West Nusa Tenggara)

Nuryanti, M.E. (Head of Industry Office of West Nusa Tenggara)

International Advisory Board

Prof. Mioara Manda (CNES, France/President of IAGA)

Dr. Monika Korte (GFZ Potsdam, Germany/Secretary General of IAGA)

Prof. Rashid Ansari (University of Illinois Chicago, USA/IEEE Life Fellow)

Prof. Taufik (Calpoly, USA/IEEE PES Chapter, Central Coast Section)

Prof. Katsumi Hattori (Chiba University, Japan)

Prof. Josaphat Tetuko Sri Sumantyo (Chiba University, Japan)

Dr. Makky Sandra Jaya (Petronas, Malaysia)

Dr. Wahyudi Hasbi (BRIN/LAPAN, Indonesia/Chair of IEEE Indonesia Section)

Prof. Kalamullah Ramli (Universitas Indonesia, Indonesia)

Prof. Riri Fitri Sari (Universitas Indonesia, Indonesia)

Prof. Fitri Yuli Zulkifli (Universitas Indonesia, Indonesia)

Prof. Eko Tjipto Rahardjo (Universitas Indonesia, Indonesia)

Dr. Yunus Daud (Universitas Indonesia, Indonesia/CEO NQ Geotechnology)

Prof. Sri Widiyantoro (Institut Teknologi Bandung, Indonesia)

Dr. Tumiran (Universitas Gadjah Mada, Indonesia)

Prof. Mauridhi Hery Purnomo (Institut Teknologi Sepuluh Nopember, Indonesia)

Prof. Gamantyo Hendrantoro (Institut Teknologi Sepuluh Nopember, Indonesia)

Prof. Adi Susilo (Universitas Brawijaya, Indonesia)

Prof. Hadi Suyono (Universitas Brawijaya, Indonesia)

Prof. Faizal Arya Samman (Universitas Hasanuddin, Indonesia)

Dra. Clara Y. Yatini (BRIN, Indonesia)

Febty Febriani, Ph.D. (BRIN, Indonesia)

Dr. Suaidi Ahadi (BMKG, Indonesia)

Nenny Krisnawaty (Pertamina Hulu Mahakam)

Sotarduga Sahat Nainggolan (Pertamina Geothermal Energy)

Ardila Johan Erdiansyah (Pertamina Geothermal Energy)



The 3rd International Conference on Applied Electromagnetic Technology 2022

Steering Committee

- Muhamad Syamsu Iqbal, S.T., M.T., Ph.D. (Dean of Engineering Faculty, University of Mataram)
- Drs. Dedy Suhendra, M.Si., Ph.D. (Dean of Math. & Natural Sci. Faculty, University of Mataram)
- Baiq Rien Handayani, S.P., M.si., Ph.D. (Dean of Food Technology & Agro-industry, University of Mataram)
- Dr. A. H. Wahab Jufri, M.Sc. (Dean of Teaching & Education Sci. Faculty, University of Mataram)
- Prof. Ir. Muhammad Sarjan, M.Agr.CP., Ph.D. (Director of Postgraduate Program, University of Mataram)
- Prof. Buan Anshari, S.T., M.Sc.(Eng.), Ph.D. (LPPM, University of Mataram)
- Dr. Muhaimin, S.H., M.Hum. (University of Mataram)

Technical Program Committee

- Dr.rer.nat. Teti Zubaidah, S.T., M.T. (University of Mataram, IEEE member)
- Prof. Dr. Eng. I Gede Pasek Suta Wijaya, S.T., M.T. (University of Mataram, IEEE member)
- Dr. Misbahuddin, S.T., M.T. (University of Mataram, IEEE member)
- I Nyoman Wahyu Satiawan, S.T., M.Sc., Ph.D. (University of Mataram, IEEE member)
- Dr. I Made Ginarsa, S.T., M.T. (University of Mataram, IEEE member)
- Cahyo Mustiko Okta Muvianto, S.T., M.Sc., Ph.D. (University of Mataram, IEEE member)
- Dr. Warindi, S.T., M.Eng. (University of Mataram, IEEE member)
- Dr. Ir. I Ketut Wiryajati, S.T., M.T., IPU., ASEAN.Eng. (University of Mataram, IEEE member)
- I Wayan Sudiarta, Ph.D. (University of Mataram, IEEE member)
- Prof. Dr. Nasmi Herlina Sari, S.T., M.T. (University of Mataram)
- Prof. Sugiman, S.T., M.T., Ph.D. (University of Mataram)
- Prof. Akmaluddin, S.T., M.Sc.(Eng.), Ph.D. (University of Mataram)
- Prof. Ir. Didi S. Agustawijaya, M.Eng., Ph.D. (University of Mataram)
- Prof. M. Mirmanto, S.T., M.T., Ph.D. (University of Mataram)
- Prof. Dr. Erin Ryantin Gunawan, M.Si., Ph.D. (University of Mataram)
- Prof. Jauhar Fajrin, S.T., M.Sc.(Eng.), Ph.D. (University of Mataram)
- Ir. Heri Sulistiyono, M.Eng., Ph.D. (University of Mataram)
- Dr. Eng. Budi Irmawati, S.Kom., M.T. (University of Mataram)
- Dr. Mutiara Rachmat Putri (Institut Teknologi Bandung)
- Dr. Widya Utama (Institut Teknologi Sepuluh Nopember)
- Dr. Ing. Onny Setyawati, S.T., M.T. (Universitas Brawijaya)
- Dr. Islamul Hadi, S.Si., M.Si. (University of Mataram)
- Stephan Adriansyah Hulukati (Universitas Ichsan, Gorontalo)
- Fericandra (Fakultas Teknik Universitas Riau)
- Amiruddin (Politeknik Siber dan Sandi Negara)
- Dr. Lukman Rosidy (Sekolah Tinggi Teknologi Terpadu Nurul Fikri)
- Dr. Rima Tri Wahyuningrum (Universitas Trunojoyo Madura)



The 3rd International Conference on Applied Electromagnetic Technology 2022

Secretariat

Dwi Ratnasari, S.Kom., M.T.
Khilda Ayu Safitri, S.T.
Rizky Aulia Safitri (F1B019126)

Treasurer

Bulkis Kanata, S.T., M.T.
Nur Fitratunnisa (F1B019109)
Nur Afifah Syarifah (F1B019108)

Seminar

Made Sutha Yadnya, S.T., M.T.
Agung Budi Muljono, S.T., M.T.
I Made Ari Nrartha, S.T., M.T.
Fitri Bimantoro, S.T., M.Kom.
Ari Hernawan, S.Kom., M.Sc.
Taufik Hidayat (F1B019136)
Ahmad Ray Surya Surenggana (F1B019013)

Workshop & Tour

Cipta Ramadhani, S.T., M.Eng.
Paniran, S.T., M.T.
Dr. Hiden, S.Si., M.Si.
Dr. Suhayat Minardi
Dr.rer.nat. Kosim, M.Si.
Muhammad Irsal FajriEfendy (F1B019097)
Zulfikar (F1B019147)

Sponsorship & Exhibition

Abdullah Zainuddin, S.T., M.T.
Syafaruddin Ch., S.T., M.T.
Eko Pradjoko, S.T., M.Eng., Ph.D.
Ramdani Saputra (F1B108055)
Insan Adhibuana Priyatna (F1B019073)
Arif Hakam Hidayat (F1B019026)
Frederick Benaya Situmorang (F1B019057)



The 3rd International Conference on Applied Electromagnetic Technology 2022

Program

Seminar: Tuesday, 1st November 2022

Time (UTC +8)	Agenda	Speaker(s)	Place
08.30 – 10.00	Workshop on Geothermal Exploration	Dr. Yunus Daud (NewQuest Geotechnology) Moderator: Dr. Atas Pracoyo	Ball Room Lombok Raya Hotel &
10.00 – 10.30	Coffee Break		
10.30 – 12.00	Workshop on Geomagnetic Equipment	Dr. Marhaban Sigalingging (PT Mitra Intimarga) Moderator: Mr. Cipta Ramadhani	Zoom Virtual Room: https://bit.ly/AEMT22_Workshop
12.00 – 13.00	Lunch		Resto Lombok Raya Hotel
13.00 – 13.05	Opening Ceremony	MC: Ms. Elise van Wijngaarden & Ms. Arnie Jasmin Johar	Ball Room Lombok Raya Hotel &
13.05 – 13.15	Recitation of Qur'an	The Winner of E-Fest 2022	
13.15 – 13.25	Speech from General Chair	Dr. Rosmaliati	Zoom Virtual Room: https://bit.ly/AEMT22_Opening
13.25 – 13.35	Speech from Chair of IEEE Indonesia Section	Dr. Wahyudi Hasbi	
13.35 – 13.45	Speech from Rector of University of Mataram	Prof. Ir. Bambang Hari Kusumo, M.Agr. St., Ph.D.	
13.45 – 14.00	Speech & Opening by Governor of West Nusa Tenggara Province	Dr. H. Zulkieflimansyah, S.E., M.Sc.	
14.00 – 14.05	Prying	Mr. Suthami Aries Saputra	
14.05 – 14.15	Performance of Local Culture (Asih Tresna Traditional Dance)	Sentras	
14.15 – 15.30	Plenary Session 1 New technologies in geothermal exploration & resource assessments Earth's magnetic fields are evolving Magnetic fields of our planet: a deep insight from space	Moderator: Dr. Teti Zubaidah Dr. Yunus Daud (NewQuest Geotechnology) Dr. Monika Korte (GeoForschungsZentrum Potsdam, Germany) Prof. Mioara Mandaia (CNES, France)	
15.30 – 16.00	Coffee Break		
16.00 – 18.00	Parallel Sessions	10 papers/room	
18.00 – 19.00	Dinner & Platinum Sponsor Presentation		Resto Lombok Raya Hotel



The 3rd International Conference on Applied Electromagnetic Technology 2022

Time (UTC +8)	Agenda	Speaker(s)	Place
19.00 – 20.15	<p>Plenary Session 2</p> <p>Advances on materials for electric vehicular renewable technologies</p> <p>Electromagnetics and our future generation of wireless system: a reflection of research & innovation</p>	<p>Moderator: Dr. I Nyoman Wahyu Satiawan</p> <p>Dr. M.V. Reddy (Nouveau Monde Graphite, Canada)</p> <p>Prof. Danilo Erricolo, Ph.D. (University of Illinois Chicago, USA)</p>	<p>Ball Room Lombok Raya Hotel &</p> <p>Zoom Virtual Room: https://bit.ly/AEMT22_Plenary2</p>
20.15 – 20.30	<p>Closing Ceremony & Awards PIC: Mr. Made Sutha Yadnya</p>		

Scientific Tour: Wednesday-Thursday, 2 -3 November 2022

PIC: Mr. Abdullah Zainuddin & Mr. A. Sjamsiar Rachman

Day	Time (UTC +8)	Agenda (Tentatively)	Place
Wednesday, 2nd November 2022	08.00 – 11.00	Travelling from Mataram to Sembalun	Departure from Lombok Raya Hotel
	11.00 – 13.00	Trip to geothermal utilizations sites	Sembalun
	13.00 – 14.00	Lunch	Bumbung Village
	14.00 – 15.30	Trip to geothermal utilizations sites	Sajang Village
	16.30 – 17.00	Presentation: Preliminary Results of Geomagnetic Surveys over Sembalun Geothermal Prospect by Dr. Teti Zubaidah & Dr. Rosmaliati	Hotel Nusantara, Sembalun Lawang
	17.00 – 18.00	Discussion: Direct Use of Geothermal Energy for Sustainable Green Industry in Sembalun Moderator: Dr. Misbahuddin	
	18.00 – 19.00	Soft Dinner	
	19.00 - ...	Private agenda	
Thursday, 3rd November 2022	07.30 – 08.30	Breakfast & briefing	
	08.30 – 12.00	Trip to geothermal manifestation	Sebau Hot Spring
	12.00 – 15.00	Travelling from Sembalun to Mataram	Arrival at Lombok Raya Hotel



Schedule of Parallel Sessions

Breakout Room 1 (in-Person ORAL)

Moderator: Dr. Felix Pasila & Dr. Misbahuddin

Time (UTC +8)	Paper ID	Title	Authors
16.00 – 16.12	2897	Design of Sepic Converter for Renewable Energy System	Ratna Ika Putri, Ferdian Ronilaya, Ika Noer Syamsiana, Septyana Riskitasari and Surya Nata
16.12 – 16.24	0693	Calcium Carbonate Scale Inhibition Program on Two-Phase Geothermal Well in Indonesia	Nur Choiri Amin, Kuzey Karasu, Abdurahman Unal and Yasemine Tigce Yuksel
16.24 – 16.36	4113	Preliminary Results from Spatial Characterization of Tropical Rain Using Weather Radar Data	Made Yadnya, Gamantyo Hendrantoro, Achmad Mauludiyanto, Wayan Sudiarta, Enderwin Enderwin, Alif Adiyasa and Abdullah Ali
16.36 – 16.48	8713	Optimization Of Patch E-Shape Array Microstrip Antenna 2.45 GHz Using Double Reflector	Cahyo Mustiko Okta Muvianto, Buyung Satrya Anugrah, Suthami Ariessaputra and Sareh Malekpour
16.48 – 17.00	5607	NebulaX: A Therapeutic Mechanism Against Corona Virus	Felix Pasila, Hestiasari Rante, Erandaru Erandaru, Handry Khoswanto, Rhema Adhi and Henricus Soehartono
17.00 – 17.12	8741	Evaluation of Earth's Magnetic Field Anomalies over Sembalun Geothermal Prospect	Khilda Ayu Safitri, Teti Zubaidah, Rosmaliati Rosmaliati and Cipta Ramadhani
17.12 – 17.24	6534	Lora Technology for Communication in Blankspot areas	L. Ahmad S. Irfan Akbar, Misbahuddin Misbahuddin, Muhamad Syamsu Iqbal, A. Sjamsjiar Rachman, Djul Fikry Budiman and Giri Wahyu Wiriasto
17.24 – 17.36	0737	Clippo: a Speaker Clip on Mask	Erwin Sanjaya Loeminto and Felix Pasila
17.36 – 17.48	3792	Clustering of the 2018 Lombok, Indonesia Earthquakes using Agglomerative Hierarchical Clustering Algorithm	Cipta Ramadhani, Abdullah Zainuddin, Abdul Natsir, Rosmaliati and Teti Zubaidah
17.48 – 18.00	8927	D-Vote: Decentralized Voting System Using Ethereum Blockchain	Darrell Yonathan, Galih Damar Jati, Gerald Christanto, Kenya Damayanti, Jauzak Hussaini Windiatmaja and Riri Fitri Sari
18.00 – 18.12	6256	Distance Estimation Model Based on RSSI Using Outdoor Propagation Model	Abdullah Zainuddin, Misbahuddin and Irsan Taufik Ali



The 3rd International Conference on Applied Electromagnetic Technology 2022

Breakout Room 2 (Virtual ORAL)

Moderator: Dr. Sabhan Kanata & Ms. Bulkis Kanata

Time (UTC +8)	Paper ID	Title	Authors
16.00 – 16.15	6301	Detrended fluctuation analysis associated with the M5.1 earthquake precursor in Banten, Indonesia	Cinantya Nirmala Dewi, Febty Febriani, Titi Anggono, Syuhada Syuhada, Aditya Dwi Prasetio, Mohammad Hasib, Hendra Suwarta Suprihatin, Suaidi Ahadi, Muhamad Syirojudin, Hasanudin Hasanudin, Indah Marsyam, Muhammad Nafian and Suwondo
16.15 – 16.30	4960	Evaluation Method for Selection of OATS Location for EV Radiated Emission Measurement Based on Electromagnetic Field Scanning	Arief Rufiyanto, Reza Septiawan, Gamantyo Hendrantoro, Budi Sulistya, Eko Setijadi and Risnanda Saputra
16.30 – 16.45	3322	Time-frequency Analysis of Normal and Abnormal Lung Breath Sounds with Short-time Fourier	Bulkis Kanata and Sabhan Kanata
16.45 – 17.00	BREAK		
17.00 – 17.15	3811	Control System Design to Increase Low Voltage Ride Through (LVRT) Capacity in Wind Turbine Using STATCOM Base on Control Linear Quadratic Regulator (LQR)	Nurul Chairunnisa Noor, Indar Chaerah Gunadin and Ansar Suyuti
17.15 – 17.30	4649	Business and Sociological Perspective Review for Smart Farming Application	Insani Sekar Wangi and Catur Apriono
17.30 – 17.45	1195	Low Level Laser Technology (LLLT) to Reduce Dependency Substance Nicotine on Cigarette for Student at the University of Mataram	M. Ahleyani, I Made Bayu Suarjaya and Teti Zubaidah
17.45 – 18.00	3682	Analysis the Effect of Electric Current on Induction Magnetic Field Coils	Gladys Fouriza Ibanez, Ergi Putra Febtiawan and Rosmaliati Rosmaliati



The 3rd International Conference on Applied Electromagnetic Technology 2022

Breakout Room 3 (in-Person POSTER)

Moderator: Mr. Erlan Taneza

Time (UTC +8)	Paper ID	Title	Author(s)
16.00 – 16.20	0001	Exploration of Geothermal Potential in Blawan – Ijen, East Java	Muhammad Riezqul Fikri
16.20 – 16.40	0002	Kamojang Geothermal Power Plant: 37 Years in Operation	Erlan Taneza
16.40 – 17.00	0003	Ulumbu Geothermal for Future Clean Energy in East Nusa Tenggara	Muhammad Irsal FajriEfendy
17.00 – 17.20	0004	Exploration and Development of Dieng Geothermal Power Plan in Central Java	Tizar Sepli Abiyusani
17.20 – 17.40	0005	Exploration and Utilization of Geothermal Energy in Hu'u – Daha Geothermal Working Area, Dompu District	Zulfikar
17.40 – 18.00	0006	Sorik Marapi in North Sumatra Geothermal Working Area	Multahadi



The 3rd International Conference on Applied Electromagnetic Technology 2022

Breakout Room 4 (Virtual POSTER)

Moderator: Ms. Dwi Ratnasari

Time (UTC +8)	Paper ID	Title	Authors
15.30 – 15.40	5166	Health Risks of Electromagnetic Field	Lalu Alaudin Ibnu Tajuddin Faqih, Deonaldo Setiawan Aninfeto and Teti Zubaidah
15.40 – 15.50	7083	Analysis Design and Materials of Inductive Sensor	Farhan Ahmad Suharyadi, Iffah Fikriana Al Nurin and Bulkis Kanata
15.50 – 16.00	6226	Application of Resistive Sensors in the sector of Environment, Health, and Technology	Fatur Rahman, Fitriatul Karimah and A. Sjamsjiar Rachman
16.00 – 16.10	3243	Liquid Crystal Display with Photolithography	Dion Pratama Putra, Dhafin Rizky Aldino and Bulkis Kanata
16.10 – 16.20	3628	Capacitive Sensors and Their Use	Lalu Efry Bani Akhry, Lutvi Alwan and Made Sutha Yadnya.
16.20 – 16.30	3902	RFID system	Dwi Juliadi Kusumayadi and M. Akbar Alamsyah
16.30 – 16.40	9851	The Effect of LED Lighting on Skin Health (The occurrence of skin hyperpigmentation)	Eny Maryani, Firdaus Romadhan and Cipta Ramadhani
16.40 – 16.50	BREAK		
16.50 – 17.00	8756	A Study the feasibility of automated data labelling and training using an EMF sensor in NILM platform	M. Irdani Syafari Fiddin and I Made Gita Yoga
17.00 – 17.10	9328	Easier Business with Barcode	Maulana Ridho Alfarizqa, Malik Gading Dirgantara and Dwi Ratnasari
17.10 – 17.20	2047	Superconducting Quantum Interference Device (SQUID) Magnetometer	Moh. Aryan Hastadi, M. Alan W G Sya'Ban and Paniran Paniran
17.20 – 17.30	5235	Implementation of Advance Photovoltaic Technology	Kevin Asgaryansyah, Lalu Muhammad Daffa Adyfar and Rosmaliati Rosmaliati
17.30 – 17.40	5058	Utilization of Electromagnetic Radiation in Cancer Treatment	M. Fajar Wirayudha, Esas Rahmat Muharam and Abdullah Zainuddin
17.40 – 17.50	4943	Drying Turmeric Using Microwave Ovens	Dony Anggara, Mochamad Dary Rochmany and Dwi Ratnasari
17.50 – 18.00	6604	Magnetic Technology for Medical Application	Diva Septiawan, Intan Novita Sari and Abdullah Zainuddin



Speech from Vice Rector University of Mataram



Distinguished guests, keynote speakers, participants, ladies and gentlemen

First of all, I would like to express my warm welcome to the 3rd International Conference on Applied Electromagnetic Technology (AEMT) 2022). It is very nice to have you all in this exciting conference. Surely, this international conference will provide an excellent opportunity for sharing knowledge and results in theory and methodology of magnetic field observation

and new technologies in geothermal exploration.

I notice that the aim of the conference is to provide a platform to researchers and practitioners from both academia as well as industry to meet and share cutting-edge development in the fields of geothermal exploration and magnetic field observation. Through the theme of this conference, which is "Geomagnetic and Geothermal Technology for Recovery of Sustainable Life Quality on a Green Planet", we can expect that the development of magnetic field observations and geothermal exploration will be increasingly recognized by various groups and will lead to scientists, practitioners and industry to joint together in developing this sector.

Distinguished guests, keynote speakers, participants, ladies and gentlemen

Intense interest from participants who will be presenting papers on new technologies or research findings in the chosen field is a clear signal that there will be a positive impact from this event. It is expected that the conference will create wider collaboration and enable new technologies, assessment of geothermal resources and information related to the earth's magnetic field to be widely disseminated. The collaboration that means seeking external organizations to create partnerships and alliances, allow co-sharing information and R&D sources to gather the potential of existing knowledge to finally configure the new technologies at a larger scale.



The 3rd International Conference on Applied Electromagnetic Technology 2022

We must seize the advantages and exciting opportunities of this international conference to make it beneficial in the development of society at large. I believe this event can generate discussions and recommendations and turn a theory-based approach into a real work as in this modern era there is a strong emphasis on applying the results of thought.

Finally, I would like to express my sincere thanks and appreciation to organizers, partners, keynote speakers and the sponsors who contribute to this event. To all participants who have come from different countries, I would like to extend my very warm welcome to this conference. I wish you all have a productive and fruitful discussion.

Mataram, 1st November 2022

Yusron Saadi
Vice Rector for Planning, Collaboration and Information System, Universitas Mataram



Speech from General Chair



Assalamualaikum Warahmatullahi Wabarakatuh.

I thank Allah S.W.T. for the blessings of health and the opportunity for all of us to be present at today's meeting.

Good morning, distinguished guests ladies and gentlemen. Thank you to each and every one of you for being here with us today. My name is Rosmaliati. It is such an honor for me to speak on behalf of the Committee. Let me begin by giving you

a warm welcome to the 3rd Applied Electromagnetic Technology international conference (3rd AEMT).

Before we get started, I would like to express my appreciation to all those who have supported this event: Mr. Rector and Vice Rector, Head of Research Institute and Community Service (LPPM), Mr. Dean Faculty of Engineering, Head of Electrical Engineering Department University of Mataram who have provided funding and facilities.

I convey high appreciation to Dr. Daud Yunus, Prof. Mioara Manda, Dr. Monika Korte, Prof. Danillo Erricolo, Dr. MV Redy as keynote speaker, Dr. Marhaban from PT. Mitra Intimarga, Bank BTN, and IEEE Indonesia Section as sponsors, as well as the Government of West Nusa Tenggara Province.

I also wish to thank all the committee members who together made the conference possible. Last but not least, we would like to thank all the contributors and reviewers who made this conference possible.

As one of the largest universities in the province, the University of Mataram, in particular the Center of Excellence (PUI) for geomagnetics, plays a role in realizing the government's program to achieve the net zero emission target. Therefore, this conference aims to bridge a meeting between experts, researchers at universities, local governments, industry, and other stakeholders under the theme of "Geomagnetic and Geothermal Technology for Recovery of Sustainable Life Quality on a Green Planet".

The 3rd AEMT will focus more on efforts to explore and use geothermal potentials, especially in the Sembalun area of Lombok. Therefore, in this conference, we carried out a series of activities in the form of workshop, which is started this morning, continued with a conference, and tomorrow will end with a scientific tour of the Sembalun area. In the tour, we will be visiting geothermal manifestations on the slopes of Mount Rinjani and several local community industries that will utilize geothermal potentials.

Well, I do not want to take too much of your time. Thank you for being here with us. We value your presence at this conference. Please enjoy the conference.



Keynote Speakers



Dr. Monika Korte

*Secretary General of International Association of
Geomagnetism and Aeronomy/IAGA*

*Interim Head of the Geomagnetism Section of German
Research Center for Geosciences (GFZ Potsdam),
Germany*

- Her main research interest is the evolution of the geomagnetic core field on all time scales. She has worked with observational and paleomagnetic data to model the field and its secular variation, and she is also interested in the separation of magnetic field sources and lithospheric magnetic field signatures.
- From 2003 to 2014 she was scientific head of the Adolf-Schmidt-Observatory for Geomagnetism of GFZ in Niemegk and later led the group dealing also with the international collaborative and supported observatories of GFZ, including the Lombok Geomagnetic Observatory in Indonesia. She has been involved in collaborative geomagnetic repeat station surveys in Germany, Europe and Southern Africa. Her research interests mainly cover the geomagnetic core field and its evolution on all time scales, but also the separation of internal field secular variation and long term magnetospheric variations. She is also interested in the lithospheric field on the side.
- Since her time as a post-doctoral research fellow of Alexander von Humboldt-foundation at Scripps Institution of Oceanography, University of California at San Diego in 2001-2002, she has been interested in the reconstruction of the global long-term magnetic field evolution, from Holocene time-scales to geomagnetic excursions, using archeo- and paleomagnetic data.
- She authored in topic(s): Earth's magnetic field & Secular variation, and has an h-index of 30, co-authored 103 publication(s) receiving 4731 citation(s).

Evolution of Earth's magnetic field

Earth's magnetic field varies on a broad range of time scales. While fast variations generally have their sources in electrical current systems around Earth, the main field generated in Earth's core evolves over time-scales from months to millions of years. This presentation focusses on the geomagnetic field evolution on scales beyond the observational era, i.e. centuries and longer. First, an overview is provided over characteristics of archeo- and paleomagnetic data, i.e. the materials that provide information about the field variations on these time-scales. Then, it is discussed how the full global view of the long-term changes can be obtained. This is important for two reasons: a) The underlying magneto-hydrodynamic processes in Earth's outer core that need to be understood to predict the future magnetic field evolution can only be studied in a global perspective. b) The geomagnetic field creates the magnetosphere, which plays an important role to shield our habitat against space weather influences, and which also only can be studied when knowing the global field configuration. New results concerning the global view on geomagnetic field excursions, particularly the Laschamps excursion 41 000 years ago, are discussed. Finally, the presentation briefly touches on full polarity reversals, and on archeomagnetic dating as an interdisciplinary application of good knowledge of geomagnetic field evolution.



The 3rd International Conference on Applied Electromagnetic Technology 2022



Prof. Mioara Mandea

President of International Association of Geomagnetism and Aeronomy/IAGA

*Centre National d'Etudes Spatiales (CNES)/
French Space Agency, France*

- President of International Association of Geomagnetism and Aeronomy/IAGA and Chair of the Outreach Committee of European Geosciences Union.
- She was also President of the Geophysical Maps Commission of the Commission for the Geological Map of the World, and Chair of the Education Award Committee of AGU.
- Mioara Mandea has a broad international education and has worked with geosciences institutions and universities in Romania, France, and Germany.
- She graduated in Engineering in Geology and Geophysics from the University of Bucharest, obtaining doctorates from the University of Bucharest in geophysics and geophysical prospecting and from the IPGP France in internal geophysics. She received the Habilitation from the University Paris VII in 2001.
- She has been granted the Van Straelen prize (French Geological Society), the Hepites Prize (Romanian Academy), Medal Slovak Academy of Sciences, AGU International Award, Chevalier de l'Ordre National du Mérite, and Petrus Peregrinus Medal from EGU. She is Member of Academia Europea, Member of Academie Royale de Belgique, Member of Russian Academy of Science, and is also a Titular Member of the Academy of Romanian Scientists. Mioara Mandea's research interests mainly concern measuring, mapping, and understanding the multitude of magnetic fields encountered in near-Earth and near Earth-like planets. She has concentrated her work in some major directions, participating in the general effort of measuring Earth's magnetic field from the ground to space, developing new tools to model the geomagnetic field and its secular variations (with a special emphasis on geomagnetic jerks), or using the geomagnetic information to determine physical properties in the deep Earth's interior (with special studies on the lower mantle conductivity or motions at the core-mantle boundary). Her fields of research also include geopotential field mapping, on global or regional scales, with important implications for the understanding of rapid changes within the Earth's system.
- Mioara Mandea has published more than 255 papers, books, and chapters in books, and has been involved in organizing more than 50 workshops and conferences.
- She has supervised 11 worldwide PhD students (France, Germany, US, Romania, Croatia, Algeria, Indonesia, and Portugal).



The 3rd International Conference on Applied Electromagnetic Technology 2022



Prof. Danilo Erricolo

*Professor and Director of Graduate Studies
Department of Electrical and Computer Engineering
University of Illinois at Chicago
Chicago, IL, USA*

Publication Topics: electromagnetic wave scattering, inverse problems, iterative methods, permittivity, UHF filters, antenna radiation patterns, beam steering, image reconstruction, leaky wave antennas, liquid crystals, microstrip filters, notch filters, optimisation, radiofrequency imaging, resonator filters, split ring resonators, varactors, MIMO communication, Markov processes, Monte Carlo methods, UHF resonators, antenna phased arrays, approximation theory, autonomous aerial vehicles, buildings (structures)

Biography

Danilo Erricolo (Fellow, IEEE) received the Laurea degree of Doctor (*summa cum laude*) in electronics engineering from the Politecnico di Milano, Milan, Italy, in 1993, and the Ph.D. degree in electrical engineering and computer science from the University of Illinois Chicago (UIC), Chicago, IL, USA, in 1998. He is currently a Professor with the Department of Electrical and Computer Engineering, the Director of the Andrew Electromagnetics Laboratory, and an Adjunct Professor in bioengineering with UIC. In 2017, he was nominated as a University of Illinois Scholar. In summer 2009, he was an Air Force Faculty Fellow with the Air Force Research Laboratory, Wright-Patterson Air Force Base, Dayton, OH, USA. He has authored or coauthored more than 300 publications in refereed journals and international conferences. His research interests include the areas of antenna design, electromagnetic propagation and scattering, high-frequency techniques, wireless communications, electromagnetic compatibility, the computation of special functions, and magnetic resonance imaging. He was elected as a Full Member of Commissions B, C and E of the U.S. National Committee (USNC) of the International Union of Radio Science (URSI), and a Committee of the U.S. National Academies. He served as the Chair (2009–2011), the Vice Chair (2006–2008), and the Secretary of the USNC-URSI Commission E on Electromagnetic Environment and Interference (2004–2005). He was the Chair of the USNC-URSI Ernest K. Smith Student Paper Competition (2009–2014), the Vice-Chair of the Local Organizing Committee of the XXIX URSI General Assembly, Chicago, in August 2008, and a member at Large of USNC-URSI (2012–2017). He was the General Chairperson of the 2012 IEEE International Symposium on Antennas and Propagation and USNC-URSI National Radio Science Meeting, Chicago, in July 2012. He was an Elected Member of the IEEE AP-S Administrative Committee (2012–2014), the Chair of the IEEE AP-S Distinguished Lecturer Program (2015–2016), and the Chair of the Chicago Joint Chapter of the IEEE AP-S and Microwave Theory and Techniques Society (2011–2016). He has served on more than 50 conference technical program committees, chaired over 70 conference sessions, and organized more than 30 special sessions at international scientific conferences. He has been the Editor-in-Chief of the IEEE Transactions on Antennas and Propagation, since August 2016.



The 3rd International Conference on Applied Electromagnetic Technology 2022

Towards a smart electromagnetic environment

This is an exciting time for the field of antennas and propagation because the anticipated future generations of wireless systems are bringing closer together antenna perspectives with propagation aspects. Antennas are one of the key enabling elements in many devices that impact the daily lives of billions of people for applications that include communications, computing and sensing. The word antenna strictly refers to the radiator that launches a guided electromagnetic wave into the air. Traditionally, antenna engineers have been concerned with design challenges such as maximizing the radiation along a specific direction, while minimizing the side lobes.

The introduction of smart antennas caused the transition from antennas to antenna systems as the operation of the antenna is more intimately connected to the RF front end and the signal processing unit that processes and controls the signals received by and sent to the antenna. Multiple antenna systems, known as Multiple input multiple output (MIMO) systems, were introduced to increase the overall communication channel capacity. The increase in communication channel capacity was not associated with antennas, but rather with features of propagation phenomena. Specifically, under appropriate conditions, one can leverage the diversity of the electromagnetic field at different locations so that it is possible to extract more information and thus leading to higher communication channel capacity. From the antenna perspective, the design of multiple antenna systems is complicated by the fact that when antennas are in close proximity, mutual coupling among radiating elements must be taken into account.

Deeper understanding of propagation phenomena and antenna design is fundamental for Massive MIMO systems, where massive refers to the number of antennas being larger than the number of users. If sufficient diversity among the various physical propagation channels exists, it is possible to achieve higher gain than with ordinary MIMO systems. From the antenna perspective, dealing with a massive antenna system further complicates the challenges of MIMO system due to the large number of RF chains needed.

More recently, thanks primarily to the increased available computational power and higher demands for the quality of communication links, new research efforts are being devoted towards the creation of a smart electromagnetic environment. The novelty consists in achieving a holistic approach where the environment where propagation occurs, together with the wireless infrastructure and the users are all taken into account to improve the performance of the system by going beyond the standard concepts of wireless infrastructure and wireless channel. In fact, while traditional communication systems focus the radiated power along the terminal direction to maximize link quality and information transfer by, for instance, increasing the antenna gain and reducing the sidelobe level, next generation multi-user multi-antenna architectures could maximize the signal-to-noise-ratio by spatially distributing the power to constructively exploit the wave scattering phenomena in the multipath propagation environment, regardless of the gain, the sidelobe levels, or the grating lobes. As an example, for propagation in urban environments, the scattering scenario needs to be considered as an asset rather than an impediment. Accordingly, building walls may be seen as an opportunity to install intelligent reflective surfaces to improve coverage at locations that cannot be reached through direct line-of-sight-paths.



The 3rd International Conference on Applied Electromagnetic Technology 2022



Dr. Yunus Daud

*Head of Geothermal Research Center
Universitas Indonesia, Indonesia*

Founder of NewQuest Geotechnology

- He obtained his doctor degree in the field of Exploration Geophysics from the Department of Earth Resources Engineering, Kyushu University, Japan, with the dissertation title Geophysical Studies Over the Sibayak Geothermal Field (Indonesia).
- He is working in research, education and business-related to geothermal resources technology.
- He has been teaching and research supervising for undergraduate and graduate students at the University of Indonesia in the field of geothermal exploration technology, mainly electromagnetic, gravity, and MT methods, as well as geothermal systems and technology.
- He has been developing 7 (seven) geoscientific software with patents including GeoSlicer-X, a 3-D visualization software for geoscientists and engineers. He has also been giving training courses in geothermal exploration, especially 3-D magnetotelluric (MT) technology and resource assessment for geothermal company's staffs.
- In addition, He has been founding PT NewQuest Geotechnology and providing a consultant in geothermal exploration and development for geothermal industries.



The 3rd International Conference on Applied Electromagnetic Technology 2022



Dr. M.V. Reddy

Nouveau Monde Graphite, Canada

- Dr. M.V. Reddy obtained his Ph. D (2003) in the area of Materials Science and Engineering (with highest distinction) from the University of Bordeaux, France. From July 2003 to May 2019, he worked at the Department of Materials Science and Engineering, Chemistry and Physics, National University of Singapore (NUS), Singapore. June 2019 to Aug 2021, he had worked at the Centre of Excellence in Transportation Electrification and Energy Storage, Hydro-Québec, Canada. Currently working as a Senior Professional Researcher at Nouveau Monde Graphite (New graphite world) (NMG), Quebec, Montreal, Canada.
- Over the past 21 years, he has conducted leading research on Materials for Energy Storage (cathodes, anodes, supercapacitors and electrolytes), Materials processing & characterization, and the development of in situ techniques for Energy storage renewable technologies.
- Dr. Reddy has published 220 papers in various international journals. He has obtained an h-index of 68 with over 17000 citations. These have recently placed him within the top 2% highly cited researchers in Energy (world Ranking the 1002nd out of 186500 researchers) and Highly cited Researcher in Materials Science in Canada (National ranking:39)
- Dr. Reddy is serving as an editorial advisory board member in Materials Research Bulletin and Journal of Energy Storage (Elsevier, Scopus journal) as well as several open access journals
- Awards: Outstanding Science Mentorship Award (2010- 2018), and Inspiring Research Mentor Award (2011 to 2019), 2021 Battery Materials electrochemistry award from the Electrochemical Society of India, Indian Institute of Science (IISc), Bangalore, India.
- Invited life member in ICDD USA and given 150 talks at various conferences and workshops & FDP.
- Invited committee member in various international Research proposals, theses and conference organizations and visiting Professor at various Universities



Author Index

Adhi, Rhema	41
Ahadi, Suaidi	19
Akbar, L. Ahmad S. Irfan	25
Amin, Nur Choiri	66
Anggono, Titi	19
Anugrah, Buyung Satria	14
Ariessaputra, Suthami	14
Apriono, Catur	56
Budiman, Djul Fikry	25
Christanto, Geraldny	30
Damayanti, Kenya	30
Dewi, Cinantya Nirmala	19
Erandaru	41
Febriani, Febty	19
Gunadin, Indar Chaerah	46
Hasanudin	19
Hasib, Mohammad	19
Iqbal, Muhamad Syamsu	25
Jati, Galih Damar	30
Kanata, Bulkis	7
Kanata, Sabhan	7
Karasu, Kuzey	66
Khoswanto, Handry	41
Loeminto, Erwin Sanjaya	37
Malekpour, Sareh	14
Marsyam, Indah	19



The 3rd International Conference on Applied Electromagnetic Technology 2022

Misbahuddin	25
Muvianto, Okta Cahyo Mustiko	14
Nafian, Muhammad	19
Nata, Surya	51
Natsir, Abdul	61
Noor, Nurul Chairunnisa	46
Pasila, Felix	37, 41
Prasetio, Aditya Dwi	19
Putri, Ratna Ika	51
Rachman, A. Sjamsjiar	25
Ramadhani, Cipta	1, 61
Rante, Hestiasari	41
Riskitasari, Septyana	51
Ronilaya, Ferdian	51
Rosmaliati	1, 61
Safitri, Khilda Ayu	1
Sari, Riri Fitri	30
Soehartono, Henricus	41
Suprihatin, Hendra Suwarta	19
Suwondo	19
Suyuti, Ansar	46
Syamsiana, Ika Noer	51
Syirojudin, Muhamad	19
Syuhada	19
Unal, Abdurahman	66
Wangi, Insani Sekar	56
Windiatmaja, Jauzak Hussaini	30
Wiriasto, Giri Wahyu	25
Yonathan, Darrell	30
Yuksel, Yasemine Tugce	66
Zainuddin, Abdullah	61
Zubaidah, Teti	1, 61

Evaluation of Earth's Magnetic Field Anomalies over Sembalun Geothermal Prospect

Khilda Ayu Safitri
Dept. of Electrical Engineering
University of Mataram
Mataram, Indonesia
khildaayu.s@gmail.com

Teti Zubaidah*
Dept. of Electrical Engineering
University of Mataram
Mataram, Indonesia
tetizubaidah@unram.ac.id

Rosmalianti
Dept. of Electrical Engineering
University of Mataram
Mataram, Indonesia
rosmalianti@unram.ac.id

Cipta Ramadhani
Dept. of Electrical Engineering
University of Mataram
Mataram, Indonesia
ciptaramadhani@unram.ac.id

Abstract— This study uses geomagnetic data that has been taken around the Sembalun geothermal prospect, which was carried out separately in Sembalun Lawang and Sembalun Timba Gading Villages in 2019. Integration of the two data was carried out to obtain a combined map using Oasis Montaj Software, which can interpolate data and display the anomaly values between the two regions. Qualitative interpretation is carried out by analyzing the comparison of anomalous patterns obtained by reducing daily variations using two different data, i.e. data from the Nurul Bayan Station (NRB) in North Lombok and the Kakadu Observatory (KDU) in Northern Australia. The differences in anomalous patterns are shown, where the peak of positive anomaly is shifted about 250 meters. In addition, there are differences in the range of anomaly values, resulting from processing with NRB and KDU data. In this case, the reductions using data from NRB which is located closer to Sembalun is considered to give more valid results than using KDU data.

Keywords—geomagnetic, geothermal, energy, interpretation, anomaly, Sembalun

I. INTRODUCTION

Geothermal energy is one of the sources of energy that is produced and stored in the Earth. The process of geothermal formation is triggered by tectonic activity in the bowels of the earth. The existence of geothermal resources in Indonesia is associated with volcanic activity as a heat source associated with the movement of these tectonic plates. The magnitude of volcanic activity creates a large geothermal potential [1]. Along the path of volcanoes, geothermal energy reserves are very large and one of the alternative energy sources that are environmentally sound [2].

This research has been carried out in Sembalun area which shows the existence of geothermal potential. One area that has geothermal potential is located in the south-western part of Sembalun. The existence of geothermal potential in this area is closely related to volcanic rocks, which are the most possible structure for a geothermal reservoir system [3].

Based on research [4] Sembalun is an area that shows indications of geothermal potential through manifestations in the form of Sebau hot springs, Orok springs, and Sembalun Lawang altered rocks. The research was conducted through geological, geochemical and geophysical investigations.

The geophysical method used in this research is the geomagnetic method. The geomagnetic method is the most

appropriate method for interpreting the subsurface layer based on the measured magnetic field intensity. According to [5], the geomagnetic method is the recommended standard method and reference in geothermal exploration in international standards. The result of this method is an anomaly map that is used to determine variations in the magnetic field so that it can be associated with the geological structure of the existence of geothermal potential. In addition, the measurement accuracy of the geomagnetic method is relatively high and the field operations are relatively simple [6].

Previous research [7] identified that Lombok Island, especially in the Sembalun area, is a zone characterized by magnetic anomalies with very large intensity values. To find out the differences in magnetic anomalies for utilization of geothermal potential in Sembalun area, a systematic research is carried out that aims to identify the subsurface layer. In assisting the interpretation of geothermal potential, this study uses data from previous researches [8], [9]. Locations of previous studies are shown in Fig. 1.

Due to the limited amount of data available, the two data sets were combined to obtain a more comprehensive map. By using interpolation technique, it is expected that the two datasets can display anomaly values spreading between the two separated areas, with an accuracy range within a radius of 300 m. Based on [5], to distinguish between the anomaly value and the magnetic area in an area, the size of the survey area must exceed the expected size of the anomaly.

In addition, to identify differences in geomagnetic anomalies, one of the interesting objects to be investigated is comparing the results of data processing using two references (i.e. using data obtained from two different geomagnetic stations). This approach is useful to obtain a more accurate distribution of magnetic anomalies. In this research, we used data from Nurul Bayan Station (NRB) in North Lombok and Kakadu Observatory (KDU) in Northern Australia.

II. METHODS

A. Magnetic Field Data Filtration

Data obtained from [8] and [9] researches in 2019 have been tested for data normality using the One Sample Kolmogorov Smirnov Test on SPSS Software. The basis for decision making is the significance value (Sig). If $\text{Sig} \geq 0.05^\circ$, then the total magnetic field data is normally

distributed; whereas if $\text{Sig} < 0.05^\circ$, then the total magnetic field data is not normally distributed.

B. Geomagnetic Data Correction

1. Daily corrections is corrections made due to deviations in the value of the Earth's magnetic field due to time differences and the effects of radiation from the sun in one day. In making daily corrections, it is necessary to pay attention to adjusting the time in the measurement data on the server to the time at the measurement point.
2. IGRF correction is to eliminate variations in the Earth's internal magnetic field so that an anomalous magnetic field is obtained.

C. Magnetic Anomaly Calculation

Magnetic data measured at a location is a resultant of Earth's internal magnetic fields (IGRF), the lithospheric field (produced by magnetized crustal rocks), the influence of external fields (known as daily variation), and the influence of slow change in the core magnetic fields (known as secular variation) [10].

The daily corrected value (F_u) is calculated as the difference between the measured magnetic field value [$F_u(t)$] and the magnetic field value measured at each station [$F_s(t)$] and the average baseline value for each station (\bar{F}_s), as formulated in (1).

$$F_u = F_u(t) - [F_s(t) - \bar{F}_s] \quad (1)$$

The average daily corrected value can be calculated by sum up all daily corrected values (obtained during measurement) and divided by the number of data, as formulated in (2).

$$\bar{F}_u = \frac{\sum_{i=1}^n F_u}{n} \quad (2)$$

Magnetic anomaly can be calculated by subtracting the average daily corrected value with IGRF value, as formulated in (3). The IGRF value, can be accessed at www.ngdc.noaa.gov.

$$\text{Mag.Anomaly} = \bar{F}_u - F_{IGRF} \quad (3)$$

III. DATA AND ANALYSIS

A. Normalization of Data with SPSS Software

Table I shows the normalized result of the Kolmogorov Smirnov Test, which shows that point 13 magnetic field data in the Sembalun Lawang area is not normally distributed because the significance value of the total magnetic field intensity measurement data is 0.016° . To overcome the data that is not normally distributed, it can be done by eliminating outliers. Outliers are data whose nature can confuse statistical tests. Outlier data can be seen in the boxplot section. The output boxplot data can be seen in Fig. 2.

Fig. 2 indicate the data indicated as outliers. If the data is above, the box indicates extremely high data and if the data is below, the box indicates extremely low data. From the output above, it can be seen that subject numbers 1, 2, and 47 are indicated as outliers. We then deleted the data outliers,

and the data is again tested for normality with the One Sample Kolomogorov Smirnov Test. The results of the new Kolmogorov Smirnov Test can be seen in Table II.

Table II shows the normality results of the Kolmogorov Smirnov Test after the outliers are removed. A significance value of 0.054° is obtained, therefore it is said that the data has been normally distributed. The total field data is measured at point 13 Sembalun Lawang; before removing the outliers, had a total of 47 data points with a significance value of 0.016° , while after removing the outliers, the number of data points is 44 with a significance value of 0.054° , and categorized as good quality data.

B. Correction Value

Following the normality testing of all total magnetic field data, the next process was carried out using Microsoft Excel Software, namely the daily variation correction process. The corrected values are obtained by using data from the NRB Station with a baseline value of (F_s) = 44840.28 nT and the KDU Observatory with a baseline value of (F_s) = 46196 nT.

Daily corrections are made at each time of data collection (per minute) at each measurement point. This daily correction aims to eliminate the influence of external magnetic field. Daily variation corrections show a difference between results obtained using NRB Station and KDU Observatory data. The measured value at NRB Station is lower than that at the KDU Observatory, due to the difference in local time between both locations. For example, when measurements were made in the field, the local time in Sembalun and NRB was at 08:24 a.m., while the local time in Kakadu was at 09:54 a.m. (1 hours and 30 minutes earlier). The difference in the local times causes a difference in the measured intensity of magnetic field at two locations, mostly due to the difference in the intensity of Sun irradiance at the two locations.

TABLE I. OUTPUT OF KOLMOGOROF SMIRNOV TEST NORMALITY BEFORE OUTLIERS REMOVAL

One-Sample Kolmogotov-Smirnov Test		
N		47
Normal Parameters ^{a,b}	Mean	45657.1513
	Std. Deviation	1.74358
Most Extreme Differences	Absolute	.144
	Positive	.144
	Negative	-.112
Test Statistic		.144
Asymp. Sig. (2-tailed)		.016 ^c

TABLE II. OUTPUT OF KOLMOGOROF SMIRNOV TEST NORMALITY AFTER OUTLIERS REMOVAL

One-Sample Kolmogotov-Smirnov Test		
N		V2 44
Normal Parameters ^{a,b}	Mean	45657.0823
	Std. Deviation	1.38460
Most Extreme Differences	Absolute	.131
	Positive	.131
	Negative	-.107
Test Statistic		.131
Asymp. Sig. (2-tailed)		.054 ^c

The corrected value obtained using (1) at point 9 in Sembalun Lawang area at 09.04 (UTC) is 45165.9 nT with correction data from KDU, and 45162.49 nT with correction data from NRB. The average corrected value obtained using (2) at point 9 in Sembalun Lawang area is 45165.94 nT with KDU data, and 45161.6 nT with NRB data.

C. Magnetic Total Anomaly

The IGRF value at point 9 in Sembalun Lawang area is 44790.5 nT, as can be seen in Table III. From (3), it is found that the total magnetic anomaly at point 9 at 23:20 (UTC) with correction data from the KDU Observatory is 375,443 nT, while the total magnetic anomaly with correction data for NRB Station is 371,095 nT.

Magnetic field anomalies are often also referred to as local magnetic fields (crustal fields). Magnetic fields are generated by rocks containing magnetic minerals such as magnetite and titanomagnetite in the Earth's crust. Magnetic field anomalies are caused by remanent magnetic fields and induced magnetic fields. The remanent magnetic field has a major role in the magnetization of rocks, namely the magnitude and direction of magnetic fields associated with previous magnetic events. The anomalies obtained from this survey are the result of a combination of remanent and induced magnetic fields. The anomaly increases when the direction of the remanent magnetic field is the same as the direction of the induced magnetic field [11].

TABLE III. INTERNATIONAL GEOMAGNETIC REFERENCE FIELDS (IGRF) 2020 FOR SEMBALUN LAWANG

Magnetic Field							
Modul Used	IGRF2020						
Latitude	008.3623758° S						
Longitude	116.5429192° E						
Elevation	1149.0 m GPS						
<i>Date</i>	<i>Declination (+E / -W)</i>	<i>Inclination (+D / -U)</i>	<i>Horizontal Intensity</i>	<i>North Comp (+N / -S)</i>	<i>East Comp (+E / -W)</i>	<i>Vertical Comp (+D / -U)</i>	<i>Total Field</i>
7/2/2019	1.0200°	32.6649°	37,706.6 nT	37,700.6 nT	671.2 nT	24,174.5 nT	44,790.5 Nt
Change/Year	0.0604°/yr	0.0945°/yr	33.0 nT/yr	33.7 nT/yr	39.2 nT/yr	66.6 nT/yr	8.2 nT/yr



Fig. 1. Location of this study, which uses data from previous researches in 2019 [8], [9]. The data collections were carried out in Sembalun Lawang with an area of 1200 m² and Sembalun Timba Gading with an area of 2000 m², Sembalun District, East Lombok Regency.

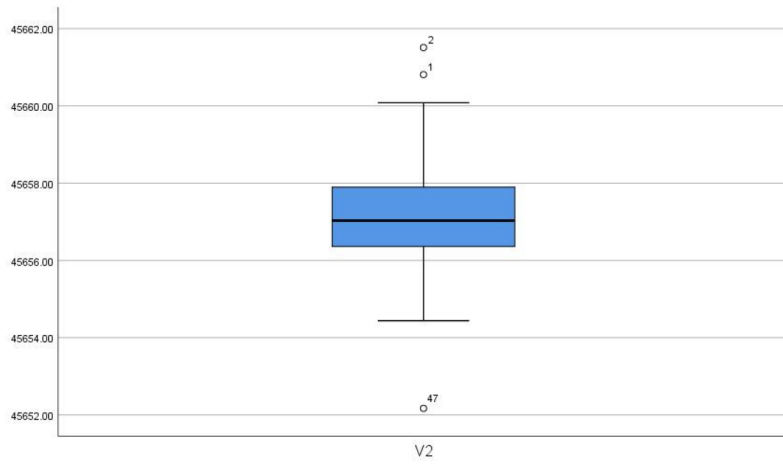


Fig. 2. The data indicated as outliers (subject numbers 1, 2, and 47).

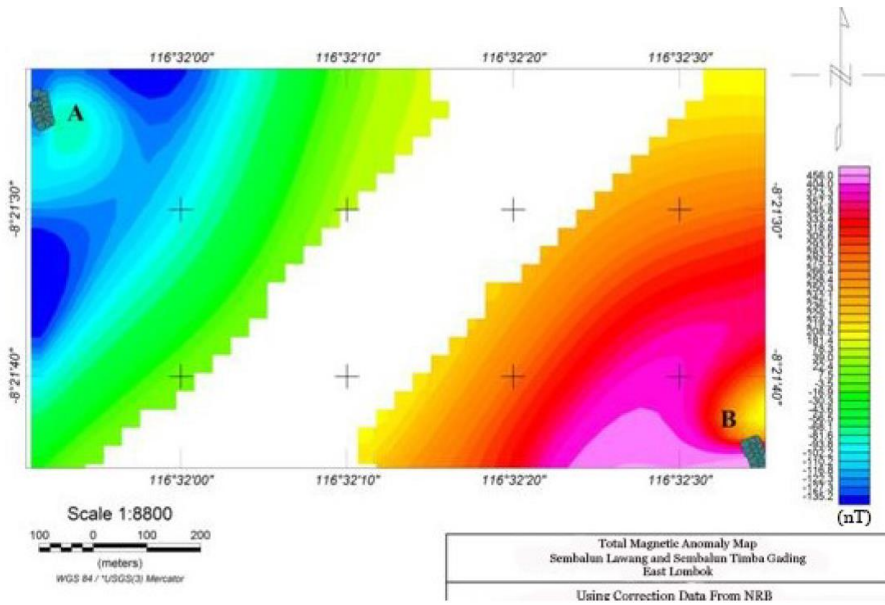


Fig. 3. Total Magnetic Anomaly Map for Sembalun Timba Gading (A) and Sembalun Lawang (B) using correction data from NRB Station.

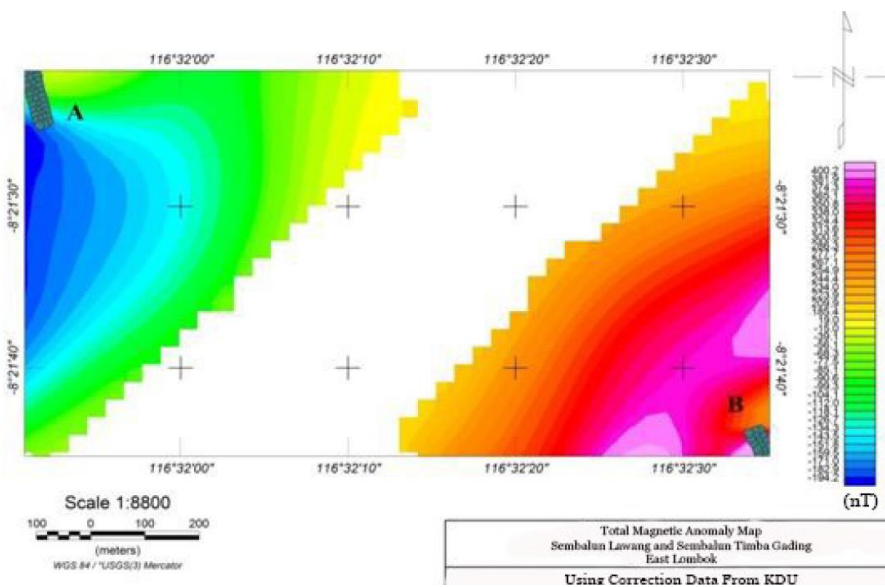


Fig. 4. Total Magnetic Anomaly Map for Sembalun Timba Gading (A) and Sembalun Lawang (B) using correction data from KDU Observatory

IV. RESULTS AND DISCUSSIONS

From the results of data processing, by using Oasis Montaj Software, a map of the total magnetic anomaly is derived from regional and residual anomalies.

Fig. 3 shows the pattern of magnetic field anomalies in Sembalun Timba Gading (A) and Sembalun Lawang (B) areas, which were processed using data correction from NRB Station. The resulting total magnetic anomaly has a range of values between -135.2 nT to 456.0 nT. The negative anomaly is in the (A) research area, the high negative closure has a value range of -135.2 nT to -102.2 nT, located in the West to the North. The positive anomaly is in the (B) research area, the high positive closure has a value range of 456.0 nT to 181.4 nT, located in the South to the West.

Fig. 4 shows the distribution pattern of magnetic field anomalies processed using correction data from the KDU Observatory. The resulting total magnetic anomaly has a range of values between -194.2 nT to 400.2 nT. The negative anomaly is in the (A) research area, the high negative closure has a value range of -194.2 nT to -104.1 nT, located in the West. The positive anomaly is in the (B) research area, the high positive closure has a value range of 400.2 nT to 185.4 nT, located in the North and South-West.

A principal in magnetic data processing: the best station/observatory to be used for data correction is the closest one to the measurement point. According to this principal, because the measurement point is in Sembalun area, therefore the best one to be used for magnetic data correction is NRB Station. The use of data correction from KDU Observatory aims to compare the differences in anomalous patterns. In this case, after processing magnetic data, the distance of the anomalous body shift can be determined.

By comparing anomaly maps in Fig. 3 and Fig. 4, the positions of positive and negative anomaly pattern are the same, namely the positive anomaly is in (B) and the negative anomaly is in (A). The difference lies in the position of the maximum peaks of the anomalies. When using data correction from NRB Station, it is found that one maximum peak of positive anomaly is in the South to the West and the maximum peak position of negative anomaly is in the West to the North. Meanwhile, when using data correction from KDU Observatory, it is found that the two maximum peaks of positive anomalies are in the North and West, while the maximum peaks of negative anomalies are in the West.

The difference in the results obtained by using data from the two station/observatory greatly affects the position of the maximum peaks of positive and negative anomalies. The significant difference lies in the positive anomaly, which a difference in the maximum peak position is of ± 250 meters.

These results should be considered in geothermal exploration in Lombok Island. KDU Observatory data can be used as replacement correction data (when NRB Station data is unavailable) provided if only the geothermal survey is carried out on the island of Lombok in an area that has a homogeneous landscape within a radius of > 250 meters. If the local landscape is quite complex (such as in some parts of Sembalun area), then KDU Observatory data cannot be used as replacement correction data on the island of Lombok.

The second difference lies in the anomalous values obtained. By using correction data from NRB Station, the range of total anomaly values obtained is between -135.2 nT to 456.0 nT, while using data from KDU Observatory is between -194.2 nT to 400.2 nT. The total anomaly value obtained using correction data from NRB Station has a greater value than using KDU Observatory, because the distance from NRB Station is closer to the measurement point.

V. CONCLUSION

Result obtained from data processing is the difference in anomalous patterns in Sembalun Lawang and Sembalun Timba Gading areas using correction data from the NRB Station and the KDU Observatory. The difference lies in the position of the maximum positive anomaly with a distance of ± 250 meters. Considering geomagnetic surveys for geothermal explorations carried out on the island of Lombok, Kakadu (KDU) observatory data can be used as replacement correction data if Nurul Bayan (NRB) or other local station/observatory data is unavailable; with a special note: if only the survey carried out in an area that has a homogeneous landscape within a radius of > 250 meters.

ACKNOWLEDGMENT

This study received funding from the University of Mataram, under the research grant (Penelitian Penugasan Tahun 2022) entitled "EKSPLOKASI POTENSI GEOTHERMAL PROSPEK SEMBALUN UNTUK PEMANFAATAN LANGSUNG". The results presented in this paper rely on the data collected at Kakadu Observatory. We thank Geoscience Australia, for supporting its operation and INTERMAGNET for promoting high standards of magnetic observatory practice (www.intermagnet.org).

REFERENCES

- [1] A. Frayogo, S. Maryanto, A. Nadhir, "Determination of Heat Reservoir Distribution in Potential Geothermal Area Tiris-Lamongan, Probolinggo, East Java Based on Remote Sensing and Magnetic Data," Malang, Physics Department, Brawijaya University, 2019.
- [2] R. Rifaldy, A. Kristanto, N.A. Ristianti, I. Yuliandari, I. Koswara, C.A. Perwita, "Estimation of Hydrothermal Flow Direction with Gravity Method Using Satellite Imagery Data in the Kelud Mountain Area of Kediri Regency," Proceedings on the 10th National Earth Science Seminar, Yogyakarta.
- [3] F. Febriani, D.S. Widarto, E.Z. Gaffar, A. Nasution, H. Grandis, T. Anggono, Syuhada, "Magnetotelluric investigation for imaging the subsurface geoelectrical feature of the prospective Sembalun-Propok geothermal zone, Indonesia," Arabian Journal of Geosciences, 2019.
- [4] H. Sundhoro, Kasbani, A. Yushantarti, and M. N. Hadi. "Integrated Geothermal Survey (Geology, Geochemistry, and Geophysics) Sembalun Area, East Lombok Regency," Ntb. Journal.
- [5] International Geothermal Association (IGA) Service GmbH, "Best Practices Guide For Geothermal Exploration, Bochum University of Applied Sciences (Hochschule Bochum) Lennerhofstr, 140, D-44801 Bochum, Germany, 2014.
- [6] Nurdianto, B. Wahyudi, I. Suwanto, "Ungaran Volcano Slope Subsurface Hot Spring Manifestations," 29th AH 2004, PIT Proceedings, Yogyakarta.
- [7] T. Zubaidah, M. Korte, M. Mandea, M. Hamoudi, "New Insights Into Regional Tectonics of The Sunda-Banda Arcs Region from Integrated Magnetic and Gravity Modelling," Journal of Asian Earth Sciences, Vol. 80, pp. 172-184, 2014.
- [8] H. Hadi. "Survey of Geothermal Energy Potential Mapping Using the Geomagnetic Method in the Sembalun Area, Timba Gading Village, East Lombok," Thesis. Mataram, Electrical Engineering, Mataram University, 2019.

- [9] H. N. Ukassyah. "Subsurface Interpretation Based on Geomagnetic Data in the Geothermal Prospect Area of Sembalun Lawang Village," Thesis. Mataram, Electrical Engineering, Mataram University, 2019.
- [10] T. Zubaidah, M. Korte, M. Manda, Y. Quesnel, B. Kanata. "Geomagnetic field anomalies over the Lombok Island region: an attempt to understand the local tectonic changes." *Int J Earth Sci (Geol Rundsch)*, Vol. 99, pp. 1123–1132, 2010. DOI 10.1007/s00531-009-0450-4.
- [11] W. Telford, L. Geldart, R. Sheriff, and D. Keys. *Applied Geophysics*, Cambridge University Press, New York.

Time-frequency Analysis of Normal and Abnormal Lung Breath Sounds with Short-time Fourier

Bulkis Kanata

*Department of Electrical Engineering
University of Mataram
Mataram, Indonesia
uqikanata@unram.ac.id*

Sabhan Kanata

*Department of Electrical Engineering
Sumatera Institute of Technology
South-Lampung, Indonesia
sabhan.kanata@el.itera.ac.id*

Abstract—This paper uses a short-time Fourier transform process to minimize errors in determining the type of breath sound through hearing. This process aims to visually determine the distribution of the respiratory sound frequency and the frequency distribution of the inspiration-expiration process. This study uses data on normal and abnormal breath sounds from Medzcool and hospitals in Lombok. The results of the spectrogram of normal breath sounds show that the frequency is distributed at 30 Hz – 1000 Hz, while the abnormal frequency is 100 Hz – 700 Hz. The process of inspiration-expiration in normal breathing is 12-20 times per minute. Abnormal breathing has a process that is less than 12 times per minute and more than 20 times per minute.

Keywords—spectrogram, breath sound, frequency, short-time Fourier transform

I. INTRODUCTION

Breathing is inhaling oxygen in the air, known as the inspiration process, and removing carbon dioxide from the body, known as the expiration process [1]. The need for sufficient oxygen is essential so that humans can still maintain metabolism in the body. Lack of oxygen in the body can cause health problems and even death. One way to know normal or abnormal human breathing is the sound of the breath itself. These sounds occur during the process of inspiration and expiration. The sounds that occur due to these two processes can be heard by auscultation using a stethoscope. These processes can produce sounds that vary because it depends on which part of the respiratory system is affected. From Laënnec's era [2] until nowadays, auscultation has been adopted by physicians as an easy, fast and non-invasive way to evaluate and diagnose patients with lung diseases.

Nevertheless, auscultation exhibits noticeable drawbacks, as it suffers from subjectivity and variability in interpreting its diagnostic information. This diagnostic value can be better revealed when sound signal digitization and processing techniques are employed [3], [4]. In that way, novel diagnostic tools that objectively track the characteristics of the relevant pathology and assist the clinician in everyday practice could be introduced [5]. Assessment of the different types of sounds produced when breathing is very important for medical personnel. The goal is that medical personnel can assess whether the breathing sound is in the normal or abnormal category to take appropriate action.

Normal breath sounds are classified as tracheal, bronchial, vesicular, or bronchovesicular. Tracheal and bronchial sounds, produced by turbulent airflow, are loud and can be heard throughout inspiration and expiration over the trachea and mainstem bronchi. Vesicular breath sounds are faint; they are best heard over other chest wall areas

throughout inspiration and at the beginning of expiration. Bronchovesicular breath sounds are heard over areas between the mainstem bronchi and the smaller airways; their pitch and duration are midway between those of tracheal and mainstem bronchi breath sounds and normal breath sounds heard over other chest wall areas [6].

There are two types of abnormal breath sounds, namely intermittent sounds and continuous sounds. Intermittent sounds include rhonchi (basic and dry) and pleural friction rub. Continuous sounds include wheezing and stridor. Ronchi is a sound produced through the airways because it contains a secret/exudate. In other words, the respiratory tract is constricted. In comparison, the pleural friction rub is a sound that occurs during the inspiration process due to a shift between the parietal pleura and the visceral pleura. Wheezing in respiratory sounds is the most specific asthmatic symptom [7]. Asthma is a disease of the respiratory tract. The disease can cause increased hyperresponsiveness of the respiratory tract. Increased hyperresponsiveness can produce a wheezing sound. Sound is one of the characteristics of asthmatics [8]. In comparison, stridor is a rough (hoarse) sound with a high or low pitch. The sound arises from each inhalation or exhalation. The cause is due to the narrowing (obstruction) of some of the upper respiratory tract [8].

Research related to diagnosing respiratory diseases such as lung and asthma has been done before. Research related to the disease has proven its success in diagnosing the disease based on the analysis of respiratory sounds. Sound analysis of the disease uses classification techniques such as a semi-supervised deep learning algorithm [9]; Convolutional neural networks [10]; biomimetic multi-resolution [11]; Time-frequency (TF) technique as well as wavelet packet decomposition (WPD) [12]; Support Vector Machine [13], [14]; multilayer perceptron (MLP) neural network and mel-frequency cepstral coefficients (MFCC) [15]; artificial neural networks (ANNs) and adaptive neuro-fuzzy inference systems (ANFIS) [16]; and K-Nearest Neighbor Classification [17].

In this paper, the researchers conducted a short-time Fourier transform process. It aims to visually determine the distribution of respiratory sound frequencies, sound patterns, and the period of inspiration expiration. Describing the frequency distribution of the sound can be a recommendation for medical personnel to determine the patient's normal or abnormal breathing sounds being examined.

In the post-covid pandemic era, viruses that cause respiratory problems are often a frightening symptom. Therefore, medical personnel require rapid treatment to detect the patient's respiratory condition. The method of a short-time Fourier transform process can assist medical personnel in making decisions by visual observation.

II. METHOD

Short-time Fourier transform (STFT) is suitable for a band-limited signals like speech and sound. Mathematically, the STFT is modelled on (1) [18], [19].

$$STFT(\tau, f) = \int x(t)g(t-\tau)e^{-2\pi ft} dt \quad (1)$$

The working step of the short time-frequency Fourier transform is to divide the signal into small segments using a sliding window function $g(t)$ centred on τ . The Fourier transform is performed in a time localized manner on the signal $x(t)$ for each segment sequentially. The aim is to obtain information from the content of frequency variations over time [20].

Bicubic interpolation uses 4 x 4 of the neighbouring pixels to get information. The formula is modelled on (2) [21].

$$p(x,y) = \sum_{i=0}^{N-1} \sum_{j=0}^{N-1} a_{ij}x^i y^j \quad (2)$$

with

a = the location of the nearest neighbour pixel
 x = the location of the new pixel horizontally
 y = the location of the new pixel vertically

The breath sound data used in this paper was sourced from Medzcool. Medzcool is an interactive medical sound library to help you learn the physical exam skills of auscultation and patient medical records at a hospital in Lombok. Data varies from 10 to 16 seconds with a sampling frequency of 44,100 Hz. Normal breath sounds consist of trachea, bronchial, bronchovesicular, and vesicular. In contrast, abnormal respiratory sounds consist of rhonchi, pleural friction rub, wheezing, and stridor.

Respiratory data is processed using a short-time Fourier transform. The steps are as follows:

1. The windowing process is carried out on the breath sound signal with the same width,
2. The Fourier transform process is carried out on each segment from the windowing process to obtain the frequency content of each segment,
3. The process of calculating the power spectral density (PSD) is carried out,
4. The process of drawing the spectrogram is carried out where the x component shows the time, the y component shows the frequency, and the z component shows the power spectral densities,
5. The process of applying bicubic interpolation is carried out

III. RESULT AND DISCUSSION

A. Normal Breathing Sounds

The normal respiratory sound signals used and generated by the spectrogram are shown in Fig. 1 – Fig. 4. Based on the results of the spectrogram, it can be seen visually the distribution of respiratory tone frequency, power spectral density and the period of inspiration-expiration (breathing period), and the frequency of the inspiration-expiration process in time per minute as shown in Table I.

TABLE I. NORMAL BREATHING SOUNDS

Type of Breathing Sounds	Pitch frequency distribution	Power spectral density	Breathing period	Inspiration-expiration process
	(Hz)	(dB/Hz)	(s)	Time/minute
Tracheal breath sounds	30-600	-40	4	15
Bronchial breath sounds	100-800	-40	3	20
Bronchovesicular breath sounds	200-1000	-40	3	20
Vesicular breath sounds	100-700	-40	3.5	17

The four normal breathing patterns in the spectrogram can be explained as follows:

a. Tracheal breath sounds

The spectrogram is shown in Fig. 1(b). Pitch is spread at a frequency of 30-600 Hz. Fig. 1(b) indicates a red power spectral density of about -40 dB/Hz. Pitch looks longer and louder in the expiration than in the inspiration with a breathing period of about 4 seconds, so 1 minute occurs 15 times for the inspiration-expiration process.

b. Bronchial breath sounds

The spectrogram is shown in Fig. 2(b). Pitch is spread at a frequency of 100-800 Hz. This is indicated by a red spectral density of about -40dB/Hz. The pitch produced during the process of inspiration and expiration looks loud. However, the pitch appears shorter during expiration. The time of inspiration and expiration is almost the same as the period of breathing which is about 3 seconds, so one minute occurs 20 times for the inspiration-expiration process.

c. Bronchovesicular breath sounds

The spectrogram is shown in Fig. 3(b). The pitch is spread in the 200-1000 Hz frequency, which is indicated by the red spectral density of about -40dB/Hz. The time used for the process of inspiration and expiration is almost the same as the breathing period, which is about 3 seconds. As a result, one minute occurs 20 times the inspiration-expiration process.

d. Vesicular breath sounds

The spectrogram is shown in Fig. 4(b). The pitch is spread at a 100 - 700 Hz frequency, marked by a red spectral density of about -40 dB/Hz. The pitch produced on inspiration is more extended than expiration, which is a ratio of 3:1. The period of breath occurs in about 3.5 seconds, so in one minute, there is 17 times the inspiration-expiration process.

Based on spectrograms of the tracheal, bronchial, bronchovesicular, and vesicular breath sounds in Fig. 1- Fig. 4 obtained that normal breath sounds are distributed at a frequency of 30 Hz – 1000 Hz. The results of the analysis of normal breath sound from Fig. 1 - Fig. 4 are obtained from 15 times per minute to 20 times per minute, and this result follows the frequency of normal breath sounds for adults, which is in the range of 12 - 20 times per minute [6]-[23].

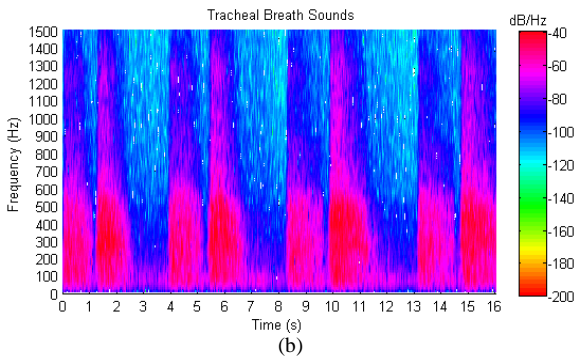
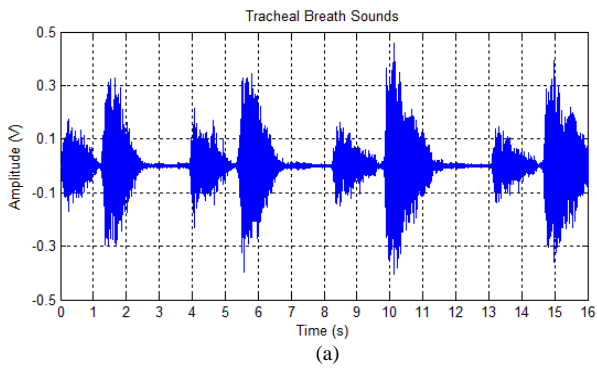


Fig. 1. Example of a figure caption Tracheal breath sounds – Normal lung sounds: (a) sounds signal and (b) spectrogram.

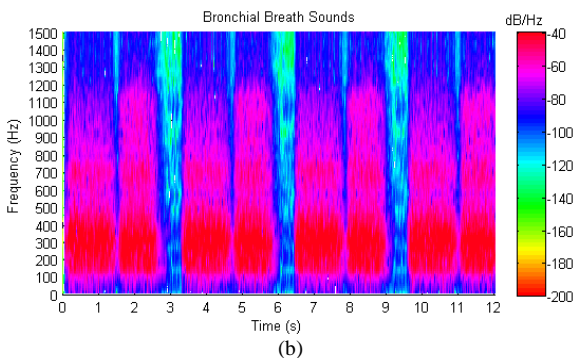
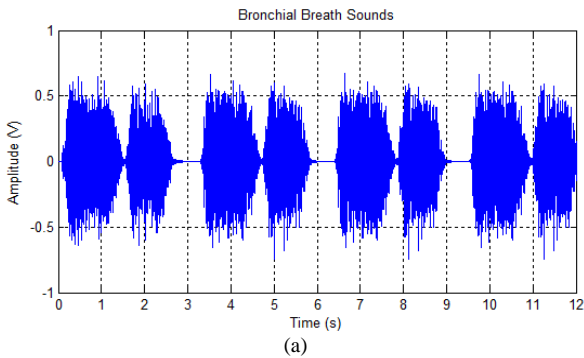


Fig. 2. Bronchial breath sounds – Normal lung sounds: (a) sounds signal and (b) spectrogram.

B. Abnormal Breathing Sounds

The abnormal respiratory sound signals used and generated by the spectrogram are shown in Fig. 5 – Fig. 8. Based on the results of the spectrogram, it can be seen visually the distribution of respiratory tone frequency, power spectral density and the period of inspiration-expiration (breathing period), and the frequency of the inspiration-expiration process in time per minute as shown in Table II.

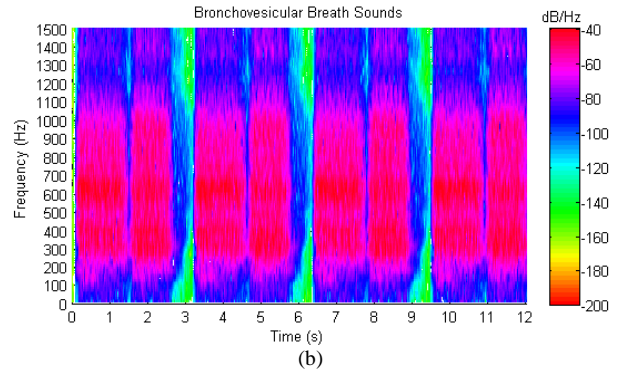
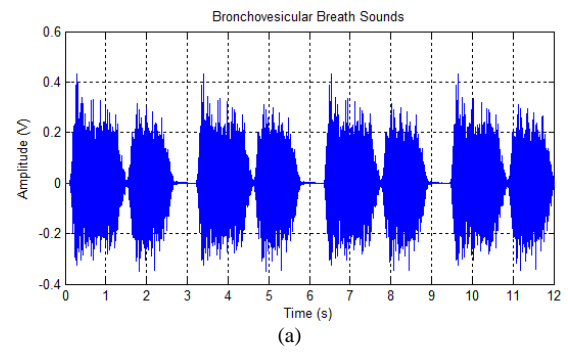


Fig. 3. Bronchovesicular breath sounds – Normal lung sounds: (a) sounds signal and (b) spectrogram.

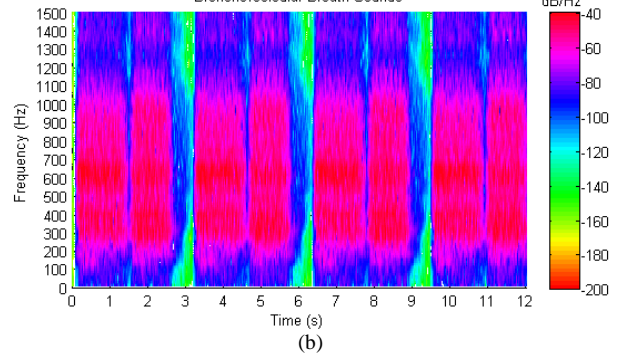
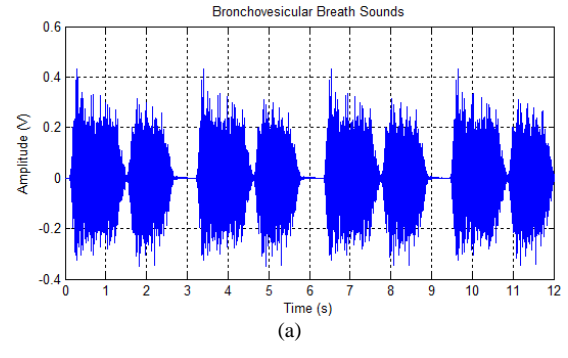


Fig. 4. Vesicular breath sounds – Normal lung sounds: (a) sound signal and (b) spectrogram

The four abnormal breathing patterns in the spectrogram can be explained as follows:

a. Wheezing

The spectrogram in Fig. 5(b) shows that the pitch is distributed at a frequency of 200-400Hz. The red spectral density indicates this with a -40dB/Hz value. The duration of the pitch used on inspiration is

approximately 0.5 seconds. In contrast, the duration used for expiration is 1.5 seconds. This means that these two processes have a duration ratio of 1:3. Based on the pitch of the sound of normal breathing, the average time used in the inspiration process is longer or equal to the time used in the expiration process. While the pitch of the wheezing sound, the time used for the expiration process is longer. In addition, during the process, it has a louder sound and is marked in red. The breathing period occurs in about 2.5 seconds. As a result, one minute occurs about 24 times the process of inspiration-expiration.

b. Stridor

The spectrogram in Fig. 6(b) shows that the pitch is spread at 100-700 Hz. This is indicated by the red spectral density of about -40dB/Hz. The duration of the inspiratory and expiratory pitches is about 1 second with a ratio of 1:1. The breathing period lasts about 1.5 seconds. As a result, one minute occurs about 40 times the process of inspiration-expiration.

c. Rhonchi

The spectrogram in Fig. 7(b) shows that the pitch is spread at a 200-700 Hz frequency. This is indicated by the red spectral density of about -40dB/Hz. The time spent on inspiratory and expiratory pitches is about 4.5 seconds. No pause occurs in the following inspiration-expiration process. The duration used in the inspiration process is shorter than the expiration process, with a time ratio of 1:3. The breathing period occurs in 4.5 seconds. As a result, one minute occurs 11 times the process of inspiration-expiration.

d. Pleural friction rub

The spectrogram in Fig. 8(b) shows that the pitch is spread at 100-400 Hz. This is indicated by the red spectral density, around -40dB/Hz. The time used for inspiratory and expiratory pitches is about 2 seconds. The duration that occurs during the inspiration process is longer than during the expiration process, with a time ratio of 2:1. The breathing period lasts about 2.8 seconds. Hence, one minute occurs about 21 times the inspiration-expiration process.

Based on the spectrogram of wheezing, stridor, rhonchi, and pleural friction rub in Fig. 5 - Fig. 8, abnormal breath sounds are distributed at 100 Hz - 700 Hz. The analysis of abnormal breathing sound results from Fig. 5- Fig. 8 obtained a respiratory frequency of fewer than 12 times per minute and greater than 20 times per minute. This corresponds to the abnormal respiratory frequency of adults outside the range of 12-20 breaths per minute [6]-[23].

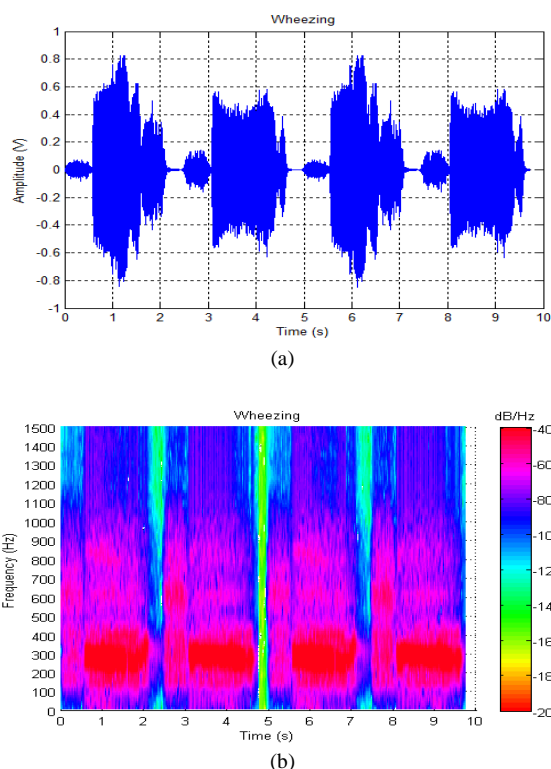


Fig. 5. Wheezing breath sounds – lung sounds: (a) sounds signal and (b) spectrogram

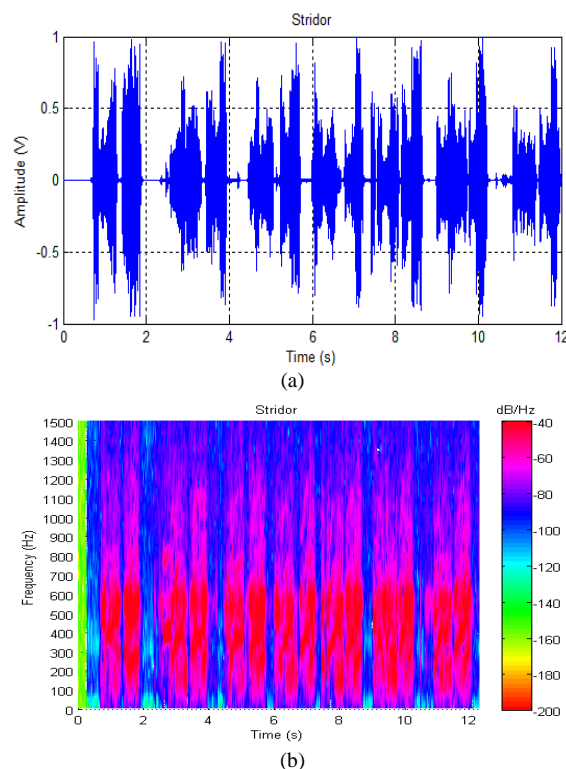
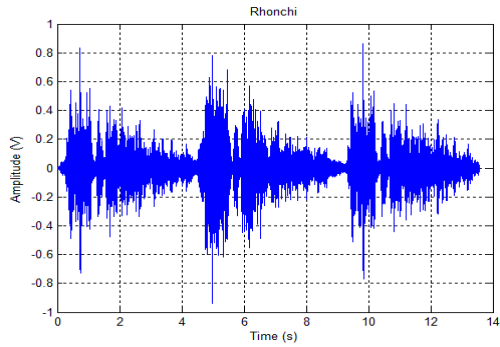


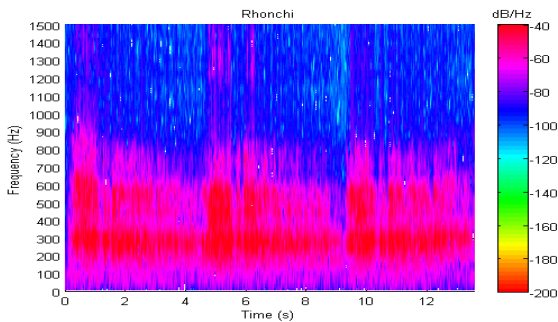
Fig. 6. Stridor breath sounds – lung sounds: (a) sounds signal and (b) spectrogram.

TABLE II. ABNORMAL BREATHING SOUNDS

Type of Breathing Sounds	Pitch frequency distribution	Power spectral density	Breathing period	Inspiration -expiration process
	(Hz)	(dB/Hz)	(s)	Time/minute
Wheezing	200-400	-40	2.5	24
Stridor	100-700	-40	1.5	40
Rhonchi	200-700	-40	4.5	11
Pleural friction rub	100-400	-40	2.8	21

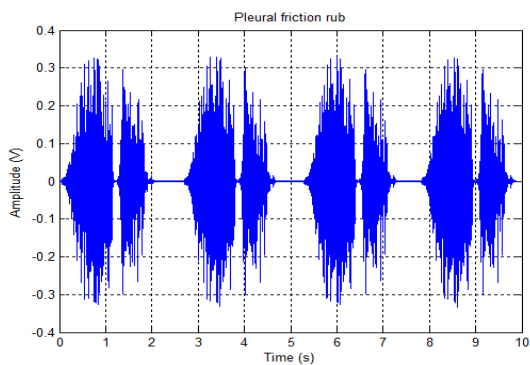


(a)

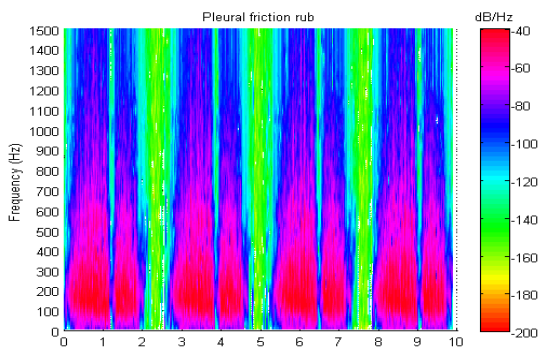


(b)

Fig. 7. Rhonchi breath sounds – lung sounds: (a) sounds signal and (b) spectrogram



(a)



(b)

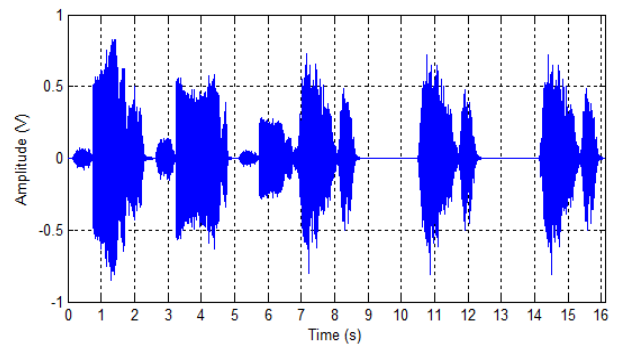
Fig. 8. Pleural friction rub – lung sounds: (a) sounds signal and (b) spectrogram

C. Breathing Sounds Test

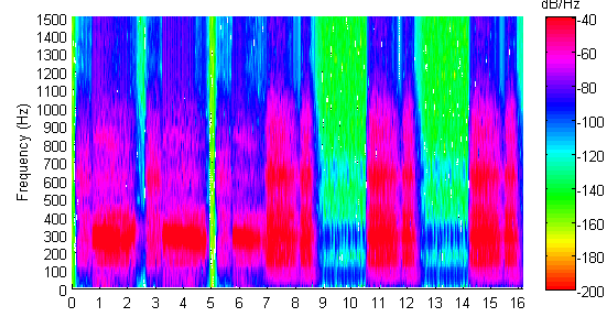
The breath sounds used for testing are breath sounds that have been determined by Medzcool and a doctor at the hospital. The data contains wheezing and vesicular breath sounds for data from Medzcool, while data from the hospital contains wheezing and rhonchi pitch.

Fig. 9 – Fig. 11 are test signals. These signals are compared with those in normal and abnormal sounds, as shown in Fig. 1 – Fig. 8. In Fig. 9, 3 pitch patterns resemble wheezing at the 1st to 7th second. In the figure, three normal breathing pitch patterns resemble vesicular breath sounds indicated in the 7th to the last second.

Fig. 10 shows a pattern of normal breathing pitch that resembles a vesicular breath sound for two seconds. In addition, in the figure, five patterns resemble wheezing pitch from the 2nd second to the last. As for Fig. 11, there is a wheezing pattern. The pattern occurs from 1st to 2nd, the 3.5th to 4.5th second, and the 9th to last. In addition to the pattern that occurred at that time, other patterns resemble Ronchi. The visual analysis results with a short-time Fourier transform show that the resulting pitch pattern corresponds to the type of data from Medzcool and the data that the hospital has determined.



(a)



(b)

Fig. 9. 1st Test breath sounds: (a) sounds signal and (b) spectrogram.

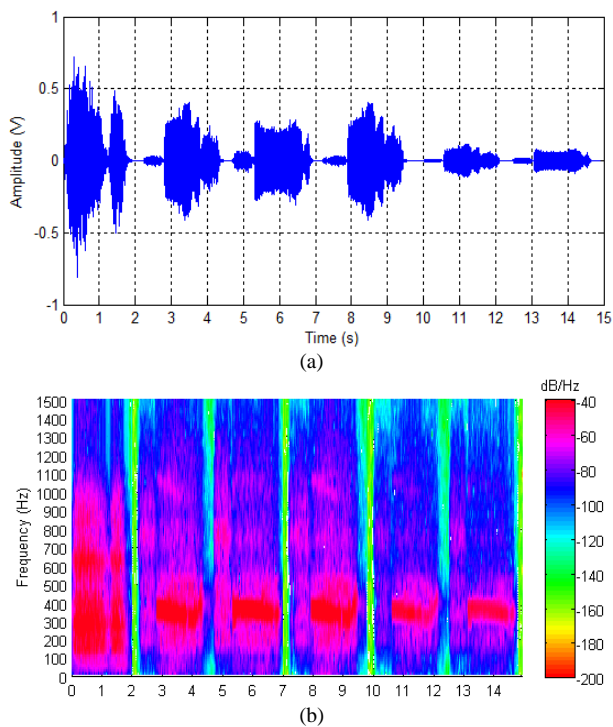


Fig. 10. 2nd Test breath sounds: (a) sounds signal and (b) spectrogram.

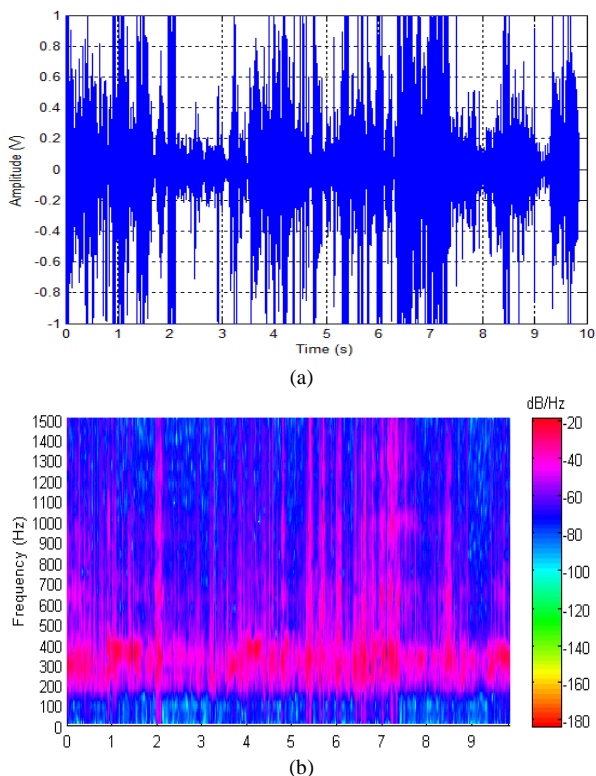


Fig. 11. 3rd Test breath sounds: (a) sounds signal and (b) spectrogram.

IV. CONCLUSIONS

The spectrogram in this paper shows that normal breath sounds are distributed at a frequency of 30 Hz – 1000 Hz. In contrast, abnormal breath sounds are distributed at 100 Hz - 700 Hz. The process of inspiration - expiration in normal breathing is in the range of 12-20 times per minute, i.e., 15 -

20 times per minute, whereas abnormal breathing is less than 12 times per minute and greater than 20 times per minute. Differences in the type of normal or abnormal sound can be seen from the frequency distribution pattern in the pitch of sound and length of the sound in the inspiration-expiration process.

ACKNOWLEDGMENT

The authors would like to thank the University of Mataram for funding the publication of AEMT fees.

REFERENCES

- [1] C. A. Del Negro, G. D. Funk, and J. L. Feldman, "Breathing matters," *Nat. Rev. Neurosci.*, vol. 19, no. 6, pp. 351-367., 2018.
- [2] R. T. H. Laennec, "De l'auscultation médiante: ou traité du diagnostic des maladies des poumons et du coeur," in 2, 1819.
- [3] N. Avriely and W. C. David, *Breath sounds methodology*. CRC Press, 2019.
- [4] L. J. Hadjileontiadis, Y. A. Toliás, and S. . Panas, "Intelligent system modeling of bioacoustic signals using advanced signal processing techniques," *Intell. Syst. Technol. Appl.*, vol. 3, pp. 103-156., 2002.
- [5] S. A. Taplidou and J. H. Leontios, "Wheeze detection based on time-frequency analysis of breath sounds," *Comput. Biol. Med.*, vol. 37, no. 8, pp. 1073–1083, 2007.
- [6] J. S. Coviello, *Auscultation skills: Breath & heart sounds: Fifth edition*. 2013.
- [7] D. Oletic and B. Vedran, "Asthmatic wheeze detection from compressively sensed respiratory sound spectra," *IEEE J. Biomed. Heal. Informatics*, vol. 22, no. 6, pp. 1406–1414, 2017.
- [8] A. Satriadi, I. M. Budi Suksmadana, and B. Kanata, "Analisis Suara Pernapasan Paru-Paru Asma Dengan Tidak Asma Menggunakan Metode K Nearest Neighbors," *Dielektrika*, vol. 8, no. 1, p. 1, 2021, doi: 10.29303/dielektrika.v8i1.251.
- [9] D. Chamberlain, K. Rahul, G. Daniela, M. Vivek, and R. F. Richard, "Application of semi-supervised deep learning to lung sound analysis," in *2016 38th Annual international conference of the IEEE engineering in medicine and biology society (EMBC)*, 2016, pp. 804–807.
- [10] F. Demir, S. Abdulkadir, and B. Varun, "Convolutional neural networks based efficient approach for classification of lung diseases," *ealth Inf. Sci. Syst.*, vol. 8, no. 1, 2020.
- [11] D. Emmanouilidou, P. Kailash, W. James, and E. Mounya, "A multiresolution analysis for detection of abnormal lung sounds," in *2012 Annual International Conference of the IEEE Engineering in Medicine and Biology Society*, 2012, pp. 3139–3142.
- [12] S. Emrani and K. Hamid, "Wheeze detection and location using spectro-temporal analysis of lung sounds," in *2013 29th Southern Biomedical Engineering Conference*, 2013, pp. 37–38.
- [13] S. Abbasi, D. Roya, A. Ataollah, and Y. Sarbaz, "Classification of normal and abnormal lung sounds using neural network and support vector machines," in *2013 21st Iranian Conference on Electrical Engineering (ICEE)*, 2013, pp. 1–4.
- [14] F. Jin, S. Farook, and Y. G. Daniel, "New approaches for spectro-temporal feature extraction with applications to respiratory sound classification," *Neurocomputing*, vol. 123, pp. 362–371, 2014.
- [15] A. Hashemi, A. Hossein, and A. Khosrow, "Classification of wheeze sounds using cepstral analysis and neural networks," *Med. Meets Virtual Real.*, vol. 19, pp. 161–165, 2012.
- [16] R. J. Oweis, E. W. Abdulhay, A. Khayal, and A. Awad, "An alternative respiratory sounds classification system utilizing artificial neural networks," *Biomed. J.*, vol. 38, no. 2, pp. 153–161, 2015, doi: 10.4103/2319-4170.137773.
- [17] C. H. Chen, W. T. Huang, T. H. Tan, C. C. Chang, and Y. J. Chang, "Using K-nearest neighbor classification to diagnose abnormal lung sounds," *Sensors (Switzerland)*, vol. 15, no. 6, pp. 13132–13158, 2015, doi: 10.3390/s150613132.
- [18] S. W. Kim and S. Y. Kim, "Analysis of dispersion of pulse signals in underground tunnels using finite-difference time domain and short-time fourier transform," *Proc. 13th International Conf. Gr. Penetrating Radar, GPR 2010*, no. 1, 2010, doi:

10.1109/ICGPR.2010.5550216.

- [19] Y. Li, W. Peng, X. Zhu, G. Wei, H. Yu, and G. Qian, "Based on short-time fourier transform impulse frequency response analysis in the application of the transformer winding deformation," *2016 IEEE Int. Conf. Mechatronics Autom. IEEE ICMA 2016*, pp. 371–375, 2016, doi: 10.1109/ICMA.2016.7558591.
- [20] R. X. Gao and R. Yan, "Non-stationary signal processing for bearing health monitoring," *Int. J. Manuf. Res.*, vol. 1, no. 1, pp. 18–40, 2006, doi: 10.1504/IJMR.2006.010701.
- [21] D. Abdullah, F. Fajriana, M. Maryana, L. Rosnita, A. P. U. Siahaan, R. Rahim, P. Harliana, H. Harmayani, Z. Ginting, C. I. Erliana, D. Irwansyah, Z. Zulmiardi, M. Khaddafi, F. Milanie, H. Aspan, I. Huda, K. Saddhono, I. Mulyaningsih, R. M. Moonti, Parwito, H. Djanggih, A. Amalia, E. Winarno, and W. Hadikurniawati., "Application of Interpolation Image by using Bi-Cubic Algorithm," in *Journal of Physics: Conference Series*, 2018, vol. 1114, no. 1. doi: 10.1088/1742-6596/1114/1/012066.
- [22] M. Wulandari, "Index quality assesment citra terinterpolasi (SSIM dan FSIM)," *J. Terap. Teknol. Inf.*, vol. 1, no. 1, pp. 11–20, 2017, doi: 10.21460/jutei.2017.11.5.
- [23] M. C. Huang, W. Xu, J. Liu, L. Samy, A. Vajid, N. Alshurafa, and M. Sarrafzadeh, "Inconspicuous on-bed respiratory rate monitoring," 2013. doi: 10.1145/2504335.2504353.

Optimization of Patch E-Shape Array Microstrip Antenna 2.45 GHz Using Double Reflector

Cahyo Mustiko Okta Muvianto
Department of Electrical Engineering
University of Mataram
Mataram, Indonesia
cahyo.muvianto@unram.ac.id

Buyung Satrya Anugrah
Department of Electrical Engineering
University of Mataram
Mataram, Indonesia
buyungsatrya14@gmail.com

Suthami Ariessaputra
Department of Electrical Engineering
University of Mataram
Mataram, Indonesia
suthami@unram.ac.id

Sareh Malekpour
The University of Manchester
Manchester, United Kingdom
sareh.malekpour@manchester.ac.uk

Abstract— Microstrip antennas are widely used in telecommunications equipment because they are compact, practical, and easy to adjust. Modifying the patch and the reflector models can improve the microstrip antenna performance. An e-shaped microstrip antenna is one model antenna used for WiFi. In this research, the E-Shaped patch microstrip antenna was optimized by adding and modifying two reflector layers. The first reflector uses a complementary form with the same dimension as the patch. Secondly, the other layer uses Defected Ground Structure (DGS) symmetric "+" shape. This modification can increase the gain and bandwidth of the microstrip antenna. Based on the measurement results, this antenna can work at a center frequency of 2435 MHz with a gain value of 7.139 dB, a VSWR of 1.7, a bandwidth of 60 MHz, and has linear polarization.

Keywords— Microstrip, reflector, E-Shaped patch, DGS, conjugate.

I. INTRODUCTION

WiFi (Wireless Fidelity) is a wireless technology for communication that operates at 2.4 GHz and 5 GHz [1]. This technology contains 11–13 channels, every 1 MHz wide range for a track. It has Data rates for WiFi ranging from 11 Mbps to 100 Mbps. The volume of data conveyed and the speed of delivery have increased along with human demands, which has sparked a lot of interest in creating supporting devices with wide bandwidth and high gain [2].

The advancement of telecommunications technology has produced numerous breakthroughs in wireless communication systems to improve gain and bandwidth antenna. Modification and development of antenna design is one way to increase antenna bandwidth. Antennas are one of the crucial parts of wireless communication systems. This component acts as a means to transmit and receive electromagnetic waves contained in the free air. Antennas have many types and shapes with various characteristics of each type of antenna. One type of antenna that is popular today is a microstrip antenna with petite and thin dimensions [3]. The array model is one way to get a high-gain microstrip antenna for WiFi applications [4], [5].

Microstrip antennas have low gain and narrow bandwidth, limiting their use. Several studies use proximity-coupled methods to improve the quality of microstrip antennas [6], [7]. But the improvement of gain is not significant. Optimizing the rectangular microstrip antennas on dual-band antennas for WiFi frequency has been done [8],

[9]. It can add antenna bandwidth. Antenna patch microstrip for wireless communication has several models, such as square, rectangular, and triangle [10]. The square antenna can be modified to an E-shape form to increase efficiency. E-Shaped antennas have higher gain and directivity than square antennas [11], [12]. E-Shaped antennas have more resonance than square antennas [13].

In addition, adding or modifying the antenna feeder and reflector portion can improve the gain and bandwidth antenna [14]. The reflector can be its conjugate circuit, which has the opposite shape to the original antenna [15]. In addition, the multi-layer antenna consists of DGS (Defected Ground Structures) [16]. Furthermore, the reflector can combine the conjugate and its DGS [17].

Based on these reasons, the idea is to make an E-Shaped Microstrip patch antenna that can work at a frequency of 2.45 GHz, which can implement for WiFi systems with relatively high gain and wide bandwidth. A reflector is needed or with the addition of DGS to obtain high power and wide bandwidth. The antenna structure of the E-Shape antenna consists of two layers. The first reflector uses a complementary design, and the second uses a DGS in the form of plus (+). Antenna feed systems using a power-sharing network on the antenna do not require complicated impedance adjustment techniques to match the impedance of each antenna element to a transmission line from the antenna. So it can be implemented as an antenna WiFi with high gain, wide bandwidth, and a physical form that is easy to apply.

II. ANTENNA DESIGN

A. Antenna Specification Optimization Antenna

WiFi antennas use copper (annealed) material as a conductor. Before realizing the antenna, it has simulated using software to know the performance.

TABLE I. ANTENNA SPESIFICATION

Parameter	Description
Frequency	2.45 GHz
Bandwidth	40 MHz
Return Loss (2.45 GHz)	-40.659 dB
VSWR	1.48
Gain	10.83 dB
Radiation Pattern	Directional
Polarization	Co-polarization
Antenna Dimension	172 mm x 82 mm

The simulation parameters observed include Return Loss (S_{11}), bandwidth, Voltage Standing Wave Ratio (VSWR), radiation pattern, polarization, bandwidth, and the gain of the antenna design, as shown in Table I.

B. Optimization Antenna

Table II compares antenna optimization with several different forms. There are three models of optimization such as only patch, patch with the conjugate, and patch with double reflector.

TABLE II. TYPE OF DIFFERENT ANTENNA MODEL

Antenna	Frequency Centre (GHz)	Gain (dB)	VSWR	Bandwidth (MHz)	S_{11} (dB)
Type	Different combinations of patch				
patch E-Shape	2,484	6,29	1,13	33	-23,7
patch E-Shape array 1x2	2,472	8,28	1,06	81	-30,268
patch E-Shape array 1x4	2,48	10,8	1,09	85	-26,707
Type	Patch with Conjugate				
patch E-Shape conjugate	2,484	6,3	1,14	33	-23,645
patch E-Shape array 1x2 conjugate	2,47	8,28	1,06	82	-30,38
patch E-Shape array 1x4 conjugate	2,48	10,8	1,04	84	-27,89
Type	Patch with Conjugate and DGS				
Patch E-Shape conjugate with DGS	2,49	6,27	1,14	60	-23,324
Patch E-Shape array 1x2 conjugate with DGS	2,46	8,2	1,05	81	-30,06
patch E-Shape array 1x4 conjugate with DGS	2,45	10,8	1,018	91	-40,659

The maximum optimization is patch E-Shape array 1x4 conjugate with high-gain and wide bandwidth with DGS. It has a gain value of 10.8 dB. The bandwidth value is greater than the others, about 91 MHz, and the most significant S-Parameter value is -40,659 dB.

C. Specification of Substrate and Conductor Material

The substrates used are as follows: Substrate type FR-4 (lossy), Dielectric constant (ϵ_r) 4.7, Dielectric thickness (h) 1.6 mm, and Thickness of conductor material (t) 0.035 mm.

In Fig. 1, the dimensions of the designed microstrip antenna have antenna dimensions of 172 mm x 82 mm, which have an E-Shape patch with a width of 28.5 mm and a length of 28.5 mm having a distance between patches d or $\lambda/4$. The microstrip antenna has a feed with the W70 Ω having a

width of 1.4 mm and a length of $\lambda/8$. The W50 Ω has a width of 3 mm and a height of $\lambda/40$.

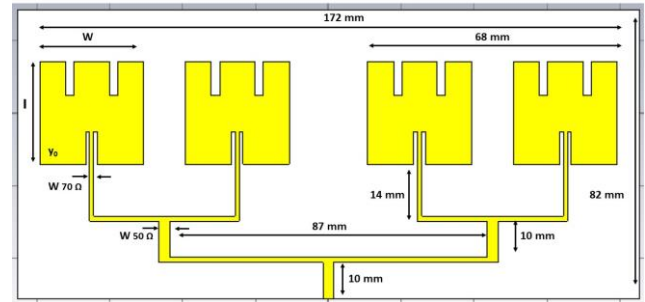


Fig. 1. Patch antenna dimensions.

D. Patch Antenna Optimization Using Complementary

In the first reflector, the concept of this structure is to place the exact dimensions of the patch on the top layer and the slots in the ground layer of the same dielectric substrate to get high gain and wide bandwidth. Based on a reference from research conducted [18], which examined the increase in bandwidth values with the added same DGS slot as the patch in the top layer or complementary as shown in Fig. 2.

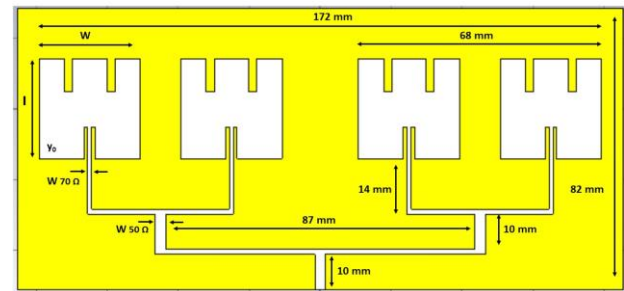


Fig. 2. First reflector (ground).

E. Patch Antenna Optimization Using the DGS Method

The second reflector optimization uses a modified DGS plus "+" and adjustments, as illustrated in Fig. 3. Modification of DGS plus "+" concerning increased bandwidth and radiation on patch antennas to efficient layered for microstrip antenna [19]. Modifying the DGS approach's reflector may increase the gain value and bandwidth.

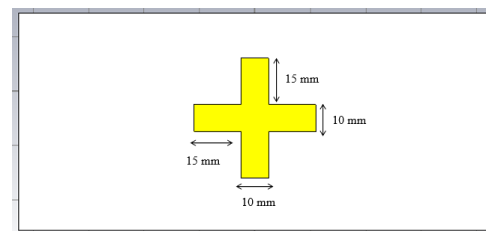


Fig. 3. Second reflector.

The simulation results observed from the final results include Return Loss (S_{11}), bandwidth, Voltage Standing Wave Ratio (VSWR), radiation pattern, polarization, bandwidth, and the magnitude of the gain of the antenna design.

III. MEASUREMENT AND ANALYSIS OF ANTENNA PARAMETERS

Measurements using a vector network analyzer, as shown in Fig. 4. Antenna performance measurements include S Parameter, Gain, and Radiation Pattern testing. The S-parameter test determines several parameters, such as bandwidth and returns loss (S_{11} , S_{21} , and VSWR).

Antenna gain testing using Vector Network Analyzer (VNA) in ports one and two. Installing the intended antenna on port one and a monopole antenna on port 2 is the test procedure through radiation pattern testing, the form of the antenna beam pattern in both the horizontal and vertical planes.

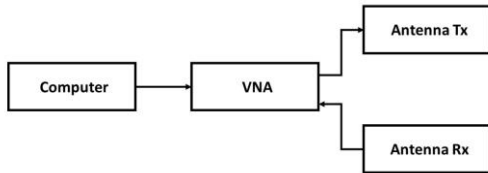


Fig. 4. S-Parameter measurement.

IV. EXPERIMENTAL RESULTS AND DISCUSSION

Figure 5 shows the result of antenna manufacturing. The antenna uses two substrates consisting of one single layer substrate and one double layer substrate for the feed channel and ground. The use of these two substrates follows the double reflector technique, which utilizes two substrates separated by an air aperture between the two substrates. The connector used in the supply is an SMA Female connector with an impedance of 50 ohms at the end of the antenna supply line.

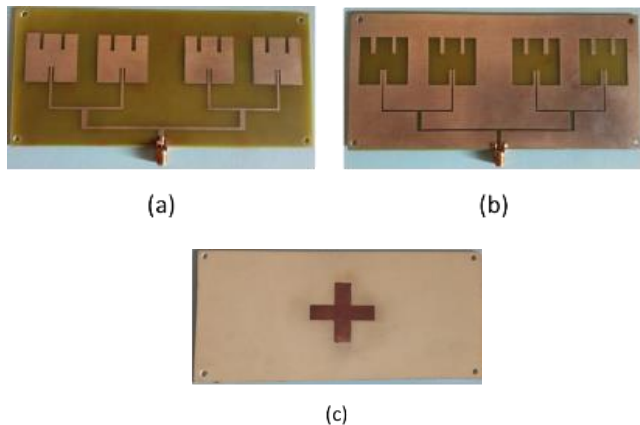


Fig. 5. Antenna fabrication results, (a) top view, (b) first reflector, (c) second reflector.

A. S-Parameter Test Results

From Fig. 6, the return loss value in the simulation at the center frequency of 2450 MHz is -40.659 dB, and the results of the antenna design can work well at a frequency of 2435 MHz of -30.117 dB. This value indicates that the designed antenna can still work well at a frequency of 2435 MHz, following the standard category of both antennas, which has $S_{11} < -10$ dB and VSWR meets the requirements of $1 \leq \text{VSWR} < 2$.

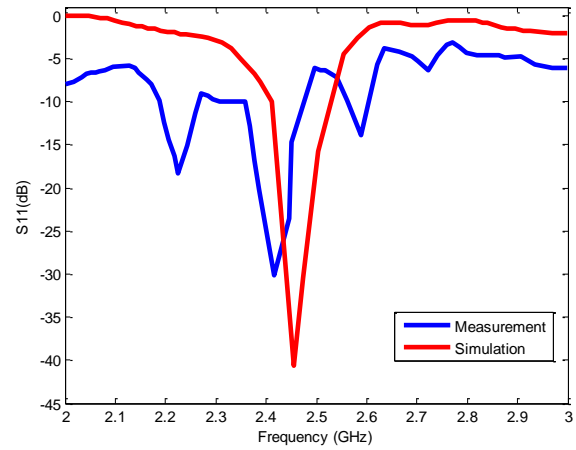


Fig. 6. S_{11} Test Results

The value obtained in this S-Parameter measurement has a different value compared to the simulation results. The simulation process produces S_{11} of 40.659 dB, VSWR of 1.48, and a bandwidth of 40 MHz in the frequency range of 2440 MHz to 2480 MHz. The attenuation of the cable and connector and the frequency shift make the value difference between simulation and fabrication. In addition, the influence of air in the gap between the substrates is due to the antenna performance.

B. VSWR

The measurement results show an excellent VSWR value in the frequency range of 2410 MHz to 2470 GHz. Based on measurement results, the bandwidth of the designed antenna is 60 MHz, as illustrated in Fig. 7.

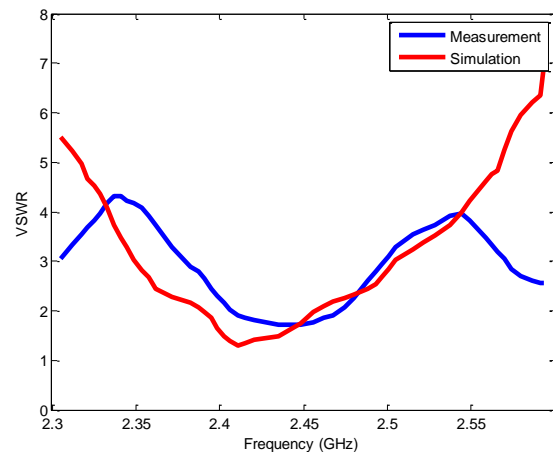


Fig. 7. VSWR value

C. Gain Test Results

Gain measurement determines how much power can be emitted by the antenna at a certain angle. This study obtains the gain value by analyzing the coefficient S_{21} . The value of S_{21} is obtained based on the value shown by the designed antenna to the reference antenna (antenna monopole). From the importance of S_{21} , a calculation result using to get the designed antenna's gain value.

Before testing the gain of the designed antenna, first, know the power of the reference antenna. This antenna serves as a comparison so that the measured gain is the same as the comparison gain or $G_t = G_r$. The following equation calculates the measured reference antenna where S_{21} is -37,358 dB.

D. Radiation Pattern

From the measurement results of the antenna in the horizontal and vertical planes, the radiation pattern is relatively the same as the radiation pattern of the simulation results. A comparison of the designed antenna radiation pattern results with the simulated radiation pattern is in Fig. 8 and Fig. 9.

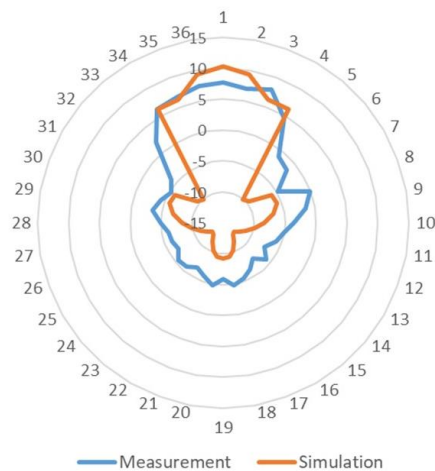


Fig. 8. Horizontal radiation pattern

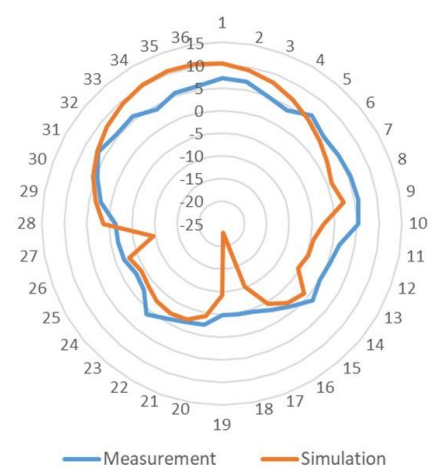


Fig. 9. Vertical Radiation pattern

The radiation pattern of the designed antenna tends to have a smaller radiation pattern than the simulated radiation pattern. Although there are still variances, the value may differ from the mark displayed by each primary lobe and side lobe at each corner. Several factors cause this difference in simulation and measurement. In the simulation, the parameters generated are in perfect form. In contrast, in the measurement process, the parameters can be affected by the environment, and materials used in the manufacturing and measurement processes.

The radiation pattern shown by this design antenna shows the shape of the radiation pattern with a directional direction, namely the direction of the antenna beam leading to a certain angle shown in the main lobe.

CONCLUSIONS

Based on the measurement results of the E-shape array microstrip patch antenna, there is a slight difference in center frequency, which in the simulation obtained a gain value of 10.83 dB, VSWR of 1.48, bandwidth of 40 MHz, and S_{11} of -40,569 dB with a center frequency of 2450 MHz. Meanwhile, the measurement results obtained a gain value of 7.139 dB, VSWR of 1.7, a bandwidth of 60 MHz, S_{11} of -30.117 dB at a center frequency of 2435 MHz, and It has linear polarization.

REFERENCES

- [1] D. A. Pankratev, A. A. Samsonov, and A. D. Stotckaia, "Wireless data transfer technologies in a decentralized system," 2019, doi: 10.1109/EICoRus.2019.8656671.
- [2] Y. Amarasinghe *et al.*, "Broadband wide-angle terahertz antenna based on the application of transformation optics to a Luneburg lens," *Sci. Rep.*, vol. 11, no. 1, 2021, doi: 10.1038/s41598-021-84849-8.
- [3] I. Nurfitri and C. Apriono, "Rectangular microstrip array antenna for enhancing terahertz imaging quality," 2019, doi: 10.1109/ICIRD47319.2019.9074652.
- [4] A. Sani, A. Ramadani, and Suherman, "Microstrip array design and implementation for WiFi external antenna," 2020, doi: 10.1109/ELTICOM50775.2020.9230494.
- [5] Z. Wang, S. Liu, and Y. Dong, "Low-Profile Circularly Polarized Antenna with Wide AR Beam-width for WIFI Application," 2020, doi: 10.1109/IWS49314.2020.9359932.
- [6] A. S. Sudi Mariyanto, M. Irfan, S. Ariessaputra, and O. M. Cahyo Mustiko, "Design and realization of microstrip antenna for GPS application using proximity coupled techniques," *Proceeding 2017 11th Int. Conf. Telecommun. Syst. Serv. Appl. TSSA 2017*, vol. 2018-Janua, pp. 1-4, 2018, doi: 10.1109/TSSA.2017.8272922.
- [7] D. K. Kong, J. Kim, D. Woo, and Y. J. Yoon, "Broadband Modified Proximity Coupled Patch Antenna with Cavity-Backed Configuration," *J. Electromagn. Eng. Sci.*, vol. 21, no. 1, 2021, doi: 10.26866/jees.2021.21.1.8.
- [8] S. P. Pan, Y. Feng, L. Qi, P. Chen, J. W. Li, and G. S. Li, "Design of Dual-band Frequency Reconfigurable Microstrip Antenna Array," 2020, doi: 10.1109/CSRSWTC50769.2020.9372521.
- [9] J. Zhang, R. Das, Q. H. Abbasi, N. Mirzai, J. Mercer, and H. Heidari, "Dual-band Microstrip Patch Antenna for Fully-Wireless Smart Stent," 2021, doi: 10.1109/APS/URSI47566.2021.9703759.
- [10] K. K. Giri, R. K. Singh, K. Mamata, and A. K. Shrivastava, "A Theoretical Survey on Patch Antenna for Wideband Communication," *Int. J. Res. Eng. Sci. Manag.*, vol. 3, no. 11, 2020, doi: 10.47607/ijresm.2020.376.
- [11] V. R. N., "Bandwidth Enhancement of Novel E-shaped Microstrip Patch Antenna with FR4 Substrate at 2.45GHz," *Rev. Gestão Inovação e Tecnol.*, vol. 11, no. 4, 2021, doi: 10.47059/revistageintec.v11i4.2168.
- [12] Y. Yulindon, N. A. Samsudin, and R. Efendi, "Optimization of E-shaped microstrip patch antenna using particle swarm optimization (PSO) for wideband application," *Int. J. Intell. Eng. Syst.*, vol. 13, no. 4, 2020, doi: 10.22266/IJIES2020.0831.27.
- [13] A. Ali, N. Pirzada, M. M. Jawaid, and S. A. Memon, "Design and simulation of a rectangular E-shaped microstrip patch antenna for RFID based intelligent transportation," *Int. J. Adv. Comput. Sci. Appl.*, vol. 9, no. 4, 2018, doi: 10.14569/IJACSA.2018.090426.
- [14] C. M. O. Muvianto, Pahurrozi, S. Ariessaputra, and S. Malekpour, "Optimization of Grid Antenna 2.4 GHz Using Grid Reflector and Yagi Antenna's Feed Modification," *2018 2nd Int. Conf. Appl. Electromagn. Technol. AEMT 2018*, pp. 24-28, 2018, doi: 10.1109/AEMT.2018.8572325.
- [15] K. Debbarma and R. Bhattacharjee, "Pattern Shifting and Size Control in Offset Reflector Antennas with Microstrip Array as

- Matched Feed," 2020, doi: 10.23919/EuCAP48036.2020.9135376.
- [16] N. L. Nhlengethwa and P. Kumar, "Fractal microstrip patch antennas for dual-band and triple-band wireless applications," *Int. J. Smart Sens. Intell. Syst.*, vol. 14, no. 1, 2021, doi: 10.21307/IJSSIS-2021-007.
- [17] Y. Dong *et al.*, "Broadband circularly polarized filtering antennas," *IEEE Access*, vol. 6, 2018, doi: 10.1109/ACCESS.2018.2883494.
- [18] J. C. Dash, G. P. Mishra, and B. B. Mangaraj, "Design of dual band patch antenna with bandwidth enhancement using complementary defected ground structure," 2016, doi: 10.1109/IC3I.2016.7917973.
- [19] P. R. Prajapati, A. Patnaik, and M. V. Kartikeyan, "Design and characterization of an efficient multi-layered circularly polarized microstrip antenna," *Int. J. Microw. Wirel. Technol.*, vol. 8, no. 7, pp. 1101–1109, Nov. 2016, doi: 10.1017/S1759078715000549.

Detrended Fluctuation Analysis Associated with the M5.1 Earthquake Precursor in Banten, Indonesia

Cinantya Nirmala Dewi

*Research Center for Geological
Disaster*

*National Research and Innovation
Agency (BRIN)*

Tangerang Selatan, Indonesia
cinanthia@gmail.com

Febty Febriani

*Research Center for Geological
Disaster*

*National Research and Innovation
Agency (BRIN)*

Tangerang Selatan, Indonesia
febty82@gmail.com

Titi Anggono

*Research Center for Geological
Disaster*

*National Research and Innovation
Agency (BRIN)*

Tangerang Selatan, Indonesia
titi.anggono@gmail.com

Syuhada

*Research Center for Geological
Disaster*

*National Research and Innovation
Agency (BRIN)*

Tangerang Selatan, Indonesia
hadda9@gmail.com

Aditya Dwi Prasetyo

*Research Center for Geological
Disaster*

*National Research and Innovation
Agency (BRIN)*

Tangerang Selatan, Indonesia
adityadprasetyo@gmail.com

Mohammad Hasib

*Research Center for Geological
Disaster*

*National Research and Innovation
Agency (BRIN)*

Tangerang Selatan, Indonesia
mohammadhasib07@gmail.com

Hendra Suwarta Suprihatin

*Geophysical Potential and Time Signal
Division*

*Indonesian Meteorological,
Climatological, and Geophysical
Agency (BMKG)*

Jakarta Pusat, Indonesia
hendrasuwarta60@gmail.com

Suaidi Ahadi

*Geophysical Potential and Time Signal
Division*

*Indonesian Meteorological,
Climatological, and Geophysical
Agency (BMKG)*

Jakarta Pusat, Indonesia
suaidi.ahadi@bmk.go.id

Muhamad Syirojudin

*Geophysical Potential and Time Signal
Division*

*Indonesian Meteorological,
Climatological, and Geophysical
Agency (BMKG)*

Jakarta Pusat, Indonesia
syirojudin.bmk@gmail.com

Hasanudin

*Geophysical Potential and Time Signal
Division*

*Indonesian Meteorological,
Climatological, and Geophysical
Agency (BMKG)*

Jakarta Pusat, Indonesia
hasan.geologi@gmail.com

Indah Marsyam

*Geophysical Potential and Time Signal
Division*

*Indonesian Meteorological,
Climatological, and Geophysical
Agency (BMKG)*

Jakarta Pusat, Indonesia
indahmarsyam.vc@gmail.com

Mohammad Nafian

*Physics Department
Syarif Hidayatullah State Islamic
University*

Tangerang Selatan, Indonesia
nafianlia@gmail.com

Suwondo

*Physics Department
Syarif Hidayatullah State Islamic
University*

Tangerang Selatan, Indonesia
suwondo.geo@gmail.com

Abstract—We studied the behavior of scaling components associated with the M5.1 earthquake that occurred in Banten on 7 July 2020 by using the Detrended Fluctuation Analysis (DFA). DFA is a powerful technique to assess the self-similarity of fractals in time series data. The time series data were obtained from Sukabumi (SKB) geomagnetic observatory station during April - August 2020. We only used the nighttime data (16.00-21.00 UTC) for our analysis to reduce the artificial noise due to human activities. The results revealed long-term correlations during the whole observation period. Moreover, we also used the results of our previous study using the Fast Fourier Transform (FFT) for further analysis in this paper. The combined analysis of the spectral density ratio (SDR) value obtained from FFT and the scaling exponent value obtained from DFA showed the presence of EQ precursors from the end of April until early June 2020.

Keywords—ULF geomagnetic, fractal analysis, scaling exponent, earthquake forecast

I. INTRODUCTION

The western part of Java Island consists of large cities which are densely populated because they become the center of the economy and industry. Geologically, this area is located at the confluence of the Eurasian and Australian plates [1]. As a result, in this area earthquakes (EQs) often occur which have the potential to cause casualties and material losses. It was recorded that 3,243 EQs occurred in West Java from 2009 - 2019. The number of EQs was the highest compared to other provinces in Java [2]. Based on United States Geological Survey (USGS) data, there were 3 EQs in western Java with magnitude (M) more than 5 occurred in 2020. These data reveal that western Java is a seismically active area. Therefore, it is necessary to reduce the risk of EQ disasters, such as by studying the characteristics of EQ precursors in the western part of Java Island using geomagnetic data.

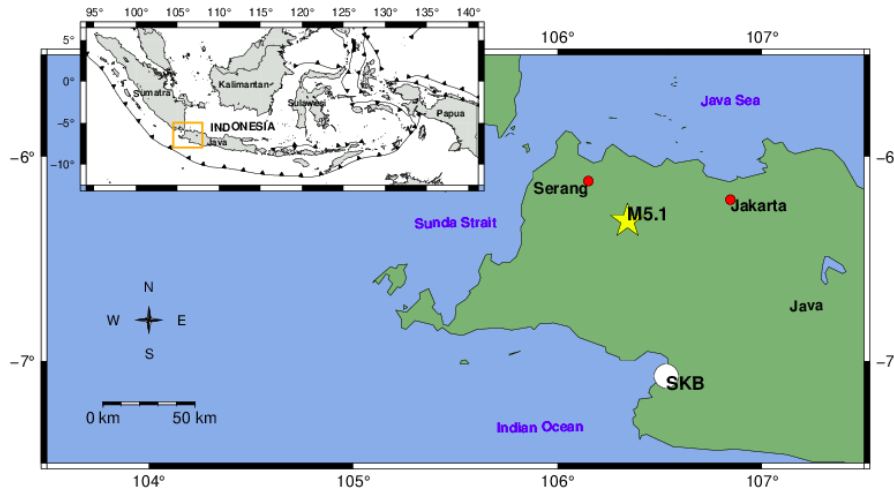


Fig. 1. The locations of the M5.1 EQ and SKB station

Analysis of Ultra Low Frequency (ULF) geomagnetic data can be applied as an approach to determine short-term EQ precursor [1]-[9]. Since ULF (<1 Hz) has low attenuation and can penetrate deep areas, it may contain information about the EQ preparation process in the lithosphere, such as micro fractures near the hypocenter, or nonlinearity lithospheric dynamics concerning EQ [10], [11]. In our previous study, EQ precursors from three EQs with $M > 5$ that occurred in 2020 were analyzed using the Fast Fourier Transform (FFT) analysis. We get the results that the M5.1 EQ that occurred on 7 July 2020 showed the most significant ULF anomaly compared to other EQs [12]. However, a multidisciplinary analysis is still needed to confirm that the ULF geomagnetic anomaly is related to the M5.1 EQ because EQ preparation is a complex process.

This study was conducted to confirm the results of the EQ precursor found in previous studies with the FFT analysis for the M5.1 EQ based on Sukabumi geomagnetic observatory (SKB) data. The location of the EQ and SKB shown in Fig.1. The ULF geomagnetic anomalies related to seismogenic processes should contain fracture process information that occurs in the lithosphere. Considering that fracture processes have fractal behavior, it is necessary to analyze the disturbances in ULF fractal characteristics [10], [13], [14]. A powerful technique that can be used to identify the degree of self-similarity of fractals in a non-stationary time series is the detrended fluctuation analysis (DFA) [15]. DFA analysis is advantageous for analyzing time series to find long-range correlations of the data [16], [17]. It has been extensively applied to ULF geomagnetic data to reveal that scaling disturbances in ULF geomagnetic data before the EQ are related to the EQ event itself [16]-[22]. Therefore, we applied the DFA method over the same timeframe as in the case of FFT analysis to obtain a comprehensive analysis in the evaluation of the M5.1 EQ precursors.

II. METHODS

We analyzed the M5.1 EQ that took place in Rangkasbitung on 7 July 2020 at 04:44:13 UTC. The EQ epicenter is located at $6.31^{\circ}\text{S } 106.34^{\circ}\text{E}$ with a depth of 96.85 km. The magnetometer located SKB belonging to the Indonesian Meteorological, Climatological, and Geophysical Agency (BMKG) with an epicenter distance less than 100 km. The recorded time series data is represented in

horizontal and vertical components (X, Y, and Z) with a sampling frequency of 1 Hz.

We take 5 months of daily geomagnetic data from April to August 2020 from SKB. Then, we selected only the nighttime (16.00-21.00 UTC) data for analysis to reduce the artificial noise due to human activities. An example of three components of geomagnetic nighttime data on 20 June 2020 can be seen in Fig. 2. We used DFA analysis to find the exact scaling behavior of non-stationary data because DFA is capable to detect the dynamic features and prevent non-stationary artifacts [20], [23]-[25].

DFA is applied in a time series data $x(i)$ with N length and the profile is determined by integrating the time series (1):

$$y(k) = \sum_{i=1}^k [x_i - x_{ave}] \quad (i = 1, \dots, N) \quad (1)$$

where x_{ave} is the average of the time series data. Then, the profile $y(k)$ is divided into non-overlapping segments with equal length n . We performed the least square polynomial to each segment to represent the trend of the segment. The integrated time series $y(k)$ is detrended by subtracting the local trend $y_n(k)$ in each segment. The root mean square fluctuation of the integrated and detrended time series is calculated by (2):

$$F(n) = \sqrt{\frac{1}{N} \sum_{k=1}^N [y(k) - y_n(k)]^2} \quad (2)$$

To find the relationship between $F(n)$ and n , we calculate (2) over all segments. Generally, $F(n)$ will increase according to the increase of n . The power-law scaling defines the relationship between $F(n)$ and n will obey (3):

$$F(n) \propto n^{\alpha} \quad (3)$$

The scaling exponent α is the slope of the line fitting $\log F(n)$ and $\log n$ that represent its correlation in the time series data. The α value shows the presence of long-range correlation or not. An $\alpha > 0.5$ means the presence of persistent long-range correlations, and $\alpha < 0.5$ means the presence of anti-persistent long-range correlations [20], [23], [24].

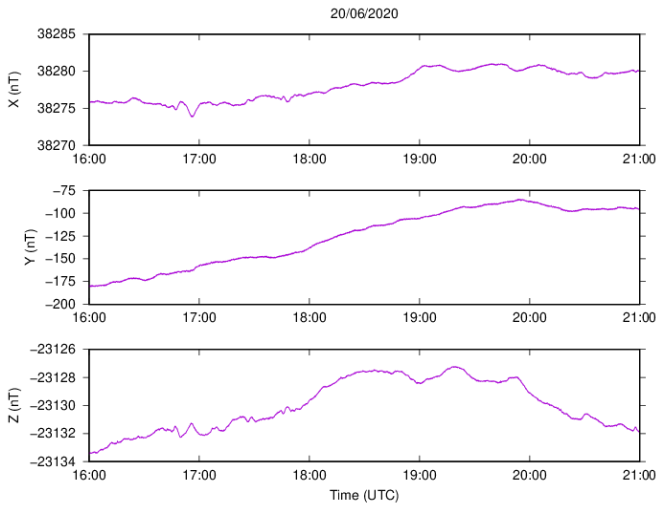


Fig. 2. Time series observed in X, Y, and Z components at nighttime (16.00-21.00 UTC) from SKB on 20 June 2020.

III. RESULT AND DISCUSSION

We analyzed the ULF geomagnetic data observed at SKB from 1 April 2020 until 31 August 2020. Fig. 3 exhibits an

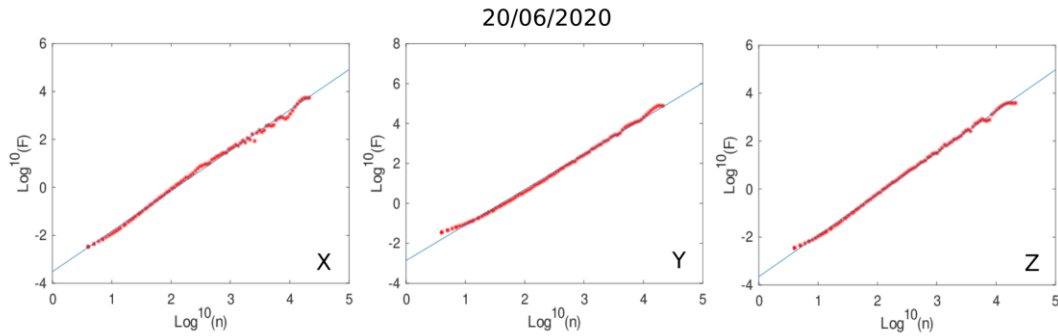


Fig. 3. An example of $\log F(n)$ versus $\log n$ plots of the X, Y, and Z components for the observed data on 20 June 2020

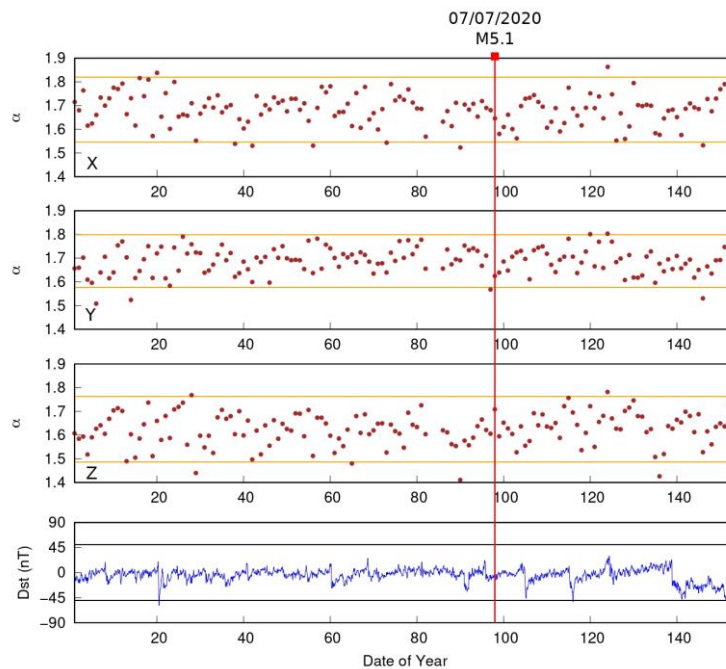


Fig. 4. Time variation of the α values in X, Y, and Z components from 1 April 2020 until 31 August 2020. The red vertical line shows the occurrence of M5.1 EQ and the orange horizontal lines show the threshold of the data

example of the fluctuation function computed with the DFA method of the X, Y, and Z components. Generally, it informs about the relation of $F(n)$ and n which is in the form of a straight line and almost uniform with a single scaling exponent for all timescales.

Fig. 4 illustrates the time variation of the scaling exponents α of the X, Y, and Z components during the observation times. The red vertical line on 7 July 2020 denotes the EQ day and the orange horizontal lines denote the threshold of the data (mean $\pm 2\sigma$, σ is the standard deviation). The scaling exponents are given from the top for X, Y, and Z components. The bottom panel is the Dst index that represents the global geomagnetic activity obtained from the World Data Center for Geomagnetism, Kyoto University. The high geomagnetic activity ($Dst \leq -50$ nT or $Dst \geq 50$ nT) may disturb the geomagnetic data. From the Dst data analysis, it can be seen that almost the whole observation period is quiet days so the global geomagnetic disturbances can be minimized. We observed that the average α value is greater than 0.5 that indicating a long-range correlation. These fractal properties are associated with transient electrical signal emission due to stress variations in the focal area before an EQ [21].

We sampled the results of our previous study for this EQ using the FFT analysis in the same period to compare with the results of the DFA analysis. Our previous study calculated the spectral density ratio (SDR) of the S_z/S_G over

0.01 - 0.06 Hz to find the optimum frequency for precursor detection [12]. We have compared the S_z/S_G values of all frequencies (0.01 Hz - 0.06 Hz) with the scaling exponents of the Z component as shown in Fig. 5.

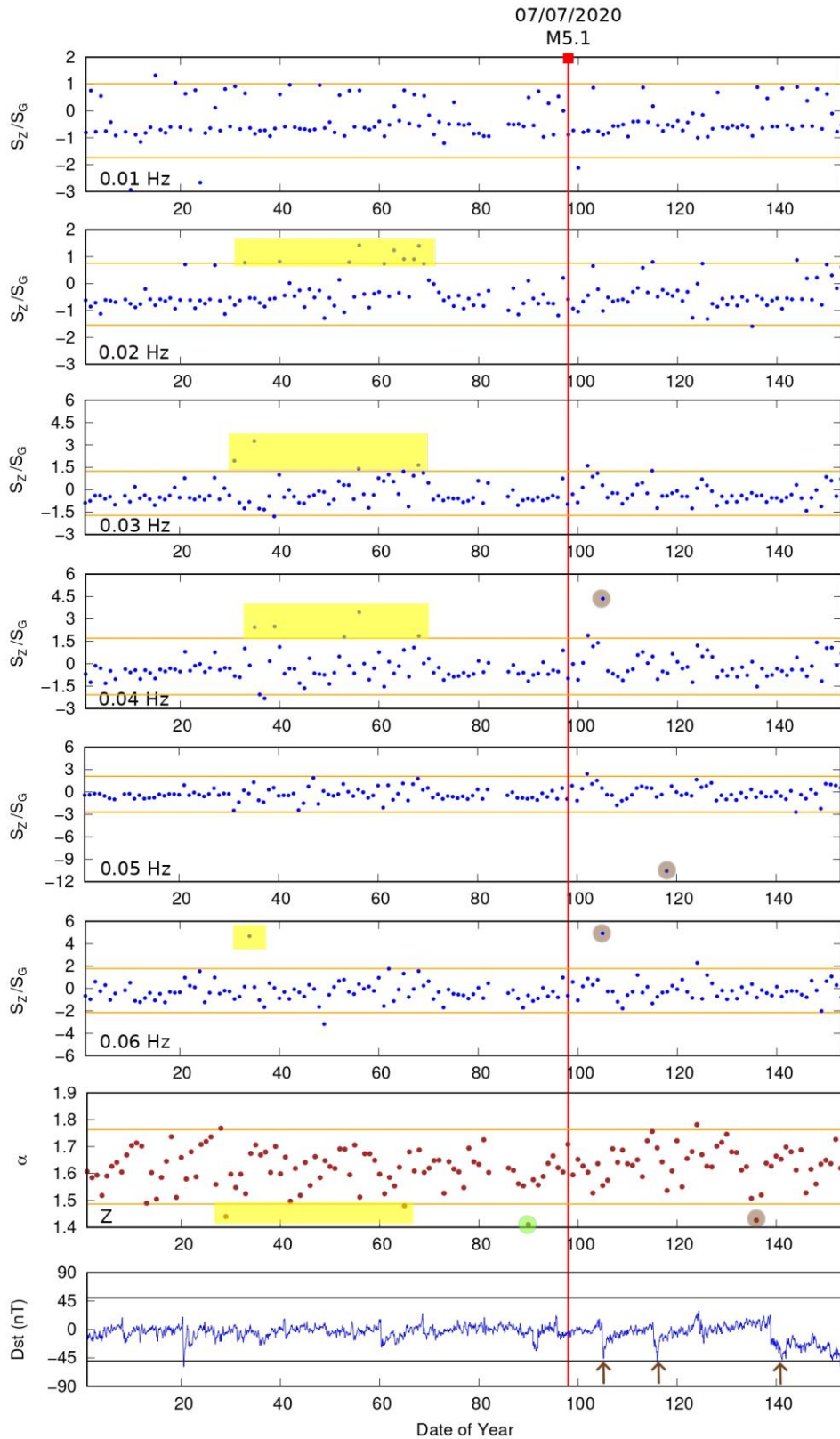


Fig. 5. Time variation of the S_z/S_G values over 0.01 - 0.06 Hz compared with the α values of the Z components from 1 April 2020 until 31 August 2020. The red vertical line shows the occurrence of M5.1 EQ and the orange horizontal lines show the threshold of the data. The α and S_z/S_G anomalies that occur simultaneously and related to the EQ precursor are marked as yellow area, while the α anomaly occurring before EQ without S_z/S_G anomaly is marked with a green circle. Meanwhile, the α and S_z/S_G anomalies related to the high global geomagnetic activity (brown arrows) are marked with brown circles

The anomalies from S_z/S_G and α values were found at almost the same period marked with the yellow areas at frequencies of 0.02, 0.03, 0.04, and 0.06 Hz which may indicate a relationship in predicting EQ precursors. In general, the above-mentioned frequencies indicate that if there is an increase in S_z/S_G exceeding the threshold, there will be a decrease in the α value which is smaller than the threshold at almost the same time. These characteristics occur from the end of April (2.5 months before EQ) to early June 2020 (1 month before EQ) during the quiet days of global geomagnetic activity. The anomalies in the S_z/S_G and α values described above are thought to be related to the EQ preparation process. We also found an anomaly in the α value smaller than the threshold (marked with a green circle) without an increase in the S_z/S_G value at 8 days before the EQ when the Dst value showed normal global geomagnetic activity. Meanwhile, there are also some significant anomalies in the S_z/S_G and α values after the EQ event (marked with the brown circles) which occurs when the Dst value drops significantly to the threshold (marked with the brown arrows) which means there is a high global geomagnetic activity, so it is not related to EQ activity.

Our result is similar to previous research which found the decrease of the α values at the same time as an increase in SDR values around 20 days before the M7.5 EQ (2009) near the Pelabuhan Ratu station, West Java, Indonesia [22]. Another case study for the M6.1 EQ (2018) which occurred about 100 km from the Banten geomagnetic observatory showed the geomagnetic anomalies were found about 2 weeks before EQ [26], [27]. Moreover, long duration of lead times also have been found 5 months before the M7.4 Guerrero-Oaxaca EQ [21] and 2 months before the M6.6 EQ in Japan [28]. The presence of anomalies that exceed the threshold when there is no high global geomagnetic activity is the characteristic of the EQ precursors detection from ULF geomagnetic data. However, this research is still preliminary and suggestive, it requires a comprehensive statistical analysis and approaches from other methods to reveal the precursors before the EQ.

IV. CONCLUSION

We have analyzed the nighttime ULF geomagnetic data recorded from SKB during April - August 2020 by using the DFA analysis. We tried to find the characteristics of the α values before the M5.1 EQ took place in Rangkasbitung on 7 July 2020. The results of the DFA analysis revealed that during the whole observation period, the α values indicate a long-range correlation. Moreover, the combination of the SDR value from our previous study and the α value obtained from this study found the presence of the EQ precursor starting from 2.5 - 1 month before the EQ. This is indicated by an increase in the SDR value exceeding the threshold that occurred in the same period with a decrease in the α value smaller than the threshold. Nevertheless, our research is still preliminary and needs other perspectives analysis of precursor detection.

ACKNOWLEDGMENT

This study is supported by the L'Oreal-UNESCO for Women in Science Program and the Disaster Research seed grant of the National Research and Innovation Agency (DIPA OR KM BRIN No. SP DIPA-124.01.1.690501/2022).

REFERENCES

- [1] S. Widiyantoro, P. Supendi, A. Ardianto, A.W. Baskara, C.A. Bacon, R. Damanik, N. Rawlinson, E. Gunawan, D.P. Sahara, Z. Zulfakriza and Y.M. Husni. Implications for fault locking south of Jakarta from an investigation of seismic activity along the Baribis fault, northwestern Java, Indonesia. *Scientific reports*, 12(1), pp.1-10 (2022).
- [2] Sabtaji. *Buletin Meteorologi, Klimatologi, dan Geofisika*, 7, pp. 31-46 (2020).
- [3] M. Hayakawa, A. Schekotov, J. Izutsu and A.P. Nickolaenko. Seismogenic effects in ULF/ELF/VLF electromagnetic waves. *Int. J. Electron. Appl. Res.*, 6(2), pp.1-86 (2019).
- [4] S.M. Potirakis, A. Schekotov, Y. Contoyiannis, G. Balasis, G.E. Koulouras, N.S. Melis, A.Z. Boutsis, M. Hayakawa, K. Eftaxias and C. Nomicos. On possible electromagnetic precursors to a significant earthquake (Mw= 6.3) occurred in Lesvos (Greece) on 12 June 2017. *Entropy*, 21(3), p.241 (2019).
- [5] P. Han, J. Zhuang, K. Hattori, C.H. Chen, F. Febriani, H. Chen, C. Yoshino and S. Yoshida. Assessing the potential earthquake precursory information in ULF magnetic data recorded in Kanto, Japan during 2000–2010: Distance and magnitude dependences. *Entropy*, 22(8), p.859 (2020).
- [6] S. Warden, L. MacLean, J. Lemon and D. Schneider. Statistical analysis of pre-earthquake electromagnetic Anomalies in the ULF Range. *Journal of Geophysical Research: Space Physics*, 125(10), p.e2020JA027955 (2020).
- [7] Singh, and Y. Hobara. Simultaneous study of VLF/ULF anomalies associated with earthquakes in Japan. *Open Journal of Earthquake Research*, 9(2), pp.201-215 (2020).
- [8] K.A. Yusof, M. Abdullah, N.S.A. Hamid, S. Ahadi, and A. Yoshikawa. Correlations between earthquake properties and characteristics of possible ULF geomagnetic precursor over multiple earthquakes. *Universe*, 7(1), p.20 (2021).
- [9] X. Yao, W. Wang and Y. Teng. Detection of Geomagnetic Signals as Precursors to Some Earthquakes in China. *Applied Sciences*, 12(3), p.1680 (2022).
- [10] S.M. Potirakis, M. Hayakawa and A. Schekotov. Fractal analysis of the ground-recorded ULF magnetic fields prior to the 11 March 2011 Tohoku earthquake (MW= 9): discriminating possible earthquake precursors from space-sourced disturbances. *Natural Hazards*, 85(1), pp.59-86 (2017).
- [11] M. Hayakawa M and Y. Ida. Fractal (mono- and multi-) analysis for the ULF data during the 1993 Guam earthquake for the study of prefracture criticality. *Curr Dev Theory Appl Wavelets* 2(2), pp.159–174 (2008).
- [12] C.N. Dewi, F. Febriani, T. Anggono, Syuhada, M. Hasib, A.D. Prasetio, A. Sulaiman, H.S. Suprihatin, S. Ahadi, M. Syirojudin, Hasanudin and I. Marsyam. The optimum frequency for detecting earthquake precursors based on Ultra-Low Frequency (ULF) geomagnetic data from Sukabumi (SKB) station. *AIP Conference Proceedings*, in press.
- [13] M. Hayakawa, T. Ito and N. Smirnova N. Fractal analysis of ULF geomagnetic data associated with the Guam earthquake on August 8, 1993. *Geophys Res Lett*, 26(18), pp. 2797–2800 (1999).
- [14] NA. Smirnova and M. Hayakawa. Fractal characteristics of the ground-observed ULF emissions in relation to geomagnetic and seismic activities. *J Atmos Sol Terr Phys*, 69, pp. 1833–1841 (2007).
- [15] C-K. Peng, S. Havlin, H.E. Stanley and A.L. Goldberger AL. Quantification of scaling exponents and crossover phenomena in nonstationary heartbeat time series. *Chaos*, 5, pp. 82–87 (1995).
- [16] L. Guzmán-Vargas, C. Carrizales-Velazquez, I. Reyes-Ramírez, J. Fonseca-Campos, A.D.L. Rosa-Galindo, V.O. Quintana-Moreno, J.A. Peralta and F. Angulo-Brown. A comparative study of geoelectric signals possibly associated with the occurrence of two Ms> 7 EQs in the South Pacific Coast of Mexico. *Entropy*, 21(12), p.1225 (2019).
- [17] T. Kataoka, T. Miyaguchi and T. Akimoto. Detrended fluctuation analysis of earthquake data. *Physical Review Research*, 3(3), p.033081 (2021).
- [18] L. Flores-Márquez, J. Márquez-Cruz, A. Ramírez-Rojas, G. Galvez-Coyt and F. Angulo-Brown. A statistical analysis of electric self-potential time series associated to two 1993 earthquakes in Mexico. *Natural Hazards and Earth System Sciences*, 7(5), pp.549-556, (2007).

- [19] L. Guzman-Vargas, A. Ramírez-Rojas, R. Hernández-Pérez and F. Angulo-Brown. Correlations and variability in electrical signals related to earthquake activity. *Physica A: Statistical Mechanics and its Applications*, 388(19), pp.4218-4228 (2009).
- [20] L. Telesca, V. Lapenna, M. Macchiato and K. Hattori. Investigating non-uniform scaling behavior in Ultra Low Frequency (ULF) earthquake-related geomagnetic signals. *Earth and Planetary Science Letters*, 268(1-2), pp.219-224 (2008).
- [21] Ramírez-Rojas, E.L. Flores-Márquez, L. Guzman-Vargas, G. Gálvez-Coyt, L. Telesca and F. Angulo-Brown. Statistical features of seismoelectric signals prior to M7. 4 Guerrero-Oaxaca earthquake (México). *Natural Hazards and Earth System Sciences*, 8(5), pp.1001-1007 (2008).
- [22] F. Febriani, P. Han, C. Yoshino, K. Hattori, B. Nurdianto, N. Effendi, I. Maulana, Suhardjono and E. Gaffar. *Nat. Hazards Earth Syst. Sci*, 14, pp. 789–798 (2014).
- [23] C.-K. Peng, S. V. Buldyrev, S. Havlin, M. Simons, H. E. Stanley and A. L. Goldberger, Mosaic organization of DNA nucleotides, *Phys. Rev. E*, 49, 1685 (1994).
- [24] Y.I. Ida, M. Hayakawa and K. Gotoh. Multifractal analysis for the ULF geomagnetic data during the Guam earthquake. *IEEJ Transactions on Fundamentals and Materials*, 126(4), pp.215-219 (2006).
- [25] K. Gotoh, N. Smirnova and M. Hayakawa. Fractal analysis of seismogenic ULF emissions. *Physics and Chemistry of the Earth, Parts A/B/C*, 29(4-9), pp.419-424 (2004).
- [26] F. Febriani, T. Anggono, Syuhada, A. D. Prasetyo, C. N. Dewi, A. S. Hak and S. Ahadi, "Investigation of the ultra low frequency (ULF) geomagnetic anomalies prior to the Lebak, Banten earthquake (M=6.1; January 23, 2018)," *AIP Conference Proceedings*, vol. 2256, no. 1, p. 090002 [AIP Publishing, Melville, NY, 2020]
- [27] F. Febriani, S. Ahadi, T. Anggono, Syuhada, C. N. Dewi and A. D. Prasetyo, "Applying Wavelet Analysis to Assess the Ultra Low Frequency (ULF) geomagnetic anomalies prior to the M6. 1 Banten Earthquake (2018)," *IOP Conference Series: Earth and Environmental Science*, vol. 789, no. 1, p. 012064 [IOP Publishing, Bristol, UK, 2021].
- [28] S.T. Uyeda, Y. Nagao, T. Orihara, Yamaguchi and I. Takahashi. Geoelectric potential changes: Possible precursors to earthquakes in Japan. *Proc. Nat. Ac. Sc. (PNAS)*, 97–9, pp.4561–4566 (2000).

LoRa Technology for Communication in Blankspot Areas

L. Ahmad S.Irfan Akbar
Electrical Engineering Department
University of Mataram
Mataram, Indonesia
irfan@unram.ac.id

A. Sjamsjiar Rachman
Electrical Engineering Department
University of Mataram
Mataram, Indonesia
asrachman@unram.ac.id

Misbahuddin
Electrical Engineering Department
University of Mataram
Mataram, Indonesia
misbahuddin@unram.ac.id

Djul Fikry Budiman
Electrical Engineering Department
University of Mataram
Mataram, Indonesia
djulfikry@unram.ac.id

Muhamad Syamsu Iqbal
Electrical Engineering Department
University of Mataram
Mataram, Indonesia
msiqbal@unram.ac.id

Giri Wahyu Wiriasto
Electrical Engineering Department
University of Mataram
Mataram, Indonesia
giriwahuwiriasto@unram.ac.id

Abstract—By 2020, the number of devices connected to the internet has reached 50 billion. By 2030, Cisco estimates that 500 billion devices are connected to the Internet. This increase in number is due to the rapid development of Internet of Things or IoT technology. IoT devices have the advantage of being able to transmit data over long distances but require low consumption of electrical energy sourced from batteries. This study utilizes the ability of the LoRa SX1276 IoT device to send messages in the blank spot area. On the island of Lombok, there are still areas that are still not covered by communication signals, both GSM signals and internet signals, due to geographical conditions located in hilly or forest areas. This study also uses ESP32 which can interact with the LoRa SX1276 device. The smart phone connects to the ESP32 through the web server it provides, through the HTML page the user sends a message which LoRa will forward to the receiving device. The test results in the field show that the LoRa and ESP32 communication devices are able to send messages up to a distance of 1.1 km in the blankspot area of hills and forests along the road.

Keywords—IoT, LoRa SX1276, Blank spot, ESP32, Message

I. INTRODUCTION

Communication plays an important role in everyone's life to interact with the surrounding environment. As technology advances, the use of digital communication is increasing rapidly. Transfer of information has become easier to do. For example, information about volcanic activity can be quickly passed on to the appropriate authorities. But there are still places that are still not reached by communication signals called blank spots, where we cannot transmit information. So the question is how to transmit information from that place, such as in the forest or in remote areas. There are several technologies to build a means of communication such as Wi-Fi, GSM or Bluetooth. But based on [1] one of the main problems in building communication facilities in rural areas is the lack of availability of reliable and cost effective. On the other hand, LPWAN offers wireless communication technology which is low cost, long coverage in license-free frequency band and consumes less power [2] LoRa is a recently developed LPWAN technology based on the spread spectrum technique. LoRa uses the entire channel bandwidth to broadcast a signal which makes it resistant to channel interference, long-range relative frequency, Doppler effects, and fading. LoRa characteristics are based on three transmission parameters: Code Rate (CR), Spreading Factor

(SF) and Bandwidth (BW) [3]. This technology is bidirectional, and consumes less power used by sensors when sending or receiving data. LoRa can cover almost 15-20 km and work for years on battery [4]. But LoRa also has the disadvantage of a small data rate to cover long distances. LoRa has a maximum data rate of 50 kbps [5], therefore LoRa cannot transmit video or audio data, LoRa devices can only transmit text data [6].

In this study, the ESP32 MCU Node modem and LoRa Transceiver SX1276 are used, these devices will be used to send messages to blankspot areas that have not been reached by GSM infrastructure and internet signals. Smartphones that are always carried by everyone will be used as an interface to send messages. The ESP32 MCU node is responsible for connecting the smartphone with the LoRa SX1276 device. ESP32 also provides a web server that can be accessed via a web browser on a smartphone so that messages typed via a smartphone can be sent via LoRa Devices. This research will also measure the range that can be taken by the LoRa device when sending text messages in the blankspot area, because sending messages will be carried out along the road through winding hills with forests on both sides of the road.

The SX1276 provides long range spread spectrum communication and high interference immunity while carrying current consumption. Using Semtech's patented LoRa modulation technique, the SX1276 can achieve a sensitivity of over -148dBm. The high sensitivity combined with the integrated +20 dBm power booster is optimally suited for any application that requires range or endurance [7]. LoRa has the capabilities required by LPWAN technology, so LoRa is very suitable to be applied to wireless sensor networks that can integrate real-time environmental conditions such as temperature, humidity, rainfall, wind, pollution, and others. LoRa technology is suitable for use in urban and rural environments [8]. LoRa technology supports variable and adaptive speeds, enabling trade-offs between throughput for long distances with good durability and low energy consumption, while keeping bandwidth constant [9]. One receiver on a LoRa network can handle multiple hubs in an area. Its performance is much better when compared to Wi-Fi networks which require many access points to cover a wide range. Although LoRa performance is better when compared to Wi-Fi, there are inconveniences in transmission speed and size of the payload [10].

II. METHODOLOGY

A. LoRa Modul

LoRa (Long Range) is a spread spectrum modulation technique derived from chip spread spectrum (CSS) technology. LoRa is a long-range low-power wireless platform that has become the Internet of Things (IoT) de facto wireless platform. LoRa works under the unlicensed frequency of 1 GHz, is a unique modulator created by Semtech [11]. LoRa uses a type of frequency modulator (FM) with transmission methods in the form of Phase Shift Keying (PSK), or Frequency Shift Keying (FSK). LoRa uses six spreading factors (SF7 to SF12) to adjust the data rate and tradeoff range. Higher spreading factors allow longer coverage at the expense of lower data rates, and vice versa. LoRa data rates are between 300 bps and 50 kbps depending on spreading factors and bandwidth. Messages transmitted using different spreading factors can be received simultaneously by LoRa BTS. The maximum payload length for each message is 243 bytes [12]. If we refer to the OSI standard, there is a difference between LoRa and LoRaWAN. LoRa represents the physical layer, while LoRaWAN is the MAC layer. LoRaWAN added to standardize and improve LoRa physical communication. LoRaWAN has been designed to respond to use cases where sensors communicate small amounts of data over several times a day. But it is not designed to support applications that require high data rates such as audio or video [13].



Fig. 1. LoRa Module SX1276

TABLE I. DEVICE COMPONENTS OF LORA

Device	Model
LoRa	SX1276
Node MCU	ESP32 W ROOM
Antenna	Omnidirectional 3 dBi
Screen	SSD1306 0.96 inch I2C OLED
Interface	Android Smartphone

LoRa supports the use of multiple carrier frequencies. Carrier frequency in MHz, allowed values range from 137.0 MHz to 1020.0 MHz. We use the 920MHz frequency in accordance with the LoRa frequency usage rules that apply in Indonesia. On both sides of the sender and receiver in order to communicate well, it is necessary to adjust the suitability of the test parameters on both the sending and receiving sides. Table II shows some other parameters used, we use a compromise of several parameters based on [8] to get the best results

TABLE II. PARAMETERS SETTING

Device	Model
Frequency	920MHz
Power Transmission	17 dBm
Coding rate	4/5
Payload size	32 byte
Bandwidth	250 kHz
Spreading Factor	8

B. ESP32

The ESP32 is a dual-core system with two Harvard Xtensa LX6 architecture CPUs. All embedded memory, external memory, and peripherals are located on the data bus and the CPU instruction bus or on both. Each of the two Harvard Architecture Xtensa LX6 CPUs has 4 GB of 32-bit address space. Both Address spaces are symmetrical between two CPUs. With their little use, the address map of both CPUs is symmetric, meaning the same to access the same memory. Several peripherals in the system can access the embedded memory via DMA. Both CPUs are named PRO_CPU and APP_CPU is used for Protocols and Applications. But to achieve a certain goal the two CPUs are interchangeable [14].



Fig. 2. ESP32 WROOM 32

To send and receive LoRa messages with ESP32, we use the RFM96 transceiver module (SX1276). All LoRa modules are transceivers so LoRa can send and receive messages/information. The RFM96 LoRa transceiver module communicates with the ESP32 using the SPI communication protocol, so the default SPI pin on the ESP32 will be used. RFM96 transceiver module has 3 GND pins and only 1 pin is used Mapping Pin SX1276 and ESP32 can be seen in table III.

TABLE III. PIN MAPPING SX1276 AND ESP32

Pin	SX1276 Pins	ESP32 Pins
1	GND	GND
2	3.3V	3.3V
3	DIO 0	GPIO 2
4	Reset	GPIO 14
5	NSS	GPIO 5
6	SCK	GPIO18
7	MOSI	GPIO 23
8	MISO	GPIO 19

The MISO and MOSI pins are important to note because they are the communication path between the two modules. MISO (Master In Slave Out) and MOSI (Master Out Slave In) are data lines for communication between the SX1276 chip (USBAsp) and Slave (Node MCU). MISO is the path used by ESP32 to receive data, while MOSI is the path used by ESP32 to send data to the microcontroller IC. These two lines are the main lines used by SX1276 and the microcontroller in this case ESP32 to communicate. To avoid errors in communication, synchronization is needed. The synchronization is done with using the SCK pathway. Data (MISO and or MOSI) will be considered valid only when SCK is high.

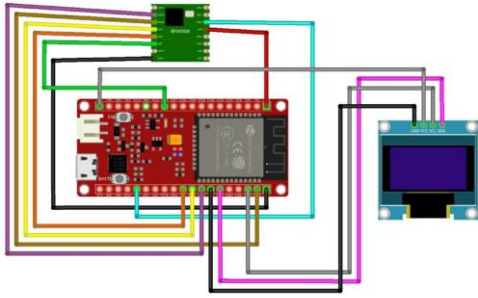


Fig. 3. Circuit diagram SX1276 to ESP32

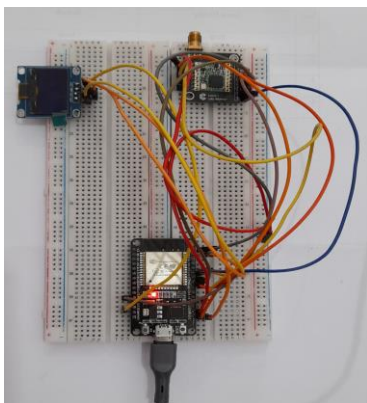


Fig. 4. Connecting SX1276 and ESP32

C. SSD1306 0.96 inch I2C OLED

The organic light-emitting diode or OLED is a light emitting diode (LED) in which the emissive electroluminescent layer is a film of organic compounds that emit light in response to an electric current. OLED screens do not require a backlight and the pixels only consume energy when they are on, so OLED requires less power compared to other screens

D. Communications Model

ESP32 is used as a Wi-Fi access point and as a web server. Smart phone users and ESP32 Web server are connected to the same network provided by EPS32 Wi-Fi. The web server provides an HTML page that serves as a form for typing messages. Messages sent via a web browser are then forwarded to the LoRa SX1276 device. The sending LoRa then forwards the message to the receiving LoRa (Fig. 5).

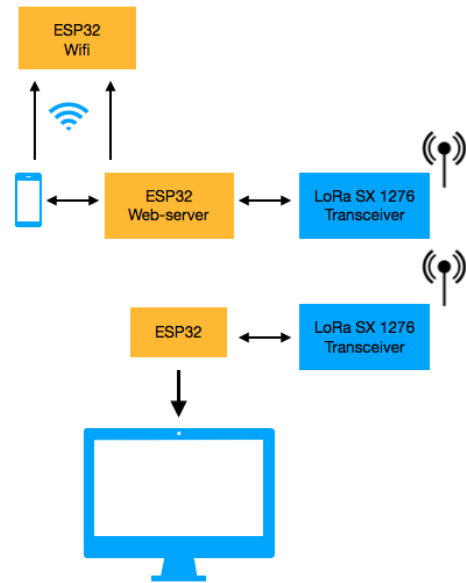


Fig. 5. LoRa Transceiver

E. Blankspot Location

The blankspot location used to test message delivery and the range of LoRa devices is on the route to Mount Rinjani National Park. The route chosen is through Aikmel Village because it crosses the forest area which is a blankspot area. Fig. 6 shows the route along the blank spot area, in addition to the winding path and changing heights, the blank spot path is also blocked by dense tree vegetation.



Fig. 6. Blank spot area

III. RESULTS AND DISCUSSION

In this study, a mechanism was created to send messages in the blankspot area and measure the range achieved by the LoRa SX1276 device. Measurements were made at 10 different points with different ground elevations. The LoRa sender sends a message at a lower ground level to a receiver at a higher ground level and vice versa. The messaging location also has lush trees on both sides of the road.

A. Message Interface

The message sender interface is accessed by the user via a smart phone web browser. The user is connected to the Wi-Fi access point and web server provided by the ESP32 mcu node (Fig. 7). But this LoRa transmitter device is still one-way, meaning that the LoRa transmitter can only send messages and cannot receive messages on the same device.

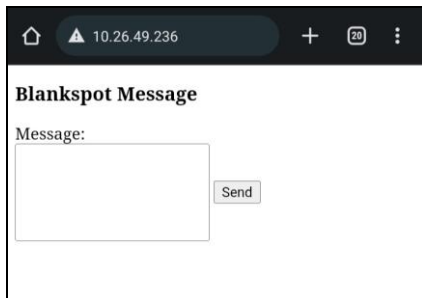


Fig. 7. Message Interface

B. SX1276 Range in Blankspot

Testing of sending messages using LoRa was carried out at 10 points. Table IV shows the distance of sending messages at blankspot locations. The farthest distance obtained is 1.1 km (Fig. 8) and the closest distance is 454 m (Fig. 9).

TABLE IV. LoRa DISTANCE IN BLACKSPOT LOCATIONS

Point	Distance (m)	Starting Point (masl)	end Point (masl)	Packet Lost
1	806	1038	1065	7
2	507	1085	1145	6
3	542	1148	1192	28
4	546	1201	1242	16
5	1.110	1476	1630	6
6	763	1628	1498	17
7	702	1510	1442	27
8	541	1443	1365	27
9	478	1356	1323	21
10	454	1323	1290	10

At points 1 to 5, the sender's LoRa is at a lower altitude than the receiver's LoRa, while points 6 to 10 of the sender's LoRa are at a higher altitude. The height difference between the sender and the receiver can be seen in the table. From the test results, it can be seen that the range achieved by LoRa is further when the receiving device is at a higher ground level.

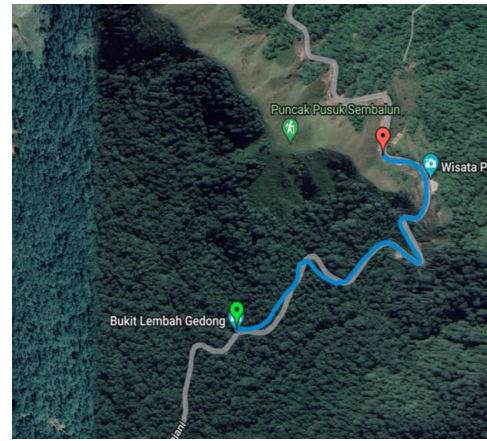


Fig. 8. Blankspot location at a distance of 1.1km



Fig. 9. Blankspot location at the closest distance 454m

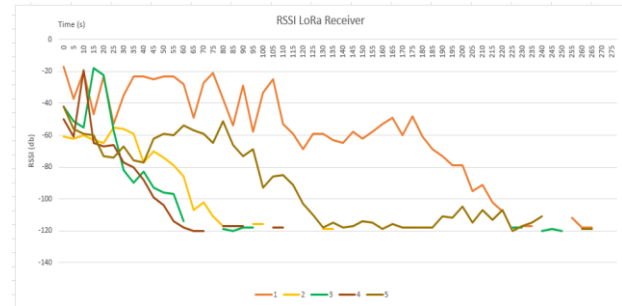


Fig. 10. RSSI LoRa Receiver 1-5

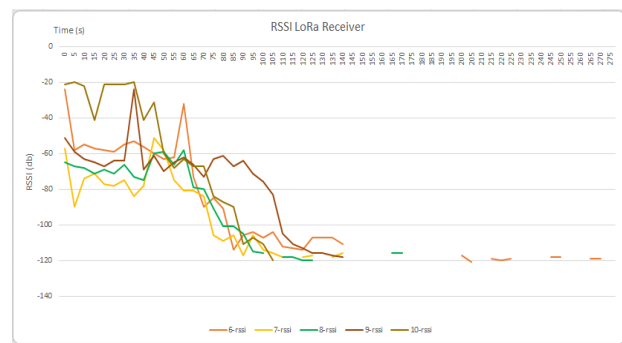


Fig. 11. RSSI LoRa Receiver 6-10

Fig. 10 shows the RSSI value, by observing the RSSI value received by the receiving LoRa device. The pattern of lost data can be analogized to a broken RSSI curve. It can be seen that at point 3 data collection has the most lost data.

In Fig. 11 it can be seen that the RSSI at points 6 to 10 shows a better quality of data reception although in general the range achieved is shorter than the 5 points in Fig. 8.

IV. CONCLUSION

LoRa devices can be used to send messages at blank spot locations by utilizing the ESP32 MCU Node as an intermediary between Android smartphones and LoRa transmitter devices. The LoRa transmitter device is capable of sending messages from a distance of 450 m to 1100 m at the blankspot location although there is still data loss at some measurement points.

ACKNOWLEDGMENT

Thank you to the University of Mataram's leadership for financing this study (contract number 1235/UN18.L1/PP/2022).

REFERENCES

- [1] D. S. George and S. N. Rao, "Enabling Rural Connectivity: Long Range Wi-Fi Versus Super Wi-Fi," 2017 IEEE International Conference on Computational Intelligence and Computing Research (ICCC), 2017, pp. 1-4, doi: 10.1109/ICCC.2017.8524142.
- [2] J. Robert, S. Rauh, H. Lieske and A. Heuberger, "IEEE 802.15 Low Power Wide Area Network (LPWAN) PHY Interference Model," 2018 IEEE International Conference on Communications (ICC), 2018, pp. 1-6, doi: 10.1109/ICC.2018.8422801.
- [3] U. Noreen, A. Bounceur and L. Clavier, "A study of LoRa low power and wide area network technology," 2017 International Conference on Advanced Technologies for Signal and Image Processing (ATSIP), 2017, pp. 1-6, doi: 10.1109/ATSIP.2017.8075570.
- [4] P. Kanakaraja, S.V. Aswin Kumer, B. Jaya Krishna, K. Sri hari, V. Mani Krishna, "Communication through black spot area using LoRa technology and IOT", *Materials Today: Proceedings*. Volume 46, Part 9, 2021, Pages 3882-3887, ISSN 2214-7853.
- [5] Aoudia F, Gautier M, Magno M, et al. (2018) Long-short range communication network leveraging LoRa™ and wake-up receiver. *Microprocessors and Microsystems* 56: 184–192.
- [6] Reddy, Y.A.K., Suganthi, K., Kumar, P.M., Khan, A.A., Pavan, K.S. (2020). LoRa—Pollution and Weather Monitoring System. In: Dash, S., Lakshmi, C., Das, S., Panigrahi, B. (eds) *Artificial Intelligence and Evolutionary Computations in Engineering Systems*. *Advances in Intelligent Systems and Computing*, vol 1056. Springer, Singapore. https://doi.org/10.1007/978-981-15-0199-9_32
- [7] Semtech SX1276/77/78/79 Accessed: July 23, 2022. [Online]. Available: https://semtech.my.salesforce.com/sfc/p/#E0000000JelG/a/2R0000001Rbr/6EfVZUorrpoKFfvaF_Fkpgp5kzjiNyiAbqcpqh9qSjE
- [8] Misbahuddin, L.A.S.I. Akbar, D. F. Budiman and A. Natsir, "Compromise of 915 MHz LoRa Transmission Parameters in A Single-hop Uplink," 2021 International Conference on Computer System, Information Technology, and Electrical Engineering (COSITE), 2021, pp. 63-68, doi: 10.1109/COSITE52651.2021.9649499.
- [9] O. Georgiou, U. Raza, Low power wide area network analysis: Can LoRa scale?, *IEEE Wireless Communications Letters*. 6 (2) (2017) 162–165.
- [10] A. S. Rawat, J. Rajendran, H. Ramiah and A. Rana, "LoRa (Long Range) and LoRaWAN Technology for IoT Applications in COVID-19 Pandemic," 2020 International Conference on Advances in Computing, Communication & Materials (ICACCM), 2020, pp. 419-422, doi: 10.1109/ICACCM50413.2020.9213067.
- [11] Semtech, "LoRa Platform For IoT." 2022 [Online]. Available at: <https://www.semtech.com/lora>.
- [12] B. Mekki, "A comparative study of LPWAN technologies for large-scale IoT deployment," *ICT Express*, vol. 5, no. 1, hlm. 1–7, 2019 [Online]. Available at : <https://doi.org/10.1016/j.ict.2017.12.005>.
- [13] A. Ducrot, Nicolas; Ray, Dominique; Saadani, "LoRa Device Developer Guide," hlm. 42, 2016 [Online]. Tersedia pada: <https://partner.orange.com/wp-content/uploads/2016/04/LoRaDevice-Developer-Guide-Orange.pdf>
- [14] ESP32 Technical Reference Manual. Version 4.6 Espressif Systems. 2021. Accessed: August 3, 2022. [Online]. Available: https://www.espressif.com/sites/default/files/documentation/esp32_technical_reference_manual_en.pdf

D-Vote: Decentralized Voting System Using Ethereum Blockchain

Darrell Yonathan
Department of Electrical Engineering
Faculty of Engineering
Universitas Indonesia
darrell.yonathan@ui.ac.id

Kenya Damayanti
Department of Electrical Engineering
Faculty of Engineering
Universitas Indonesia
kenyadamayantip@gmail.com

Galih Damar Jati
Department of Electrical Engineering
Faculty of Engineering
Universitas Indonesia
galih.damar71@ui.ac.id

Jauzak Hussaini Windiatmaja
Department of Electrical Engineering
Faculty of Engineering
Universitas Indonesia
jauzak.hussaini@ui.ac.id

Geraldly Christanto
Department of Electrical Engineering
Faculty of Engineering
Universitas Indonesia
geraldly.christanto@ui.ac.id

Riri Fitri Sari
Department of Electrical Engineering
Faculty of Engineering
Universitas Indonesia
riri@ui.ac.id

Abstract— Voting is a means of making collective decisions in communities, organizations, and institutions. Each participant is granted a number of votes that they can use to affect the election outcomes of the current candidates. The votes are tallied at the end of the voting process, and the outcome is determined by the electoral system in use. Conventionally, we may associate this voting mechanism with a piece of paper that is filled out and then placed in a box. However, postal ballots, postal voting, internet voting, and manual voting are all means of voting. The presence of incidents in which data from voting results are manipulated or are not counted from the indicated voting system calls the data's integrity into doubt. We think that utilizing blockchain technology for voting systems will overcome this problem. Blockchain will help secure voting result data and the voting process. A web-based application named D-Vote was developed to implement blockchain technology on voting systems. With blockchain characteristics, D-Vote can maintain the security of collected voting data as well as data containing the identities of voters who are entitled to vote. Furthermore, test result shows that all functions was successfully performed by entering several parameters as needed.

Keywords—blockchain, decentralized, web-based application, security, voting

I. INTRODUCTION

Voting is a method of collective decision-making between communities, organizations and institutions. Voting is a widely used activity among the communities. Each participant is given a certain number of votes that they can cast to influence the election results of the existing candidates. At the end of the vote, then simultaneously the vote is counted and the result of the vote is determined according to the applicable electoral system. At first we may know this voting system through a paper that is filled and then collected into a place. However, voting can be done by several methods such as postal ballots, postal voting, online voting and machine voting (offline).

The existence of cases or events that data from the voting results are rigged or there is data that does not enter the conventional voting system or that is already online makes the integrity of the data questionable. This can be solved by the existence of a blockchain system. Blockchain will help secure voting result data and even secure the voting process. Blockchain has a decentralized mechanism so that every user in the voting can see the transaction data in its entirety. The verification process in this blockchain system also plays an important role to ensure that the people who votes are the

ones who are indeed registered. This process will make the voting process much safer.

D-Vote is a web-based application designed to implement blockchain technology on campus voting systems. With the features of the blockchain, the application can easily authenticate the identity of the voter to prevent fraud in the vote and can prevent unregistered voters from voting. In addition, with blockchain technology, D-Vote can maintain the security of collected voting data as well as data containing the identities of voters who are entitled to vote.

The purpose of this research is to implement blockchain technology in voting systems using Ethereum. By using blockchain technology, the pre-recorded election results are secured, it cannot be changed or deleted. Decentralized systems in blockchain enhance user privacy as no third party can manipulate the data. In addition, voter identity is also more secure because it is pseudonymous, where users in the Ethereum network use private keys, so that others cannot know who is voting.

II. LITERATURE REVIEW

A. Ethereum Blockchain

As blockchain technology evolves, developers want to use the concept of blockchain into a wider range of applications not just as payment applications [1]. The protocol used in bitcoin is not able to accommodate these requirements, regardless of the advantages it has. So Vitalik Buterin developed Ethereum in 2013, as a platform that can create decentralized applications using blockchain through smart contract support [2].

Ethereum is an alternative open source platform for running decentralized applications by providing a very useful approach to various cases with fast development times and more efficient interactions [3]. In his paper, Buterin states that Ethereum allows developers to create blockchain-based applications, with features such as scalability, standardization, feature completeness, as well as ease of development and interoperability [4].

The networks in Ethereum can be distinguished into two types, namely public networks and private networks. Public networks can be accessed by anyone connected to the internet. On this network, anyone can view or make transactions on the blockchain network and validate the

executed transactions [5]. Transaction approval is determined through the network node consensus mechanism. There are two kinds of public networks on Ethereum, namely the mainnet network which is the main network that has the actual coin value on the transactions made and the testnet network used for development before smart contracts are deployed to the production environment or to the mainnet [6].

A transaction is an instruction digitally signed by Externally-owned Account (EOA). EOA will initiate a transaction to update the status in the Ethereum network. With the decentralized nature of blockchain, new transactions must be distributed broadcast to the entire network [7]. Transactions require costs and must be validated through consensus protocols. Transaction fees in Ethereum using gas units.

B. Solidity

Solidity is a high-level programming language better known as contract-based. The syntax of this programming language is similar to that of the Javascript programming language. This programming language is used to improve the performance of virtual machines on Ethereum [8]. This solidity is a statically crafted scripting language for the verification process and limitations on compile time. In addition to compiling, this programming language will also help check at run-time. This solidity programming language also supports object-oriented programming such as object inheritance and others [9]. Solidity workflow is shown in Fig. 1.

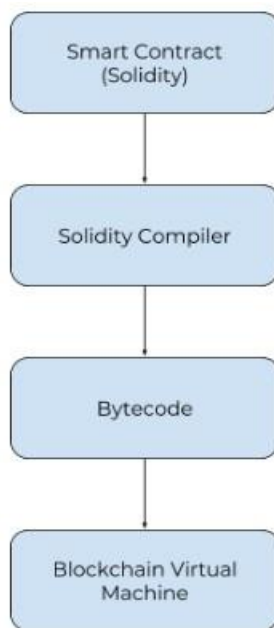


Fig. 1. Solidity Workflow

Solidity is a programming language created specifically for Smart Contracts on Ethereum [16]. Solidity is written in the .sol file format. Solidity is basically not an executable language on the Blockchain Virtual Machine [10]. Solidity is a language that aims to make it easier for developers to create smart contracts. When we are going to compile or deploy our smart contract, we need a solidity compiler [11]. Through the solidity compiler smart contract we will be

compiled into bytecode which will be the bytecode that will be executed by the virtual machine.

C. Third Party Resources

Metamask is a cryptocurrency wallet that can be used in Chrome, Firefox and Brave browsers. This wallet application is a browser extension that works like a bridge between a normal browser and the Ethereum blockchain so that this application can also be referred to as a 3rd party application. Metamask can be used to store keys only for Ethereum cryptocurrencies [12]. There is an Ethereum cryptocurrency commonly called Ether. In addition there are also other cryptocurrencies built on the Ethereum blockchain that are tokens. Most of the tokens built on the Ethereum blockchain are called ERC20 tokens because they follow the rules that Ethereum developers have set to create new cryptocurrencies [13].

Metamask has several network options such as Rinkeby, Ropsten and other networks. This network serves to store transaction data from users. Metamask can interact automatically with Ethereum-based websites [14]. This metamask is quite safe because there hasn't been a major hack. Metamask browser extensions interface is shown in Fig. 2.

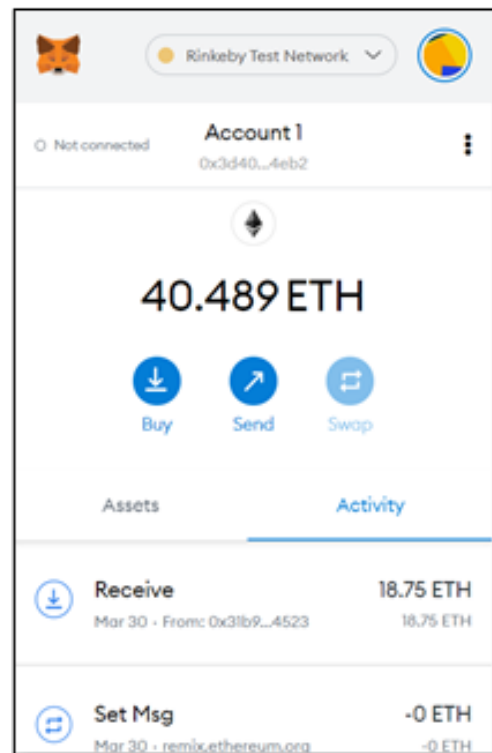


Fig. 2. Metamask Extension

Metamask is suitable for use as a network in application development commonly called Decentralize Application (DApp) [15]. Automation can also be done from DApp applications to Metamask to run and verify to blockchain networks [16]. Since this metamask is a wallet, users can also receive and send cryptocurrencies to other users. In metamask, users can also create more than one wallet account.

III. PROPOSED WORK AND IMPLEMENTATION

This section describes the proposed architecture and the implementation of D-Vote application. D-Vote is created based on Ethereum network architecture. D-Vote is connected using the Web3.js library. The smart contracts that we created are deployed into the Ethereum network through Ganache. We also use several accounts available in Ganache so that voters do not have to pay gas fee when voting.

A. Directory

Programs are created using JavaScript with nodes.js framework. There are also several dependencies that need to be installed in this program. Front-end and back-end applications are stored in the app folder, while contracts are stored in the contracts folder. Contract migration scripts to other networks and initialization is done in the migrations folder.

B. Contract (Solidity)

There are three main contracts in our application, i.e. voting.sol, registrar.sol, and creator.sol. The diagram of each contract produces a different struct. The code snippet of the contracts are described as follow:

1) Voting.sol

In this contract there are three data struct, i.e. Ballot as voting made, Candidates as data for the list of candidates on the ballot created, and Voters created using whitelist data or not. Voting.sol is shown in Fig. 3.

```
pragma solidity ^0.4.19;

contract Voting {

    struct Ballot {
        uint8 ballotType;
        uint32 ballotId;
        uint8 voteLimit;
        uint32 timeLimit;
        string title;
        uint8 whitelist;
    }

    struct Candidates {
        bytes32[] candidatelist;
        mapping (bytes32 => bytes32) candidateHash;
        mapping (bytes32 => uint256) votesReceived;
    }

    struct Voter {
        bytes32[] whitelisted;
        mapping (address => uint8) attemptedVotes;
    }
}
```

Fig. 3. Voting.sol Snippet

To add the contents of the data to the struct, there are several functions that can be used. Function setCandidates is created for adding candidate data in ballots. Function hashCandidates is created for

changing candidate names into Keccak256 format when saved into blockchain network. Function voteForCandidate is created to add the number of votes from voter to selected candidate, as well as some other additional functions such as to view candidate list or other data structure [16]. Candidate List and Voter Whitelist is shown in Fig. 4.

```
function setCandidates(bytes32[] _candidates) public onlyOwner {
    for(uint i = 0; i < _candidates.length; i++) {
        tempCandidate = _candidates[i];
        c.candidateList.push(tempCandidate);
    }
}

function setWhitelisted(bytes32[] _emails) public onlyOwner {
    for(uint i = 0; i < _emails.length; i++) {
        tempEmail = _emails[i];
        v.whitelisted.push(tempEmail);
    }
}

function hashCandidates() public onlyOwner {
    tempVote = 1;
    for(uint i = 0; i < c.candidateList.length; i++) {
        tempCandidate = c.candidateList[i];
        convertCandidate = bytes32tostring(tempCandidate);
        c.candidateHash[tempCandidate] = keccak256(abi.encodePacked(convertCandidate));
        c.votesReceived[keccak256(abi.encodePacked(convertCandidate))] = tempVote;
    }
}

function voteForCandidate(uint256[] _votes, bytes32 _email, bytes32[] _candidates) public {
    if (checkTimeLimit() == false || checkVoteAttempts() == false) revert();
    if (checkWhitelisted() == true && checkIfWhitelisted(_email) == false) revert();
    tempVotes = _votes;
    tempCandidates = _candidates;
    v.attemptedVotes[msg.sender] += 1;

    for(uint i = 0; i < tempCandidates.length; i++) {
        tempCandidate = tempCandidates[i];
        tempHash = c.candidateHash[tempCandidate];
        if (validCandidate(tempHash) == false) revert();
        tempVote = tempVotes[i];
        c.votesReceived[tempHash] = tempVote;
    }
}

function votesFor(bytes32 cHash) public returns (uint256){
    if (validCandidate(cHash) == false) revert();
    return c.votesReceived[cHash];
}
```

Fig. 4. Candidate List Snippets and Voter Whitelist

2) Creator.sol

Contract creator.sol is only used to create new ballots with some parameters such as, voting expiration time, ballot name, and whitelisted voter data if needed. Creator.sol snippet is shown in Fig. 5.

```
contract Creator {
    mapping (uint32 => address) contracts;
    address owner;

    function createBallot(uint32 _timeLimit, uint8 _ballotType, uint8 _voteLimit, uint32 _ballotId, string _title, uint8 _whitelisted) public {
        owner = msg.sender;
        address newContract = new Voting(_timeLimit, _ballotType, _voteLimit, _ballotId, _title, _whitelisted, owner);
        contracts[_ballotId] = newContract;
    }

    function getAddress(uint32 id) public view returns (address contractAddress) {
        return contracts[id];
    }
}
```

Fig. 5. Creator.sol Snippet

3) Registrar.sol

The function of the contract registrar is to register voters or voters using the appropriate email, as well as view the registration or registration of election participants. Registrar.sol is shown in Fig. 6.

```

1 pragma solidity ^0.4.19;
2
3 contract Registrar {
4
5     struct voter {
6         bytes32[] allowedDomains;
7         mapping (bytes32 => address) voterAddr;
8         mapping (bytes32 => uint256) createPerms;
9         mapping (bytes32 => uint256) voterID;
10        mapping (uint256 => bytes32) voterEmail;
11    }
12
13    struct ballot {
14        mapping (uint256 => address) votingAddress;
15        mapping (address => uint256) ballotID;
16        mapping (uint256 => uint256) whitelistCheck;
17        mapping (bytes32 => uint256) allowedVoters;
18    }
19
20    voter v;
21    ballot b;
22    address owner;
23
24    constructor (bytes32[] domainList) public {
25        v.allowedDomains = domainList;
26        owner = msg.sender;
27    }
28
29    modifier onlyOwner {
30        require(msg.sender == owner);
31        _;
32    }
33
34    function registerVoter(bytes32 email, uint256 idnum, bytes32 _domain, uint256 _permreq) public {
35        if (domainCheck(_domain) == false) revert();
36        v.voterID[email] = idnum;
37        v.createPerms[email] = _permreq;
38        v.voterAddr[email] = msg.sender;
39        v.voterEmail[idnum] = email;
40    }

```

Fig. 6. Registrar.sol Snippet

The function of the contract registrar is to register voters or voters using the appropriate email, as well as view the registration or registration of election participants.

4) Web3 Initialization

Initialization of web3 instances in the app.js to be used in contract calling functions. Web3 is used to connect Ethereum wallets connected to the blockchain network. Contracts that have been compiled will be able to interact as objects in the created JavaScript. By using ganache, RPC Server is created in local network with port number 7545. Web3 initialization is shown in Fig. 7.

```

$(document).ready(function() {
    var web3 = new Web3(new Web3.providers.HttpProvider("http://localhost:7545"));
    Registrar.setProvider(web3.currentProvider)
    Voting.setProvider(web3.currentProvider)
    Creator.setProvider(web3.currentProvider)
})

```

Fig. 7. Web3 Initialization

5) Truffle Configuration

This file contains network and solc compiler configuration. Local network is used using Ganache so that transaction interactions conducted by users do not have to pay the required network fees. The solidity compiler version used in this research is 0.4.26. This compiler is adapted to the solidity version of the smart contract. The truffle configuration is shown in Fig. 8.

```

4 module.exports = {
5     networks: {
6         development: {
7             host: 'localhost',
8             port: 7545,
9             network_id: '*'
10        },
11    },
12    compilers: {
13        solc: {
14            version: "^0.4.26"
15        }
16    }
17 }

```

Fig. 8. Truffle Configuration

IV. RESULT AND ANALYSIS

This section described the result and analysis of the research. After the contract migration has been successfully performed from local network to Ganache network, we analyze application behavior and gas fee to make sure it is ready for production deployment. The analysis on Ganache Network is based on previous works [18]-[21].

TABLE I. CONTRACT ADDRESS

Contract	Contract Address
Voting.sol	0xD8ACBcf0D96824a411A52c2B2bb75d db33151DD9
Registrar.sol	0x48B52D9213d35BCF0Baa6A0a7C1b4 A4dec1942b0
Creator.sol	0x6069e29859Eb6F419fE4Ef0391028b8f 6Cf371E9

Tabel 1 described contract address of each contract deployed on the network. We test the application using defender.openzeppelin.com. Openzeppelin is used to speed up the testing process with an easier interface. Test result shows that all functions were successfully performed by entering several parameters as needed.

A. Voter Registration

Voter registration is done by entering an ID, i.e. student number, and also email address in form. Users can also select the option for request a permission so that the email can be used for admins in ballot creation. The voter registration interface is shown in Fig. 9.

Fig. 9. Voter Registration

B. Ballot Creation

Ballot creation is done by filling out the following form. There are some information that needs to be provided in making the ballot. Users need to enter an email that has admin permissions. The type of ballot that can be created is poll. The poll will show the number of votes each ballot is reloaded. Users also need to add ballot titles, candidate names separated using commas, and limits on the number of votes allowed for each voter.

Fig. 10. Ballot Creation Form

To vote, there are two options, i.e. non-whitelist and whitelist. The non-whitelist option allows all emails with whitelisted domains. For testing purposes, the whitelisted domain is @ui.ac.id as the project is intended for campus-level voting. The whitelist option only allows some emails to be populated in the next field. As in the candidate filling section, the filling of email addresses is separated by commas. Furthermore, the duration of voting is determined by entering the closing date and time of the voting period. After the ballot is successfully created, transaction information will appear containing address, ETH value, gas, and tx data. In addition, there are information about the type of contract created along with the function called and the parameters and inputs entered.

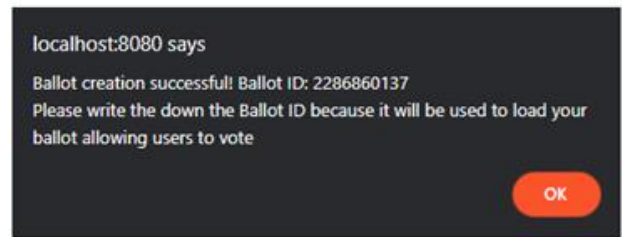


Fig. 11. Notification After Create Ballot Successful

C. Load Ballot and Voting

To vote, a ballot needs to be loaded first by entering its ID. After a ballot is successfully loaded, a table will appear containing the names of candidates along with the number of votes for each candidate.

Candidate	Votes
Djati	0
Yonathan	0

Fig. 12. Load Ballot Process

To vote, the user needs to enter the email registered as the voter and also the name of the candidate you want to vote for.

Fig. 13. Voting Page

A vote will be accepted if it has gone through the verification process. When verification is successful, a pop up like the one above appears. When the vote verification is successful, the number of votes on the selected candidate will increase if the ballot is loaded again.



Fig. 14. Verified Vote

D. Gas Fee Analysis

The gas fee analysis is conducted to find out the average cost required for each transaction.

1) Contract Deployment

We can see from Table II that the total cost required to deploy the three contracts is 0.06409316 ETH. The most widely used cost is when deploying the contract creator because the contract is inheritance of voting contracts to be used at the time of creating a new ballot. For contracts that use the least cost is the contract registrar because on the contract the least computing.

TABLE II. ADDRESS CONTRACT

Contract	Gas Price (gwei)	Gas Used (unit)	Total Cost (ETH)
Voting	20	1173893	0.02347786
Registrar	20	599020	0.0119804
Creator	20	1431745	0.0286349

The most used cost is when deploying the contract creator. We believe that this might happened because the contract is inheritance of voting contracts to be used at the time of creating a new ballot. For contracts that use the least cost is the contract registrar because on the contract the least computing.

2) Transaction

Gas fee measurement in each transaction is done as many as 3 experiments to find the average cost required for each transaction:

TABLE III. TRANSACTION FEE FOR REGISTER NEW VOTER

n	Gas Used (unit)	Gas Price (gwei)	Tx Fee (ETH)
1	108246	20	0.00216492
2	108162	20	0.00216324
3	108066	20	0.00216132

We can see from Table III that the average transaction fee required to register a voter is 0.00216316 ETH.

TABLE IV. TRANSACTION FEE FOR FOR BALLOT MAKING

n	function	Gas Used (unit)	Gas Price (gwei)	Tx Fee (ETH)
1	checkVoter	1117325	20	0.00223465
	getPermission	63898	20	0.00127796
	createBallot	108554	20	0.00217108
	getAddress	181613	20	0.00363226
2	checkVoter	1117313	20	0.00223463
	getPermission	63886	20	0.00127772
	createBallot	132195	20	0.00026439
	getAddress	241666	20	0.00048333
3	checkVoter	1117325	20	0.00223465
	getPermission	63898	20	0.00012780
	createBallot	155836	20	0.00031167
	getAddress	301719	20	0.00060344

We can see from Table IV that the average transaction cost required for one ballot or voting is 0.005234542 ETH.

3) Vote

We can see from Table V that the average transaction fee made at the time of voting is 0.00635756 ETH. Over three transactions made in this voting system, the most costly transactions are voting. We believe it might happened because there are several functions needed in a voting contract. It also has a number of computational functions, such as hashing and encryption functions. The second transaction is at the time of ballot making where there are quite a lot of functions of various contracts called with varying gas costs. The last transaction that has the lowest transaction fee is voter registration, because of the little transaction data and few function calls made [17].

TABLE V. TRANSACTION FEE FOR VOTE

n	Gas Used (unit)	Gas Price (gwei)	Tx Fee (ETH)
1	316248	20	0.00632496
2	243903	20	0.00487806
3	393544	20	0.00787066

V. CONCLUSION AND FUTURE WORK

A blockchain-based e-voting application used to conduct candidate voting is successfully made. Blockchain technology is used to maintain data security and integrity as well as to ensure voter identity to avoid fraud in the voting process. The immutable nature of the blockchain will also make the data of the voting process cannot be changed and always relate to each transaction. We aware that these applications still have some drawbacks, especially on the application interface that are less attractive to use. Further development and research of the user interface and user experience are needed. Authentication also needs to be added to the administrator when registering a voter and creating a new vote.

ACKNOWLEDGMENT

This work is supported by the Ministry of Education, Culture, Research, and Technology (Kemendikbudristek) of Indonesia under PDD Grant with contract number NKB-1016/UN2.RST/HKP.05.00/2022.

REFERENCES

- [1] Y. Huang, B. Wang and Y. Wang, "MRResearch on Ethereum Private Blockchain Multi-nodes Platform," 2020 International Conference on Big Data, Artificial Intelligence and Internet of Things Engineering (ICBAIE), 2020, pp. 369-372, doi: 10.1109/ICBAIE49996.2020.00083.
- [2] S. Rouhani and R. Deters, "Performance analysis of ethereum transactions in private blockchain," 2017 8th IEEE International Conference on Software Engineering and Service Science (ICSESS), 2017, pp. 70-74, doi: 10.1109/ICSESS.2017.8342866.
- [3] X. Liu, R. Chen, Y. Chen and S. Yuan, "Off-chain Data Fetching Architecture for Ethereum Smart Contract," 2018 International Conference on Cloud Computing, Big Data and Blockchain (ICCCBB), 2018, pp. 1-4, doi: 10.1109/ICCCBB.2018.8756348.
- [4] G. A. Pierro and H. Rocha, "The Influence Factors on Ethereum Transaction Fees," 2019 IEEE/ACM 2nd International Workshop on Emerging Trends in Software Engineering for Blockchain (WETSEB), 2019, pp. 24-31, doi: 10.1109/WETSEB.2019.00010.
- [5] C. BouSaba and E. Anderson, "Degree Validation Application Using Solidity and Ethereum Blockchain," 2019 SoutheastCon, 2019, pp. 15, doi: 10.1109/SoutheastCon42311.2019.9020503.
- [6] S. H. Maeng, M. Essaid and H. T. Ju, "Analysis of Ethereum Network Properties and Behavior of Influential Nodes," 2020 21st Asia-Pacific Network Operations and Management Symposium (APNOMS), 2020, pp. 203-207, doi: 10.23919/APNOMS50412.2020.9236965.
- [7] R. A. Canessane, N. Srinivasan, A. Beuria, A. Singh and B. M. Kumar, "Decentralised Applications Using Ethereum Blockchain," 2019 Fifth International Conference on Science Technology Engineering and Mathematics (ICONSTEM), 2019, pp. 75-79, doi: 10.1109/ICONSTEM.2019.8918887.
- [8] Y. N. Aung and T. Tantidham, "Review of Ethereum: Smart home case study," 2017 2nd International Conference on Information Technology (INCIT), 2017, pp. 1-4, doi: 10.1109/INCIT.2017.8257877.
- [9] P. V. Sukharev and D. S. Silnov, "Asynchronous Mining of Ethereum Cryptocurrency," 2018 IEEE International Conference "Quality Management, Transport and Information Security, Information Technologies" (IT&QM&IS), 2018, pp. 731-735, doi:10.1109/ITMQIS.2018.8524929.
- [10] W. Chan and A. Olmsted, "Ethereum transaction graph analysis," 2017 12th International Conference for Internet Technology and Secured Transactions (ICITST), 2017, pp. 498-500, doi: 10.23919/ICITST.2017.8356459.
- [11] P. Deshmukh, S. Kalwaghe, A. Appa and A. Pawar, "Decentralised Freelancing using Ethereum Blockchain," 2020 International Conference on Communication and Signal Processing (ICCSPP), 2020, pp. 881-883, doi: 10.1109/ICCSPP48568.2020.9182127.
- [12] Aldweesh, M. Alharby and A. van Moorsel, "Performance Benchmarking for Ethereum Opcodes," 2018 IEEE/ACS 15th International Conference on Computer Systems and Applications (AICCSA), 2018, pp. 1-2, doi: 10.1109/AICCSA.2018.8612882.
- [13] V. Aleksieva, H. Valchanov and A. Huliyan, "Application of Smart Contracts based on Ethereum Blockchain for the Purpose of Insurance Services," 2019 International Conference on Biomedical Innovations and Applications (BIA), 2019, pp. 1-4, doi: 10.1109/BIA48344.2019.8967468
- [14] J. Chen, "Finding Ethereum Smart Contracts Security Issues by Comparing History Versions," 2020 35th IEEE/ACM International Conference on Automated Software Engineering (ASE), 2020, pp. 1382-1384..
- [15] P. V. Sukharev and D. S. Silnov, "Mining Result Validation in the Ethereum Cryptocurrency," 2019 IEEE Conference of Russian Young Researchers in Electrical and Electronic Engineering (EConRus), 2019, pp. 1731-1734, doi: 10.1109/EConRus.2019.8656906.
- [16] T. Wang, C. Zhao, Q. Yang, S. Zhang and S. C. Liew, "Ethna: Analyzing the Underlying Peer-to-Peer Network of Ethereum Blockchain," in IEEE Transactions on Network Science and Engineering, doi: 10.1109/TNSE.2021.3078181.
- [17] U. Bagadia, J. Bodkurwar, J. Bhat and A. Halbe, "Performance Analysis of Decentralized Ethereum Blockchain System," 2020 International Conference on Inventive Computation Technologies (ICICT), 2020, pp. 127-131, doi: 10.1109/ICICT48043.2020.9112550.
- [18] P. Hegedus, "Towards Analyzing the Complexity Landscape of Solidity Based Ethereum Smart Contracts," 2018 IEEE/ACM 1st International Workshop on Emerging Trends in Software Engineering for Blockchain (WETSEB), 2018, pp. 35-39.
- [19] S. Kim, J. Song, S. Woo, Y. Kim and S. Park, "Gas Consumption Aware Dynamic Load Balancing in Ethereum Sharding Environments," 2019 IEEE 4th International Workshops on Foundations and Applications of Self* Systems (FAS*W), 2019, pp. 188-193, doi: 10.1109/FAS-W.2019.00052.
- [20] D. Son, S. Al Zahr and G. Memmi, "Performance Analysis of an Energy Trading Platform Using the Ethereum Blockchain," 2021 IEEE International Conference on Blockchain and Cryptocurrency (ICBC), 2021, pp. 1-3, doi: 10.1109/ICBC51069.2021.9461115.
- [21] Aldweesh, "Analysis, Evaluation and Benchmark The Ethereum Incentive Mechanism," 2021 IEEE 11th International Conference on Electronics Information and Emergency Communication (ICEIEC)2021 IEEE 11th International Conference on Electronics Information and Emergency Communication (ICEIEC), 2021, pp. 14, doi: 10.1109/ICEIEC51955.2021.9463723.

Clippo: a Speaker Clip on Mask

Erwin Sanjaya Loeminto
Electrical Engineering Department
Petra Christian University
Surabaya, Indonesia
erwin.loeminto@gmail.com

Felix Pasila
Electrical Engineering Department,
Petra Christian University
Surabaya, Indonesia
felix@petra.ac.id

Abstract— This paper includes an Introduction, basic laws and regulations, and technical explanations of loudspeakers on masks that could be used to make it easier for mask users to speak which is a solution to the problem of difficulty communicating in conditions of corona virus disease 2019 (COVID-19) which requires a person to wear a mask. Talking about solutions, the author takes the perspective of opportunities to help others, and makes it easier for medical personnel, the public and close relatives to communicate using masks without any disturbance in terms of how big or small the voice is. From this article, the author finds a solution to this problem, namely a loudspeaker that can be easily attached to any mask called CLIPPO with patent pending number S00202104532. The implication of further research is connecting the Clippo into Bluetooth Device for communication with gadget or other peripheral device.

Keywords—CLIPPO, loudspeaker, speaker, speaker clip on mask, covid19.

I. INTRODUCTION

WHO (World Health Organization or World Health Organization) officially declared the corona virus (COVID-19) as a pandemic on March 9, 2020. So everyone is required to wear a mask. In 2020, Indonesia, one of the countries affected by Corona Virus Disease (COVID-19) underwent a major overhaul of the legal system which required people to wear mask as a new part of normal life since the world declared Covid-19 virus as pandemic.

One of the basic elements in this problem is masks ranging from medical mask to fabric mask has been circulating in the market. Apart from the shortage of masks, other problems arise when communicating. When people wear their masks, they tend to lower or even take off their masks due to the difficulty of speaking and even listeners find it difficult to catch on what other people were saying. Even without lowering or removing the mask, it takes more energy to speak louder so that the other people could hear.

Based on this fact, the author creates a loudspeaker on the mask with the clip method. This is useful for making it easier for mask wearer to speak without requiring excessive energy and removing the mask.

II. LITERATURE REVIEW

The theory of sound was first discovered by James Maxwell who had a mathematical theory of energy. The theory was about energy that could be channeled through the air and was visible to the eye. However, this theory could not be proven until in 1887 Heinrich Hertz proved James Maxwell's theory through an experiment with two metal rods that were electrified and a strong receiver made of copper.

A loudspeaker is a transducer that converts an electrical signal to an audio frequency (sound) by vibrating its membrane-shaped components to vibrate the air so that

sound waves reach our eardrums and we can hear them as sound.

On the basis of these theories and books, CLIPPO was born to present sound transmitted by copper or other metals with the clip method.

III. DISCUSSION

A. The Obligation to Wear a Mask in Regulations

The World Health Organization (WHO) has declared a new corona virus named Corona Virus Disease 2019 (COVID-19) as a pandemic on March 9th 2020 and because of the urgency of the pandemic, Indonesia as a country participates in guarding borders, put it in a statutory regulation to provide coercive power for people who aim to fight against the COVID-19 infectious disease. The existence of this urgency COVID-19 was first given instructions by President Joko Widodo in Presidential Instruction No. 6 of 2020 concerning Improvement of Discipline and Law Enforcement of Health Protocols in the Prevention and Control of Corona Virus Disease 2019. In essence, the instruction mentions 4 points, namely the author quotes as follows:

"FIRST

Take the necessary steps according to their respective duties, functions and authorities in ensuring legal certainty, strengthening efforts and increasing the effectiveness of prevention and control of Corona Virus Disease 2019 (COVID-19) in all provinces and districts/cities in Indonesia.

SECOND

...

1) Obligations to comply with health protocols include:

a) Individual health protection which includes:

(1) Use personal protective equipment in the form of a mask covering the nose and mouth to the chin, if you have to leave the house or interact with other people whose health status is unknown.

...”

After the issuance of presidential instruction No. 6 of 2020, various legal instruments emerged, in this case the laws and regulations related to COVID-19, including:

1. Circular Letter Number HK.02.02/I/385/2020 concerning the Use of Masks and Provision of Handwashing Facilities with Soap (CTPS) to Prevent the Transmission of Corona Virus Disease 2019 (COVID-19);

2. Decree of the Minister of Health Number HK.01.07/MENKES/104/2020 of 2020 concerning the Determination of Novel Coronavirus Infection (2019-NCOV INFECTION) as a Disease That Can Cause Outbreaks and Efforts to Overcome it;
3. Instruction of the Minister of Home Affairs Number 13 of 2022 concerning the Implementation of Restrictions on Community Activities at Level 4, Level 3, and Level 2 Corona Virus Disease 2019 in the Java and Bali Regions;
4. Instruction of the Minister of Home Affairs Number 14 of 2022 concerning the Enforcement of Restrictions on Community Activities at Level 3, Level 2, and Level 1 and Optimizing the Command Post for Handling Corona Virus Disease 2019 at the Village and Sub-District Levels to Control the Spread of Corona Virus Disease 2019 in the Sumatra, Nusa Tenggara Region, Kalimantan, Sulawesi, Maluku, and Papua;
5. Letter of the Director General of Supervision of Labor and Occupational Safety and Health No. 5/193/AS.02.02/III/2020 of 2020 concerning Preparedness in Facing the Spread of Covid-19 in the Workplace.

As well as Regional Regulations related to COVID-19 in the areas of West Java, Bali, Banten, DKI Jakarta, South Sulawesi, and North Sumatra.

In addition, the available data also shows that exposure to air pollution can affect the transmission of COVID-19. Furthermore, air pollution can cause adverse effects on the prognosis of patients exposed to SARS-CoV-2 infection [1].

B. Problems Arising From The Use of Mask

Cause-and-effect theory proven in COVID-19 pandemic, which can be seen from the cause of the obligation to use masks according to the recommendations and laws and regulations arising from the use of masks. The consistent message conveyed by health stakeholders is that the fight against the pandemic requires significant behavior change [2].

Problems that arise as a result of using masks include the following:

- Medical masks are becoming scarce

Reporting from CNBC Indonesia, the scarcity of masks due to masks circulating in Indonesia are mostly imported masks. The availability of masks that are running low is certainly difficult for the community. Especially with the price spike [3].

- Skindemic

The use of masks for a long time makes the facial skin continue to rub against the mask. This friction triggers skin irritation, so that the facial skin will become inflamed and acne will appear more easily. In addition, breathing and talking while using a mask will also trap heat which makes facial skin becoming too moist. This condition not only causes clogged pores, but also makes it easier for bacteria and germs to multiply. The combination of irritation, soggy skin, and the number of bacteria on the facial skin are causes of various skin-

demetic problems, ranging from blackheads, rosacea, folliculitis to acne [4].

- Decreased sound level

The author encountered this problem when the author bought food at traditional market which was close to the author's house, in which case when the author wear a mask that makes the grocery store had difficulty in communicating and seemed to have reduced the author's volume so often that the words spoken by the author sound wrong by the seller. This problem also arises when the author conducted socialization with colleagues, and relatives who both wore masks.

As the theory of sound exists, there is a large frequency range over which longitudinal mechanical waves can be generated and sound waves are limited by the range of frequencies that can excite the human ear and brain to the sensation of hearing [5].

When the mask is on, the conversation can't be heard clearly. There are several patents that have made inventions as in the US patent with no. US20200315266 A1 dated October 8th, 2020 with inventor Kathleen Worthington McMahon entitled microphone mask. The patent mentions a device to help clarify pronunciation when someone is wearing a mask. But the weakness of this tool is that it uses a cable that is long enough so that it will interfere with the movement of the user.

On the US patent No. US6940984 B2 dated September 6th, 2005 with the inventor Robert Leonard Carpenter entitled Hands-free megaphone. The patent states that the device for amplifying pronunciation is hands-free. However, this tool can't be used for mask users, and the speaker at the waist makes the use of a long cable so that the function is not for mask users who need loudspeakers every day.

Another invention, namely the US patent No. US20020166557 A1 dated November 14th, 2002 with inventor David Cooper entitled Mask with a built-in microphone. The patent mentions a device to help clarify the pronunciation of someone wearing a mask. But the weakness of this tool is that it uses the transmitter first, and it received by the receiver so that it will require a complex and inflexible tool.

IV. THE DISCOVERY OF CLIPPO AS A VOICE LOUDER WITH A CLIPPER AS A SOLUTION FOR SOUND REDUCTION

The CLIPPO invention process itself has a brief history of the author wanting to modify the speaker and several existing patents. Basically, the sound-conducting medium can have various properties and shapes. It can be solid, liquid, and gas, depending on the extent to which the properties of the material can deliver sound through the air [6]. In general there are two characteristics of sound that can be felt by humans, namely loud and weak sound and high and low sound. Loudness of sound is related to amplitude and energy of the sound wave [7]. In connection with this, the author wants to make an invention based on the problem of reduced sound as a result of the use of masks.

Here is a schematic drawing of a brief history of the loudspeaker clamp.

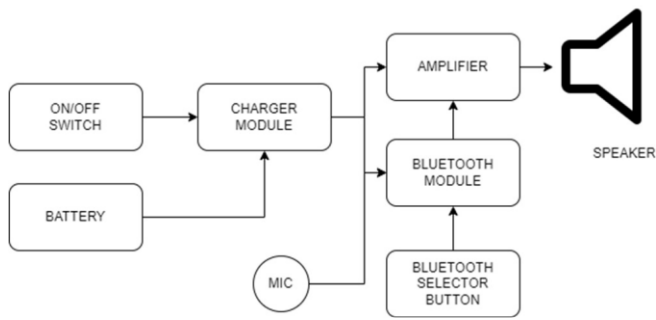


Fig. 1. CLIPPO Scheme



Fig. 2. CLIPPO Front Design

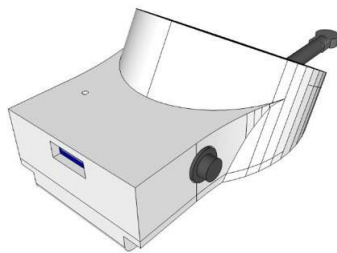


Fig. 3. CLIPPO Side Design

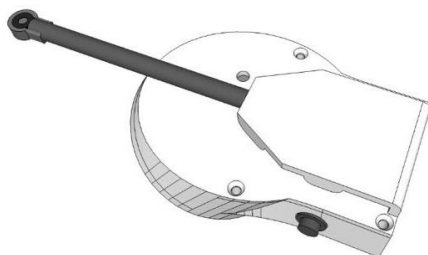


Fig. 4. CLIPPO Back Design

From the schematic in Fig. 1, CLIPPO is designed in a clamping device with the following design:

Fig. 2 is a design drawing of the front view of the loudspeaker clamp device. It can be seen that there are speakers at the front which are covered with a layer (casing) in the form of stripes. There is a Bluetooth selector button at the top to select Bluetooth mode or normal mode. Below there is an on/off button to turn off or turn on the loudspeaker.

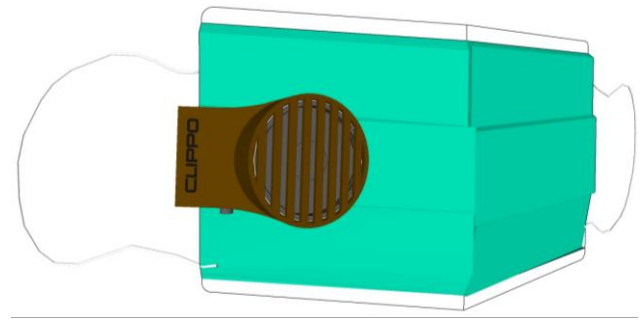


Fig. 5. CLIPPO On Medical Mask Front View

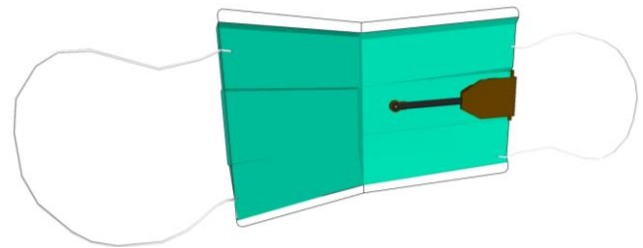


Fig. 6. CLIPPO On Medical Mask Back View

Fig. 3 is a side view design image, where we can see a hole for charging using a micro USB. In addition, in Fig. 3 there is also a button that functions as an off and on switch (ON/OFF).

In Fig. 4 there is a microphone with a copper cable that connects to the circuit. Furthermore, the clamp is also at the back of the product, so the loudspeaker can be clipped to the side of the mask. When this clamp is clamped on the mask, it can be seen in Fig. 5.

Fig. 6 is the back view of the clamp when it is attached to the mask.

Although the inventions made by the author are not perfect, according to the principle of sound transmission, "Any medium used for sound recording will eventually deteriorate" [8].

V. CONCLUSION

From the introduction, to the discovery of the problem and the resolution, it is concluded that this clip-shaped loudspeaker device can help amplify the voice in speaking. In addition, this loudspeaker can also be channeled to active speakers, so that to channel sound in a large room can be done with a Bluetooth connection. CLIPPO itself already has a patent pending number S00202104532. The implication of further research is connecting the Clippo into Bluetooth Device for communication with gadget or other peripheral device.

ACKNOWLEDGEMENT

We would like to thank Lembaga Penelitian dan Pengabdian Masyarakat (LPPM) UK Petra, Surabaya under its Grant in 2022.

REFERENCES

- [1] Budi Wahyono. "Ilmu Pengetahuan Alam 4", Jakarta, Book Center of the Ministry of National Education 2008, pp. 100.
- [2] Alice Cartaud, dkk Wearing a face mask against Covid-19 results in a reduction of social distancing, 6, 2020, National Institutes of Health, UNITED STATES, <https://journals.plos.org/plosone/article/file?id=10.1371/journal.pone.0243023&type=printable>
- [3] <https://www.cnbcindonesia.com/news/20200227130223-4-140843/ini-ternyata-penyebab-masker-langka-di-ri-saat-heboh-corona>
- [4] <https://www.alodokter.com/pakai-masker-seharian-sebabkan-skindemik-ini-solusinya>
- [5] "Getaran Dan Perambatan Bunyi Serta Macam-Macam Perambatan Bunyi", Muhammadiyah University, Sidoarjo, 2018, <http://eprints.umsida.ac.id/1729/1/GETARAN%2C%2028-02-2018.pdf>
- [6] Rusli Kastaman, "Bunyi dan Manusia", ProTVF vol 1 no 2, 2017, pp. 118
- [7] Nurshad Ali* and Farjana Islam, *The Effects of Air Pollution on COVID-19 Infection and Mortality—A Review on Recent Evidence*, , 5, 2020, Department of Biochemistry and Molecular Biology, Shahjalal University of Science and Technology, Sylhet, Bangladesh, <https://www.frontiersin.org/articles/10.3389/fpubh.2020.580057/full#h6>
- [8] T. A. Edison, *The State of Recorded Sound Preservation in the United States, A National Legacy at Risk in The Digital Age*, Washington, D.C., 2010. Pp. 66

NebulaX: A Therapeutic Mechanism Against Corona Virus

Felix Pasila*
Electrical Engineering Department
Petra Christian University
Surabaya, Indonesia
felix@petra.ac.id

Handry Khoswanto
Electrical Engineering Department
Petra Christian University
Surabaya, Indonesia
handry@petra.ac.id

Erandaru
Visual Communication Design
Petra Christian University
Surabaya, Indonesia
andar@petra.ac.id

Rhema Adhi
Mechanical Engineering Dept.
Institute Technology Sepuluh
Nopember
Surabaya, Indonesia
Rhema01adi@gmail.com

Hestiasari Rante
Dept. of Multimedia Engineering
Technology
Politeknik Elektronika Negeri
Surabaya, Indonesia
hestiasari@pens.ac.id

Henricus Soehartono
Electrical Engineering Department
Petra Christian University
Surabaya, Indonesia
heri@petra.ac.id

Abstract—COVID-19 is a disease caused by the Coronavirus. This virus spreads quickly worldwide. Indonesia, like many other countries around the world, is preparing to respond to additional cases and possible widespread transmission of the disease. As cases of COVID-19 is increasing day by day, public concern in Indonesia regarding the severity of the disease and population vulnerability is also growing. In new normal situation, it is necessary to have a device to eliminate the spread of the Coronavirus, by eliminating this virus in the human respiratory tract. We introduce a NebulaX, is an anti-COVID-19 therapeutic device. It is a nebulizer's device, controlled by the Controller. The program in the Controller converts liquid into steam, thus if the liquid is a drug, it can easily enter the respiratory system and kill bacteria and viruses. The Casing of NebulaX is made from food-grade materials that suitable and also save in the respiratory process. In very useful for the prevention and cure of COVID-19 with the market segment of patients, medical workers, people in crowded places, and middle-high income families. The results of NebulaX is a light version with the specification as follows: weight Version 3.1 = 7.8 kgs, materials plat stainless, plastic ABS, dimension 32cm*15cm*30cm, display LCD 5", control unit AT-Mega, temperature Sensor DS18B20, power consumption 220 VAC(240 Watt), warm Oxygen 2 Liter/minute, nebulizer 1 cc/minute and Hydrogen Generator 160 mL/minute. The implication of further research is connecting the NebulaX into Internet of Things mechanism for collecting data of people for datamining purposes.

Keywords—COVID-19, NebulaX, hydrogen generator, warm Oxygen, nebulizer, therapeutic device

I. INTRODUCTION

Until today, Coronavirus is continuing its spread across the world with about 70 million confirmed cases in 190 countries and more than 1.5 million deaths [1]. The virus is surging in many regions and countries that had apparent success in suppressing initial outbreaks are also seeing infections rise again. This virus spreads very rapidly and has a huge impact in the world, not only causing large numbers of deaths but also crippling the economy. This virus attacks human respiratory system. In some severe cases, COVID-19 can cause hypoxia and result in death. Recently, the vaccines for the COVID-19 virus are released and soon will be on market.

Meanwhile, to face the new normal, it is necessary to have a device to eliminate the spread of the Coronavirus, by eliminating the virus in the human respiratory tract. Therefore, we conducted study and developed NebulaX as an alternative device to use in the new normal.

The Coronavirus has a characteristic to die at the temperature of 70°C with inactivation time of 5 minutes [2]. Based on this fact, we use a heater and blower to introduce dry hot air to the respiratory tract. Since the Coronavirus can be found at the respiratory tract, we need a device that can change liquid to aerosol so that if the liquid is a drug, it can easily enter the respiratory system and kill the bacteria and virus. For this purpose, we use nebulizer to change liquid into aerosol.

This NebulaX has three main functions: oxidant therapy, medical therapy, and antioxidant therapy. In oxidant therapy, we use heaters to introduce hot air into the body. Then proceed with medical therapy, namely the insertion of food-grade herbs into the body, using the inhalation method, to kill the virus, that already register as Patent (with No. S00202103359) and Copyright with registered number EC00202058924 [3], [4]. Then it ends with antioxidant therapy, which is the introduction of hydrogen into the body, to relax, cleanse, and soothe the body. The combination of these three functions is very useful for the prevention and cure of COVID-19 with the market segment of COVID-19 patients, medical personnel, crowded places, and middle-high income households.

II. AIMS

The aim of this study is to provide an electrical therapy device to kill viruses consisting of: a heater, a blower, an atomizer or sometimes described as a Hydrogen-Oxygen Generator (HHO generator) and a controller to control the ignition and shutdown of the heater, blower, HHO producer and the atomizer. The electric therapy device further consists of a temperature sensor connected to the heater, a dimer connected to the heater, a PWM connected to a blower, the first relay connected to the HHO generator, a second relay connected to the atomizer, a display, and a number of indicators.

In addition, this study is also to support the Indonesian government program in handling the COVID-19 pandemic.

III. THEORETICAL BASIS

A. Corona Virus Disease 2019 (COVID-19)

In the beginning of 2020, the Centers for Disease Control and Prevention (CDC) began to be observing the flare up of an unused Coronavirus, SARS-CoV-2, which cause the respiratory illness presently known as COVID-19. Authorities begin to distinguish the infection in Wuhan, China. The World Health Organization (WHO) have declared a public health emergency relating to COVID-19. The common symptoms of COVID-19 are fever, breathlessness, cough, it takes 14 days for the patience to notice the symptoms [5].

B. Nebulizer

Atomizer or usually known as nebulizer, is a therapeutic device that convert liquid into aerosol or fine mist with the size of μm that can easily reach the inferior part of the respiratory tract, through mouth or nose [6]. An atomizer can be used with an electric compressor, which vaporizes drugs so they can be inhaled to open airways, or it can use vibrating ultrasound. The mesh atomizer uses a new type of technology that forces liquid pharmaceuticals through nozzle, which has multiple holes, to produce a fine mist or aerosol. The following factors influence the process of administering drugs to patients through the nebulizer system:

- The method of interface between the patient and the nebulizer, and
- The volume of air given to the patient breathing [7].

The time it takes to nebulize a regular dose of common bronchodilators such as albuterol (used for asthma, emphysema, and other lung conditions) varies from a particular brand of nebulizer and the dose flow rate from the gas supply source (i.e., compressed air/gas). An efficient nebulizer machine is required to supply the dose in about six minutes. There are certain techniques that can determine the performance of a nebulizer. This includes:

- Analysis by weighing the nebulizer before and after nebulization.
- Volumetric analysis.
- Measure the particle size distribution.
- After filtration, the inhaled drug is adjusted with the help of in vivo radionuclide lung scanning or infrared photo spectrometry [8], [9].

The methodology to measure nebulized aerosol shown in Fig. 1. A constant inhalation of $15 \text{ L}\cdot\text{min}^{-1}$ is drawn over (or through) the nebulizer. Nebulized aerosol containing a NaF solute tracer mixes with the entrained air. A low flow cascade impactor samples aerosol at $2 \text{ L}\cdot\text{min}^{-1}$ from this flow, and impacted aerosol can be subsequently desorbed and analyzed from each size fraction from which the droplet size distribution can be determined.

The methodology for measuring the nebulized aerosol is shown in Fig. 1. A constant inhalation of $15 \text{ L}\cdot\text{min}^{-1}$ is sucked on (or through) the nebulizer. The nebulized aerosol, which contains a NaF-Solute tracer, mixes with the drawn air. A low-flux cascade impactor removes aerosols at $2 \text{ L}\cdot\text{min}^{-1}$ from this stream and the affected aerosol can then

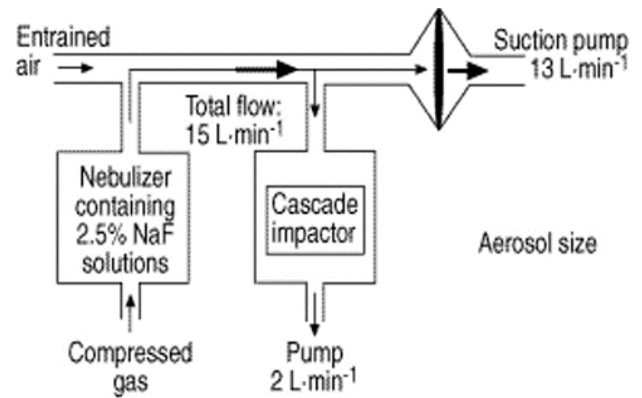


Fig. 1. The methodology to measure nebulized aerosol droplet size [10].

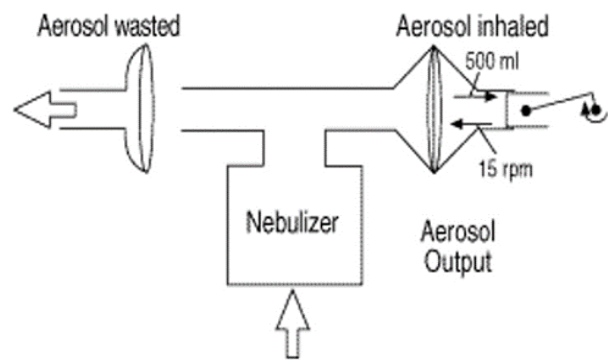


Fig. 2. Nebulizer scheme [10].

be desorbed and analyzed by any dimensional fraction from which the size distribution of the droplets can be determined.

In detail, the methodology for measuring the output of nebulized aerosol, as shown in Fig. 2. It is subject to the simulation of the breath of sinus flow, and the aerosol is collected on low-impedance electrostatic filters. Aerosols contain traces of sodium fluoride concentration, which can then be desorbed and measured electrochemically in rpm [10].

C. Hydrogen-Oxygen Generator (HHO Generator)

HHO generator is a hydrogen-oxygen generator with the aim of relaxing the body that is exposed to excessive oxidation. So, the function of the HHO generator is as an antioxidant for the body. Generally known as Hydrogen Water which can be consumed freely in the community. There are two HHO generator methods currently available, namely the Wet Cell method and the Dry Cell method [11]. In this research, we use Wet Cell Method for implementation of Therapeutic Device (NebulaX). In addition, two electrodes and a set of neutral plates are used in a typical Wet Cell. These plates are interconnected and connected to the edges of the two electrodes. In the design step the electrode and the neutral plate are completely submerged in electrolyte [12]. The O_2 gathering around the positive electrode starts to react with the metal plates used in the system which eventually causes corrosion of the plates. Also, here, the heat dissipation in the system is low compared to the dry cell configuration.

As if, the system heat will increase during the generator running which causes water vapor. The water vapor will mix with HHO gas and as a result the system efficiency is reduced [13].

IV. DEVICE DESIGN

NebulaX is a therapeutic device against COVID-19. It is combining three different therapeutic treatments which is heat treatment therapy or sauna therapy using heater and blower, herbal therapy using nebulizer with herbal liquid, and antioxidant therapy using HHO generator. These three-therapy treatments controlled by a controller for maximum efficiency.

The heater functions as a heat source and simultaneously functions as a sauna therapy, which is equipped with a temperature sensor to read the temperature of the heater, the dimmer, which regulates the ignition current of the heater so that the temperature of heater is not too low and does not rise too high. Indicator 3 used to indicate that heater is on. The temperature sensor is a PT-100 sensor. The PT-100 sensor is used because it has high accuracy and belongs to the RTD (Resistive Temperature Detector) group with a positive temperature coefficient, which means that the resistance value increases with increasing temperature. The heater is a heater with a working voltage of 220 V and 1000 W of Power.

The block diagram of the therapeutic device is shown in Fig. 3.

The blower draws hot air from the heater so that it reaches the mask (not shown in the picture). Blower is equipped with PWM which regulates the speed of hot air flow and indicator 2 as a sign that the blower is on. Blower is a blower with a working voltage of 12 V and a power of 50 W.

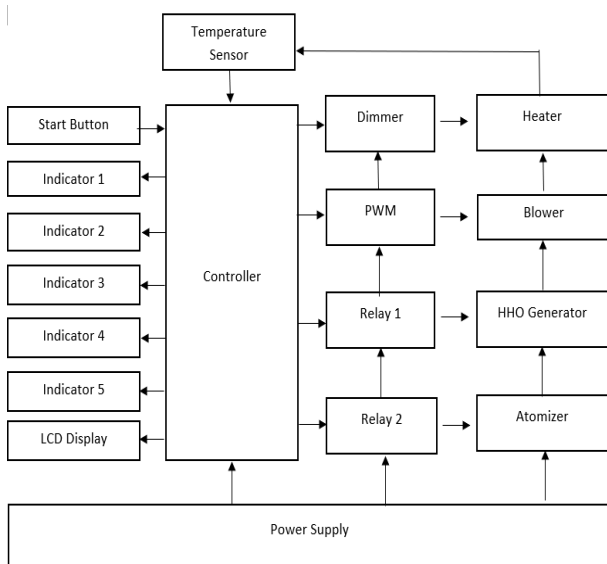


Fig. 3. NebulaX block diagram.

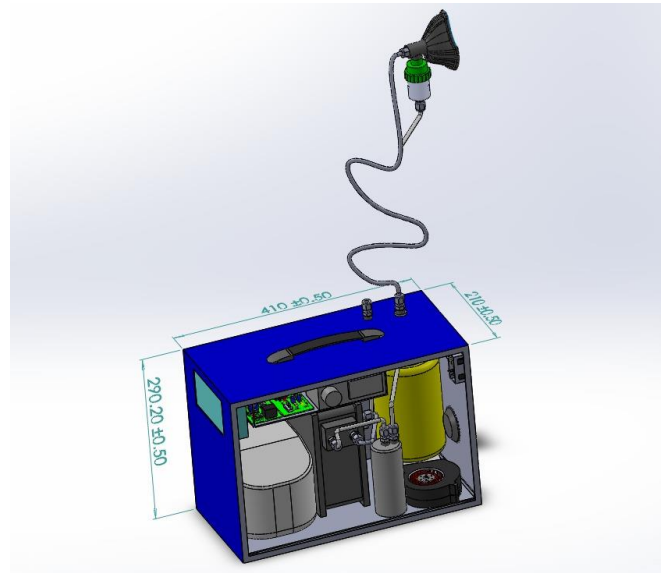


Fig. 4. NebulaX design Ver 2.1 (2019).

HHO generator produce HHO (oxyhydrogen) gas which functions for antioxidant therapy. The HHO generator is equipped with the first relay to turning on the HHO generator. Indicator 4 used as a marker that the HHO generator is active (on). The HHO generator is a hydrogen-generating device for the purpose of providing relaxation to the body that is exposed to excessive oxidation. Therefore, the function of producing HHO is as antioxidant therapy for the body. The technology for producing HHO can be in the form of wet cell technology and dry cell technology. The HHO generator is an HHO generator with a working voltage of 24 V and a current of 2.5 A.

The atomizer or well known as nebulizer is used as herbal therapy. It will convert drug/herbal liquid into aerosol or fine mist with the scale of the aerosol in μm . This atomizer is equipped with a second relay to turn on the atomizer and indicator 5 as a marker that the atomizer is active. The atomizer is an atomizer with a working voltage of 24 V and a current of 100 mA.

The controller basically controls the starting and stopping of the heater, the blower, the HHO generator, and the atomizer. The controller also manages the sensor, dimmer, PWM, first relay, second relay, indicators, and display. Furthermore, controller maintained the temperature between 56-60°C while the therapeutic device was functioning. The controller is the AVR ATmega 328 controller, the working voltage is 5 V with a current of 200 mA.

NebulaX is also equipped with LCD display to show the initial status of the device, temperature of the air produced, etc. Indicator 1 and 2 is used as status indicator for the device, whether it is in standby mode or already finished.

Fig. 4 is showing the design of NebulaX in 3 dimensions.

V. DEVICE DESIGN

NebulaX working procedure and implementation are presented in the Fig. 5 and Fig. 6 respectively.

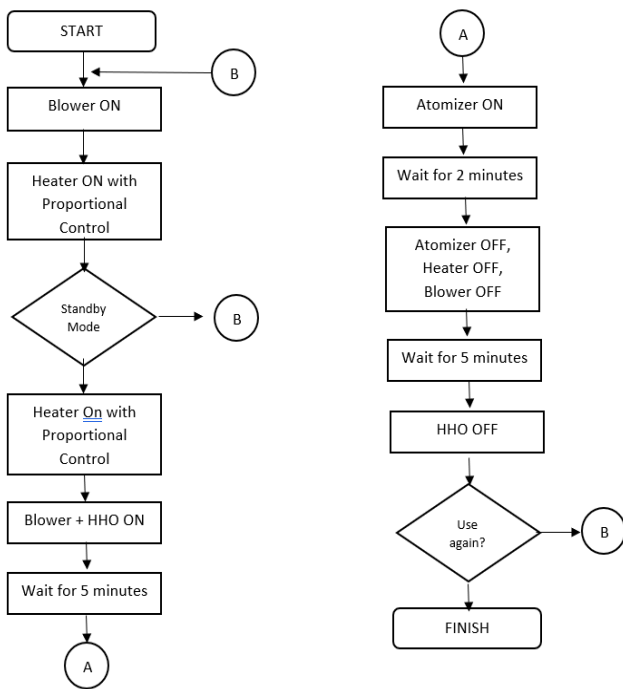


Fig. 5. NebulaX operational flowchart.

When the start button is pressed, electric power will be supplied to the appliance, the heater and blower turn on and a preparation time of approximately 3 to 5 minutes is required. After the green light on indicator 1 lights up, it indicates that the electric therapy device is ready for use. Then the start button is pressed, then the HHO generator starts to light up for approximately 5 minutes. The heater maintains its setting temperature (setting point). Then turn on the atomizer for about 2 minutes. After the 2 minutes are over, turn off the atomizer, blower and heater. Here, the HHO generator is still on and maintains this condition for approximately 5 minutes. After 5 minutes have ended, the red light on indicator 2 lights up indicating that the therapy process has been completed. For next use, we must wait until the red light on indicator 2 turns off and the green light on indicator 1 lights up, then we can press the start button.

In addition, the specification of NebulaX according to Fig 6. Can be described as follows:

- Weight Version 3.1 = 7.8 kgs
- Materials plat stainless, plastic ABS
- Dimension 32cm*15cm*30cm
- Display LCD 5"
- Control Unit AT Mega
- Standard Masker
- Temperature Sensor DS18B20
- Power 220 VAC (240 Watt)
- Function: Warm Oxygen 2 Liter/minute,
- Nebulizer 1cc/minute and Hydrogen Generator 160 mL/minute



Fig. 6. NebulaX Design 3.1 (2022)

VI. CONCLUSION

NebulaX is a therapeutic device against COVID-19 that combine three functions of therapies, which are sauna therapy, herbal therapy using nebulizer, and antioxidant therapy. This device claimed to be able to kill COVID-19 in human respiratory tract and help to prevent the spread of COVID-19 in Indonesia context. The dimension of NebulaX is suitable for handling in mobile. It is light and easy to use concerning the power. The idea of further research is connecting the NebulaX into Internet of Things mechanism for collecting data of people for datamining purposes.

ACKNOWLEDGMENT

We would like to thank Department of Education Ministry (KEMDIKBUD) under its Grant with number 073/E5/P6.02.00.PT/2022, on 16 March 2022.

REFERENCES

- [1] BBC News. Covid-19 pandemic: Tracking the global Coronavirus outbreak. <https://www.bbc.com/news/world-51235105>. Accessed on 30 August 2022.
- [2] Chin. Alex WH, Julie T S Chu, Mahen R A Parera, Kenrie P Y Hui, Hui Ling Yen, Michael C W Chan, et al, "Stability of SARS-Cov-2 in Different Environmental Condition," The Lancet Microbe, vol. 1, issue 1, e10. April 2020. DOI: [https://doi.org/10.1016/S2666-5247\(20\)30003-3](https://doi.org/10.1016/S2666-5247(20)30003-3)
- [3] Pasila, F., et al. Patent ALAT TERAPI ELEKTRIK UNTUK MEMBUNUH VIRUS, with registered No. S00202103359, 2021
- [4] Pasila, F., et al. Copyright No. EC00202058924 SOFTWARE ALAT TERAPI COVID ELIMINATOR, 2020
- [5] Unhale, Shrikrushna & Bilal, Quazi & Sanap, Shubham & Thakhre, Suraj & Wadatkar, Shreya & Bairagi, Rohit & Sagrule, Prof & Biyani, Dr. (2020). A REVIEW ON CORONA VIRUS (COVID-19). International Journal of Pharmaceutical and Life Sciences. 6. 109 - 115.
- [6] Sahiti, et al, "Nebulizers: A Review Paper", International Journal of Advanced Research in Computer Science, Volume 8, No. 5, May-June 2017.
- [7] H. Lin, G. Wan, J. B. Fink, W. Liu and K. Liu. " Influence of Nebulizer Type With Different Pediatric Aerosol Masks on Drug Deposition in a Model of a Spontaneously Breathing Small Child." Vol 57 No 11, November. 2012.
- [8] Hess D, Fisher D, Williams P, Pooler S, Kacmarek RM. "Medication nebulizer performance: effects of diluent volume, nebulizer flow, and nebulizer brand." Chest, 110(2): 498-505, 1996.
- [9] "A New System for Understanding Nebulizer Performance." Respiratory Care. Vol 52, no. 8, August. 2007.

- [10] J. Boe, J.H. Dennis, B.R. O'Driscoll, T.T. Bauer, M. Carone, B. Dautzenberg, P. Diot, K. Heslop, L. Lannefors, *European Respiratory Journal* 2001 18: 228-242.
- [11] TS De Silva, L Senevirathne and TD Warnasooriya "HHO Generator – An Approach to Increase Fuel Efficiency in Spark Ignition Engines", *Euro. J. Adv.Eng. Tech.*, 2015, 2(4):1-7.
- [12] Smith and Jerry.US Patent US 8,168,047 B1, 01 May 2012.
- [13] Attila GÖLLEI, *Measuring and Optimization of HHO Dry Cell for Energy Efficiency*, Hungary, 2014.

Control System Design to Increase Low Voltage Ride Through (LVRT) Capacity in Wind Turbine Using STATCOM Base on Control Linear Quadratic Regulator (LQR)

Nurul Chairunnisa Noor

Department of Electrical Engineering
Hasanuddin University
Makassar, Indonesia
channur30@gmail.com

Indar Chaerah Gunadin

Department of Electrical Engineering
Hasanuddin University
Makassar, Indonesia
indarcg@gmail.com

Ansar Suyuti

Department of Electrical Engineering
Hasanuddin University
Makassar, Indonesia
ansarsuyuti@gmail.com

Abstract - Energy production from the wind turbine power is an intermittent energy source, producing a fluctuating amount of electrical energy according to the uncertain wind energy potential, making the risk of disconnecting the power grid very high and wind power plants can be disconnected from the power grid due to excess or lack of production capacity of the wind turbine. This matter can have an impact on the stability of the transmission system in the electricity network. This research aim: to increase the capacity of the LVRT (Low Voltage ride through) in the turbine so that the generator will continue to operate and not be disconnected from the transmission line when the disturbance occurs. In this study the STATCOM (Static synchronous compensator) will be used to regulate voltage by generating or absorbing reactive power, this tool reduces the risk of voltage drop when the reactive power is working. The method used in this research is the LQR (Linear Quadratic Regulator) system for optimal control in linear systems, used to adjust the performance of STATCOM and increase the capacity of the LVRT. The simulation results show that LQR can produce a control system that can measure reactive currents when there is a voltage drop and can achieve steady-state stability when a disturbance occurs.

Keywords—LVRT (Low Voltage ride through), STATCOM (Static synchronous compensator), LQR (Linear Quadratic Regulator), steady-state stability.

I. INTRODUCTION

Indonesian country is very feasible in developing and producing renewable energy, especially wind energy. The largest wind power plant has been built in the Sidrap area of South Sulawesi. In the wind power generation system, the wind turbine will take advantage of wind speed and convert it into mechanical energy. After that process in the turbine, the generator will convert this energy into electrical energy [1]. When there is a fault across the stator terminals of a wind turbine generator, the electrical torque is reduced, but the mechanical torque is still present as the wind continues to blow. This condition causes the rotor speed to increase, and if the voltage drop continues, the turbine accelerates the rotor and the rotor speed can become unstable [2]. Increased penetration of wind energy in wind turbines has a significant impact on grid stability. Frequency and voltage stability are very important as they relate to system reliability and safety [3]. This is an important aspect in the design and operation

of power plants as wind turbines grow in size and must continue to operate without being disconnected from the grid [4].

A large loss of generating capacity in a power plant combined with an increase in wind energy production creates problems for the power generation system [4]. This has a significant impact on grid stability when generators must remain connected to the grid [5]. This interference causes Low Voltage Right Through (LVRT) instability. When a fault occurs at the Stator terminals of a wind turbine generator, the electrical torque is reduced and the mechanical torque is still present because the wind is still blowing [6]. The maximum voltage that a wind turbine can sustain without suffering from rotor speed instability, known as the drive-through capability of low-voltage wind turbines, decreases either in magnitude or time [7]. The wind turbine rotor speed try to achieve stability on the index which requires a certain voltage [8].

LVRTs are required in wind turbine generators when grid disturbances or large load changes cause temporary voltage dips in the grid [9]. To maintain system stability and reduce the risk of brownouts, the required LVRT operation is specified in grid codes issued by grid operators [10]. Each voltage source converter's principal control level has been updated utilizing the LVRT approach without the use of a communication link [11]. The power generation must maintain grid synchronization even in the event of a severe voltage decrease [12]. Since wind turbines have different characteristics than normal power plants [13], the grid code was created taking into account the synchronous generators used in conventional power plants. Voltage and frequency standards comply with applicable regulations and quickly return to normal when the system is disturbed. The simulation modeling carried out is the Sulawesi interconnection system starting with the usual situation of the Sidrap PLTB on the system when a three-phase short circuit occurs, then the entry of STATCOM on the system.

II. MODEL OF THE SYSTEM

A. Generator model

The system model in this study is to make the LVRT capacity in wind power plants even better by using Linear Quadratic Regulator (LQR). The system model will include wind turbines, generators, and STATCOM. Generator modeling uses a two-axis model that accounts for transient

effects while ignoring sub-transient effects. Transient effects are related to the rotor circuit. The expression that the rotor motion of a synchronous machine is the product of the rotor moment of inertia times the angular velocity is written in the vibration equation as (1).

$$J \frac{d^2 \theta_m}{dt^2} = T_a = T_m - T_e \quad N - m \quad (1)$$

The fundamental equation that affects the dynamics of the rotation of the synchronous machine on the stability problem is also called the swing equation of the machine can be written as (2).

$$\frac{2H}{\omega_s} \frac{d\omega}{dt} = P_m - P_e \text{ per unit} \quad (2)$$

The change in P_e is primarily determined by the system transmission, distribution, and load conditions when the generator is delivering power. Disturbances in the grid created by load changes or circuit breaker operation can cause rapid changes in generator output during electromechanical transients. The engine has two stator circuits and two rotor circuits, the network generated by load changes or circuit breaker operation can cause the generator output to change rapidly in the presence of electromechanical transients. The differential equations describing this system are simplified because λ_d and λ_q are neglected in the stator equation.

$$E + x_d I_d = E'_q + x'_d I_d \quad (3)$$

$$E_d + x_q I_q = E'_d + x'_q I_q \quad (4)$$

$$\tau'_{q0} E'_d = -E'_d (x_q - x'_q) I_q \quad (5)$$

$$E'_q = \frac{1}{\tau'_{d0}} (E_{FD} - E) \quad (6)$$

$$T_e = E'_d I_d + E'_q I_q - (L'_q - L'_d) I_d I_q \quad (7)$$

$$\tau_j \omega = T_m - D \omega [E'_d I_d + E'_q I_q - (L'_q - L'_d) I_d I_q] \quad (8)$$

$$\delta = \omega - 1 \quad (9)$$

$$E = E'_d - (x_d - x'_d) I_d + E_\Delta \quad (10)$$

This equation can represent the two-axis generator model in the form of a diagram as follows:

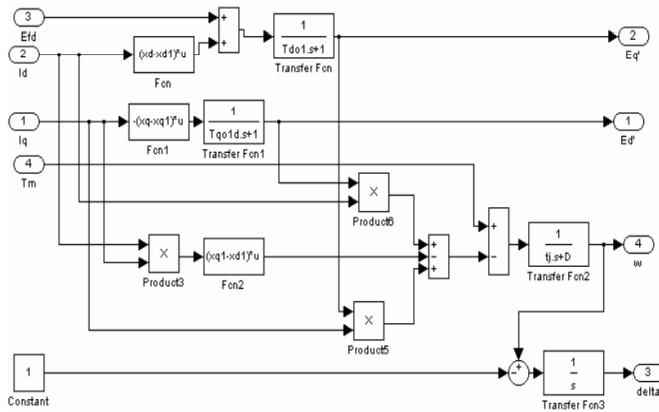


Fig. 1. Two-axis generator model

The magnetic field controls the magnitude of the voltage generated and can be adjusted by changing the current through the magnetic field coils. Increasing the field current increases the resulting voltage and vice versa. The excitation system that controls the generator EMF, output voltage, power factor. Excitation model current can be thought as in Fig. 2.

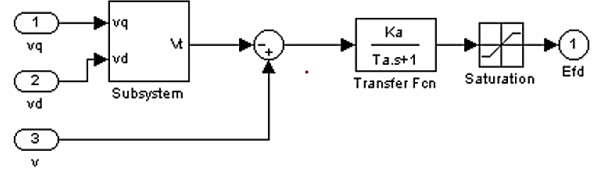


Fig. 2. the excitation model

A system designed to regulate the engine speed on a generator with very high resistance in the event of a load change can be seen in the governor, the governor is a rotor speed controller on the generator which functions to stabilize the mechanical torque value into the generator input.

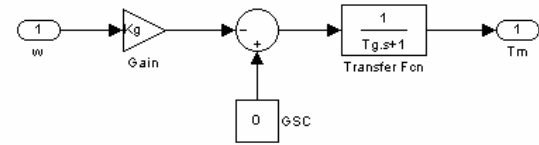


Fig. 3. The governor model

B. The System Model

If the state of the system is asynchronous after a disturbance, efforts should be made to bring the system back into sync. The ultimate goal achieved with this journal is steady-state stability. Steady-state stability is the ability of the power system in the generator to accept disturbances that occur near the equilibrium point under certain conditions. This type of stability depends on the characteristics of the components that make up the power system, such as generators, loads, the grid, and the control of the system itself. The generator model used is a simple generator (constant voltage source) because it only involves disturbance around the equilibrium point. For more details, the system model is made as in Fig. 4.

This system control model is recommended for checking the power performance of systems including generators, wind turbines and STATCOM.

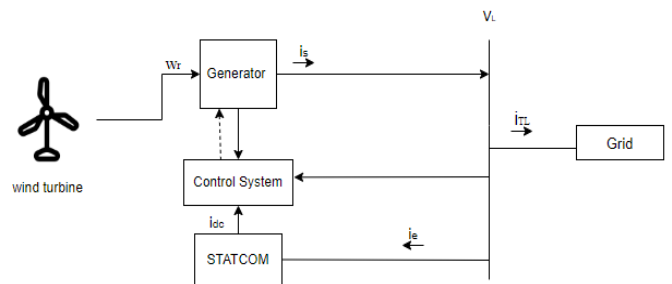


Fig. 4. The system model

C. The STATCOM Model

Reactive power control by the STATCOM is done by comparing the terminal voltage values between the STATCOM and the system. If the STATCOM voltage is low, the STATCOM will absorb the reactive power of the system. If the value is higher than the system, it will generate reactive power in the system. The working principle of STATCOM is shown in (11) – (13).

$$P = \frac{v_s v_c \sin \delta}{X_L} \quad (11)$$

$$Q = \frac{v_s(v_s - v_c) \sin \delta}{X_L} \quad (12)$$

$$S = 3 \frac{v_s v_c}{X_L} \sin \delta - j3 \left(\frac{v_s v_c}{X_L} \cos \delta - \frac{v_s^2}{X_L} \right) = P - jQ \quad (13)$$

Power system stability can generally be defined as the ability of a power system to remain synchronized during and after a fault. This definition also applies to systems that operate by interconnecting multiple generators (multi machine). The dynamic behavior of the STATCOM can be written as (14) – (17).

$$i_{de} = \frac{1}{L_f} [(v_{ds} - e_d) - R_f i_{de}] + \omega_s i_{qe} \quad (14)$$

$$i_{qe} = \frac{1}{L_f} [(v_{qs} - e_q) - R_f i_{qe}] + \omega_s i_{de} \quad (15)$$

$$v_{dc} = \frac{k}{c} (i_{de} \cos \alpha + i_{qe} \sin \alpha) - \frac{v_{dc}}{RC} \quad (16)$$

$$e_d = k v_{dc} \cos \alpha, \quad e_q = k v_{dc} \sin \alpha \quad (17)$$

III. DESIGN CONTROL SYSTEM

The first step in control system design is linearization, we can say x_0 is the initial state and u_0 can be the appropriate input vector with small signal point balance. If there is a disturbance in the system then:

$$\begin{aligned} x &= x_0 + \Delta u \\ &= f[(x_0 + \Delta u), (u_0 + \Delta u)] \end{aligned} \quad (18)$$

If the disturbance is assumed to be small and the function is nonlinear $f = (x, u)$ can be solved by the Taylor series as (19).

$$\begin{aligned} x_i &= x_{i0} + \Delta x_i = f[(x_0 + \Delta u), (u_0 + \Delta u)] \\ = f_i &= (x_0, u_0) + \frac{\partial f_i}{\partial x_1} \Delta x_1 + \dots + \frac{\partial f_i}{\partial x_n} \Delta x_n + \frac{\partial f_i}{\partial u_1} \Delta u_1 \\ &+ \dots + \frac{\partial f_i}{\partial u_r} \Delta u_r \end{aligned} \quad (19)$$

Then the linearization of the equation is:

$$\Delta x = A \Delta x + B \Delta u \quad (20)$$

$$\Delta y = C \Delta x + D \Delta u \quad (21)$$

After we determine the eigenvalues in the matrix, this value is a scalar quantity with a parameter λ which is solved by (22).

$$A \phi = \lambda \phi \quad (22)$$

The eigenvalues determine the stability of the system. To determine the eigenvalues you can use (23).

$$(A - \lambda I) \phi = 0 \quad (23)$$

Control system in general can be expressed in (24).

$$\dot{x} = Ax + Bu \quad (24)$$

Control system design generally chooses a vector $u(t)$ so that the given performance index can be minimized. Then we can get the linear control law relationship. Where K is the matrix $r \times n$

$$u(t) = -Kx(t) \quad (25)$$

Therefore, the design system of the optimal regulator control system based on the quadratic performance index refers to the determination of the K matrix elements. Determination of the optimal control vector $u(t)$ for the system can be written as (26).

$$J = \int_0^{\infty} (x^t Q x + u^t R u) dt \quad (26)$$

The Q and R matrices determine the relative error and energy cost. In this case, it is assumed that the control vector $u(t)$ does not change. The optimal control system will minimize the performance index and the system will be stable.

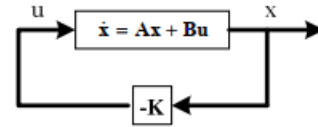


Fig. 5. Optimal control system

By substituting the optimal control equation and vector $u(t)$ we get:

$$\dot{x} = Ax - BKx = (A - BK)x \quad (27)$$

Then replace the optimal control vector equation $u(t)$ with the vector equation $u(t)$:

$$J = \int_0^{\infty} x(Q + K.RK)x dt \quad (28)$$

To see the results of the optimization parameter problem, the following equation is used:

$$x((Q + K.RK)x) = -\frac{d}{dt}(x.p x) \quad (29)$$

The next system design is to solve the reduced Riccati matrix equation:

$$A.P + PA - PBR^{-1}B.P + Q \quad (30)$$

The result of the reduced Riccati matrix is the P matrix after which it is substituted in the equation:

$$u(t) = -Kx(t) = R^{-1}B^* P x(t) \quad (31)$$

The result of this equation is the optimal matrix.

IV. SIMULATION RESULT

The performance of control system was evaluated using Matlab/Simulink simulations. First we see the results of the usual situation of the Sidrap PLTB on the system when a three-phase short circuit occurs before installing STATCOM We can see in the Fig. 6 to Fig. 9.

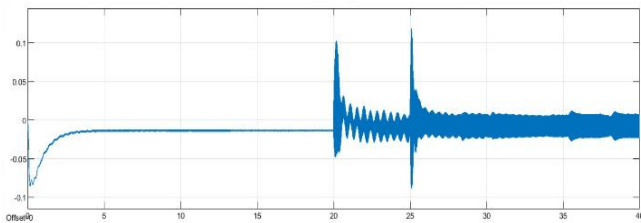


Fig. 6. d-axis Generator

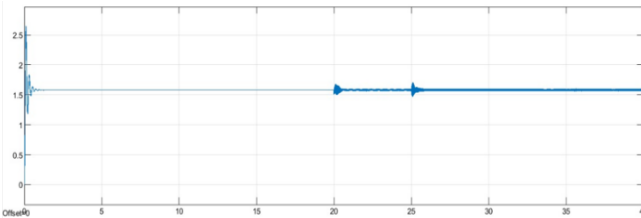


Fig. 7. q-axis Generator

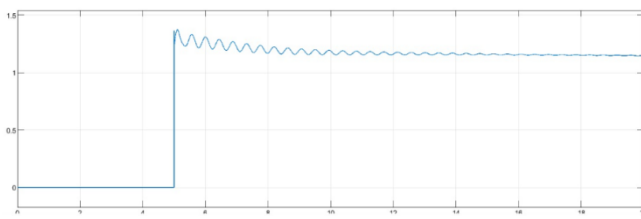


Fig. 8. Stator

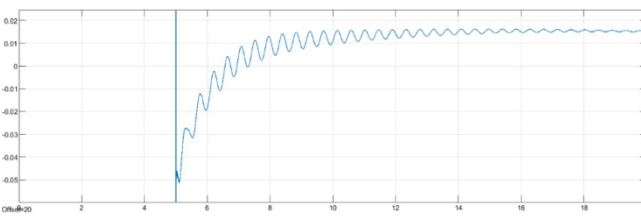


Fig. 9. Rotor

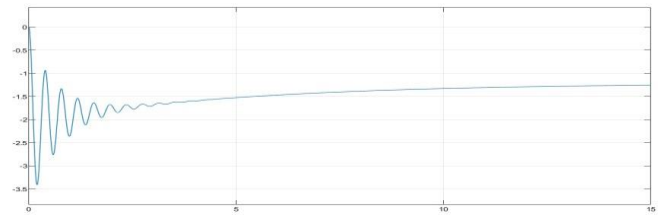


Fig. 10. d-axis Generator

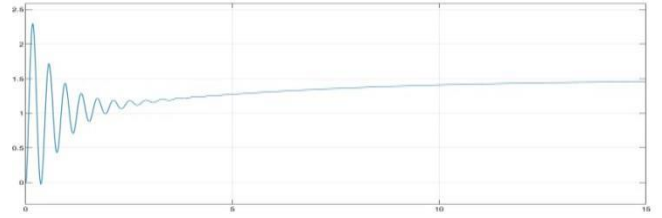


Fig. 11. q-axis Generator

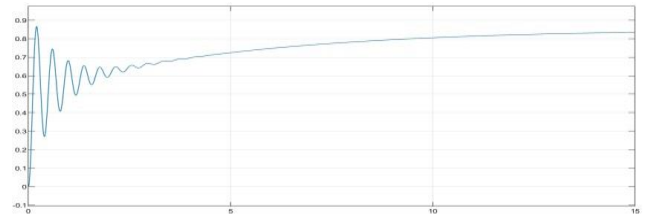


Fig. 12. Stator

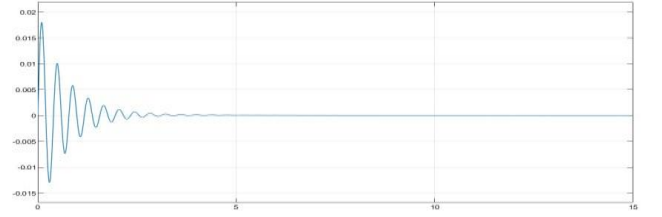


Fig. 13. Rotor

To find out the system can achieve stability or not after installing STATCOM system, it can be seen from the response of the generator on the system. The response of the d-axis and q-axis of the generator can be seen in Fig. 10 and Fig. 11.

We can see that the results of the d-axis and q-axis generators show significant changes to the addition of STATCOM capacity. The response from the stator can be seen in Fig. 12.

To stabilize the generator speed and ease the calculations, the STATCOM and stator current are assumed equal. The response of the rotor can be seen in Fig. 13.

The greater the moment of inertia, the smaller the value of the rotor angle. By reducing the mechanical torque during rotor acceleration, its speed can be decelerated and stabilized more quickly. After knowing the results of the rotor, we can compare the simulation results for static and dynamic generator loads. The response of static load can be seen in Fig. 14.

In the simulation, it can be seen that the static load on the Sidrap PLTB generator overshoots at 5 seconds and oscillates slightly until it finally reaches its steady state value. The response of dynamic load can be seen in Fig. 15.

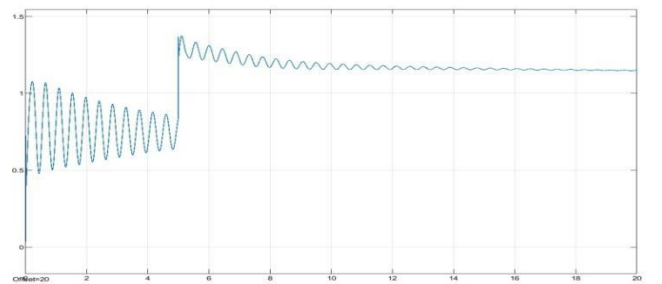


Fig. 14. Static Load Generator

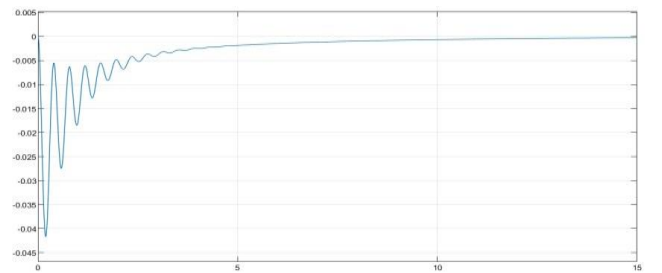


Fig. 15. Dynamic Load Generator

With the simulation results from dynamic loads, the results show that the system is getting better with smaller oscillations and a faster peak response and there is no overshoot before getting steady state stability. From the simulation results after linearization, the optimal Eigen value is obtained as followed:

$$E = 1.0e + 04$$

$$-0.0634 + 0.000i$$

$$-6.6663 + 0.0377i$$

$$-6.6663 - 0.0377i$$

The result of the reduced Riccati matrix we can get the optimal gain matrix k as followed:

$$K = 1.0e + 04$$

-1.0006	0.0029	0.3242
0.0029	-1.0079	-0.9313

V. CONCLUSION

The simulation results by adding a control system, the LVRT capacity has increased and quickly makes the STATCOM control better, it can be seen from the response of the generator with a dynamic load having a higher peak response and a longer stability time compared to a generator with a static load. Using the LQR system makes the generator response oscillations to dynamic and static loads more damped and achieve steady state stability faster and the STATCOM response value will be close to the recommended value of 1 pu.

REFERENCES

- [1] Y. M. Alsmadi et al., "Detailed Investigation and Performance Improvement of the Dynamic Behavior of Grid-Connected DFIG-Based Wind Turbines under LVRT Conditions," *IEEE Trans Ind Appl*, vol. 54, no. 5, pp. 4795–4812, Sep. 2018, doi: 10.1109/TIA.2018.2835401..
- [2] H.J. Lee, S. H. Lim, and J. C. Kim, "Application of a superconducting fault current limiter to enhance the low-voltage ride-through capability of wind turbine generators," *Energies (Basel)*, vol. 12, no. 8, 2019, doi: 10.3390/en12081478..
- [3] H. Rezaie and M. H. Kazemi-Rahbar, "Enhancing voltage stability and LVRT capability of a wind-integrated power system using a fuzzy-based SVC," *Engineering Science and Technology, an International Journal*, vol.22,no.3,2019,doi:10.1016/j.jestch.2018.12.018.
- [4] L.Liu and S.Wang, "Improving low voltage ride-through with STATCOM and SDBR for wind turbine with squirrel-cage induction generator," *European Journal of Electrical Engineering*, vol. 21, no. 2, 2019, doi: 10.18280/ejee.210208.
- [5] E. Gatavi, A. Hellany, M. Nagrial, and J. Rizk, "An integrated reactive power control strategy for improving low voltage ride-through capability," *Chinese Journal of Electrical Engineering*, vol. 5, no. 4, 2019, doi: 10.23919/CJEE.2019.000022.
- [6] Y. Neyshabouri, S. K. Chaudhary, R. Teodorescu, R. Sajadi, and H. Iman-Eini, "Improving the Reactive Current Compensation Capability of Cascaded H-Bridge Based STATCOM under Unbalanced Grid Voltage," *IEEE J Emerg Sel Top Power Electron*, vol. 8, no. 2, 2020, doi: 10.1109/JESTPE.2019.2916571.
- [7] Z. Rafiee, S. S. Najafi, M. Rafiee, M. R. Aghamohammadi, and M. Pourgholi, "Optimized control of Coordinated Series Resistive Limiter and SMES for improving LVRT using TVC in DFIG-base wind farm," *Physica C: Superconductivity and its Applications*, vol. 570, 2020, doi: 10.1016/j.physc.2020.1353607.
- [8] G. Lou, Q. Yang, W. Gu, and J. Zhang, "An improved control strategy of virtual synchronous generator under symmetrical grid voltage sag," *International Journal of Electrical Power and Energy Systems*, vol. 121, 2020, doi: 10.1016/j.ijepes.2020.106093.
- [9] M. Nadour, A. Essadki, and T. Nasser, "Improving low-voltage ride-through capability of a multimegawatt DFIG based wind turbine under grid faults," *Protection and Control of Modern Power Systems*, vol. 5, no. 1, 2020, doi: 10.1186/s41601-020-00172-w.
- [10] F. J. Lin, K. H. Tan, W. C. Luo, and G. D. Xiao, "Improved LVRT Performance of PV Power Plant Using Recurrent Wavelet Fuzzy Neural Network Control for Weak Grid Conditions," *IEEE Access*, vol.8,pp. 69346–69358, 2020, doi: 10.1109/ACCESS.2020.2984803.
- [11] H.Bahramian-Habil, H.A.Abyaneh, and G. B. Gharehpetian, "Improving LVRT capability of microgrid by using bridge-type fault current limiter," *Electric Power Systems Research*, vol. 191, Feb. 2021, doi: 10.1016/j.epr.2020.106872.
- [12] J. Zhang and Y. Huang, "Research on low voltage ride through control technology based on dynamic voltage restorer," 2020. doi: 10.1109/EI250167.2020.9347277.
- [13] A.Gencer, "Analysis and control of low-voltage ride-through capability improvement for PMSG based on an NPC converter using an interval type-2 fuzzy logic system," *Elektronika ir Elektrotechnika*, vol. 25, no. 3, 2019, doi: 10.5755/j01.eie.25.3.23678

Design of Sepic Converter for Renewable Energy System

Ratna Ika Putri

Electrical Engineering Department
State Polytechnic of Malang
Malang, Indonesia
ratna.ika@polinema.ac.id

Ika Noer Syamsiana

Electrical Engineering Department
State Polytechnic of Malang
Malang, Indonesia
ikanoersyamsiana@polinema.ac.id

Ferdian Ronilaya

Electrical Engineering Department
State Polytechnic of Malang
Malang, Indonesia
ferdian@polinema.ac.id

Surya Nata

Electronics Engineering Department
State Polytechnic of Malang
Malang, Indonesia
suryanata0502@gmail.com

Septyana Riskitasari

Electronics Engineering Department
State Polytechnic of Malang
Malang, Indonesia
septyanariskitasari@polinema.ac.id

Abstract— The use of renewable energy is increasing to meet the need for electrical energy because the availability of fossil energy as fuel for electricity generation is running low. In addition, the use of renewable energy is environmentally friendly and pollution-free. The use of renewable energy systems requires a power converter that plays an important role to produce high power quality and efficiency. In this article, a Sepic converter circuit is designed for applications in photovoltaic systems. The Sepic converter performance is simulated using PSIM. In addition, the Sepic converter's hardware prototype was made and tested in a laboratory using an Arduino Uno microcontroller-based PWM generator. The duty cycle of the PWM signal, which is controlled by the microcontroller, determines how efficiently the Sepic converter performs. Based on the results of the simulation test and experiments on the plant, the designed Sepic converter can work well with a switching frequency of 31 kHz. It will provide an output voltage larger than the input voltage during a duty cycle over 50%.

Keywords—Sepic converter, dc/dc converter, renewable energy

I. INTRODUCTION

The use of renewable energy is currently increasing in proportion to the limitations of fossil energy as fuel for electricity generation. Demand for electrical energy is projected to increase with an average growth of around 5.9% per year [1]. This condition causes an energy crisis in Indonesia so energy diversification by increasing the supply of new and renewable energy is needed to ensure energy availability. The development of renewable energy sources such as hydropower, geothermal, wind, solar, marine, and biomass has a lot of potentials if developed by Indonesia. Utilization of various types of renewable energy in the form of a photovoltaic, wind turbine, micro-hydro, and others requires a power converter to be used to adjust the input voltage in accordance with the application requirement. Power converters have already become a crucial component of power systems and driver engineering. Because it can

stabilize the output voltage even in unpredictable weather conditions, the converter implementation is the most important part of the hybrid renewable energy system (HRES). The power quality of a renewable energy system is highly dependent on the power converter's stable operation and control techniques. However, the majority of conventional converters and control techniques used in HRES have a number of drawbacks. As a result, numerous studies on the design of DC-DC converters and effective control techniques for HRES have been conducted [2]-[6].

The use of electronic-based DC-DC converters will provide more efficient results than conventional power conversion techniques. Several types of converters have been researched and used in renewable energy systems, such as Buck converter, Boost Converter, Buck-Boost converter, and Sepic converter. A combined Sepic, Cuk, and Zeta converter have been used in hybrid PV systems and wind turbines that use maximum power extraction with the perturb & observe method. Based on the simulation results, this topology can produce stable energy and has good performance [7]. A Sepic converter combined with a Cuk converter is used in hybrid wind/PV systems. Based on the simulation results, the converter can produce greater power efficiency [4], [8].

The use of a Sepic converter in a hybrid energy system has been simulated and proven to produce a good performance. The prototype of the circuit is designed using embedded systems [5]. The use of a Sepic converter that operates in CCM gives a high efficiency in renewable energy applications [6], [9], [10]. In addition, this converter is also suitable for multi-input converters that are applied in hybrid systems [11].

In this article, a Sepic converter will be designed for a renewable energy system whose performance will be tested through simulation and experiment. Simulation is carried out using PSIM, where the component parameters use values that are commonly used in the market and are adjusted to the hardware. Meanwhile, the hardware is tested in the laboratory using an Arduino Uno microcontroller as a PWM to drive the switching components on the Sepic converter. Testing the performance of the circuit is done by providing changes in the duty cycle of PWM pulse and input voltage. The simulation results will be compared with the experimental results.

II. SEPIC CONVERTER

One type of converter, the sepic converter, would change the value of output voltage to be more or lower than the input voltage's value depending on the duty cycle (D) value that the circuit receives [12]. A Sepic converter is consisted of a switching component (Q1), two inductors, two capacitors, and a diode, as shown in Fig. 1(a). How the Sepic converter will work is dependent on the duty cycle which will determine the condition of the switch (Q1). There are two conditions in this converter, that is when Q1 is on or when Q1 is off, where the amount of energy exchanged is controlled by switch Q1 [3]. When switch Q1 is active, as shown in Fig. 1(b), the diode (D1) will be reverse biased so that current from the input will flow through inductors L1 and L2. This will increase current I_{L1} and voltage V_{L1} will approach the input voltage. The current in inductor L2 will become increasingly negative so that the voltage on L2 will approach the voltage on the capacitor (Cs). Energy and current that are stored in L2 will flow to the load.

On the other hand, when switch Q1 is off, as shown in Fig. 1(c), the diode will be forward biased so that the current value in Cs will have the same value as the current L1 and the inductor's current I_{L2} will increase and then send power to the load. During this cycle, inductor L1 will charge capacitor Cs and power is sent to the load from inductors L1 and L2. Fig. 2 shows the inductor's current, capacitor, and switch Q1's conditions on the Sepic converter. The magnitude of the Sepic converter's output voltage can be expressed by (1).

$$V_{out} = \left(\frac{D}{1-D} \right) V_{in} \quad (1)$$

Where D is the duty cycle, V_{out} is the output voltage of the Sepic converter, and V_{in} is the input voltage of the Sepic converter.

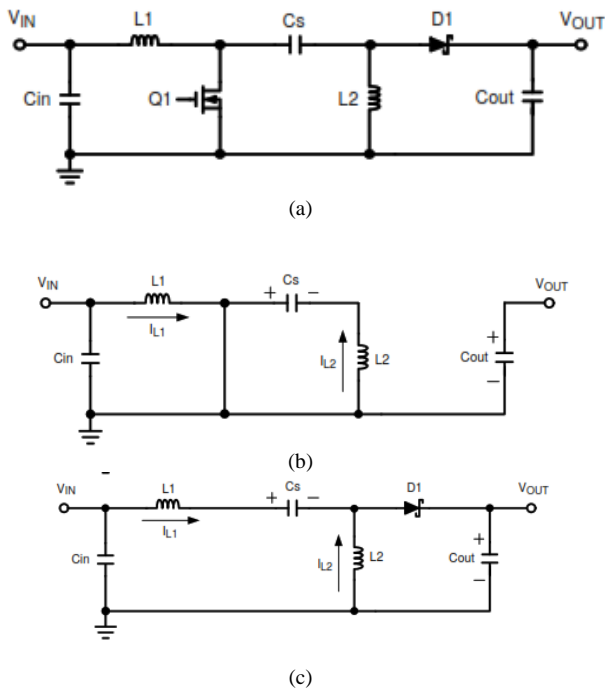


Fig. 1. (a) Sepic Converter (b) During on Condition (c) During off Condition.

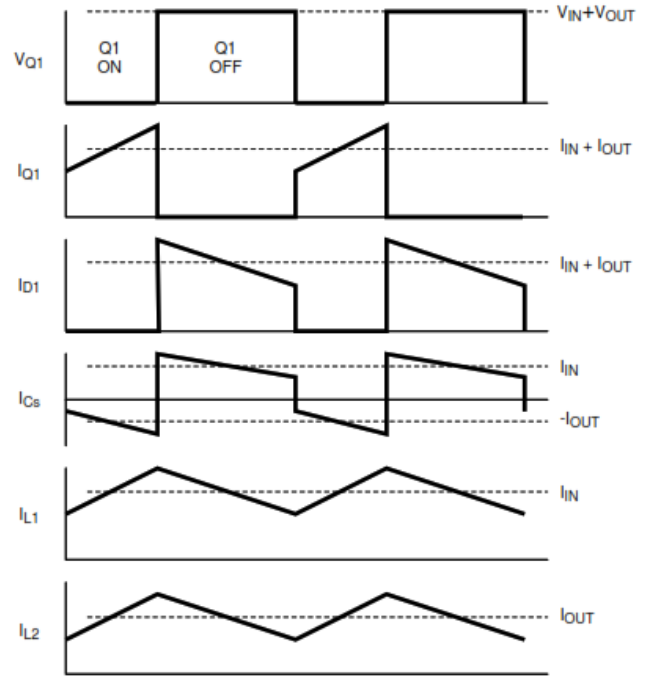


Fig. 2. Current inductor and capacitor in Sepic converter.

III. SEPIC CONVERTER DESIGN

In this paper, the output of the Sepic converter is connected to the load, and the input voltage of the Sepic converter is connected to the solar panel's output. Sepic converter operates in CCM. Maximum input voltage of the photovoltaic is 36 V, with the output voltage of the Sepic converter which will be connected to the resistive load.

• Inductor Selection

The value of the inductor is determined based on the peak to peak ripple current where ripple current in the inductor is limited to 25% of the input current (I_{in}) as shown in (2).

$$\Delta I_L = I_{in} \times 25\% = I_{out} \times \frac{V_{out}}{V_{in(min)}} \times 25\% \quad (2)$$

With a maximum output current of 10 A, the peak-to-peak inductor current ripple (ΔI_L) is 6.5 A. The value of inductors can be calculated by (3).

$$L_1 = L_2 = L = \frac{V_{in(min)}}{\Delta I_L \times f_{SW}} \times D_{max} \quad (3)$$

Where the switching frequency (f_{SW}) is 31 kHz and the value of D_{max} at the minimum input voltage can be determined by (4).

$$D_{max} = \frac{V_{out} + V_D}{V_{in(min)} + V_{out} + V_D} \quad (4)$$

With a minimum input voltage ($V_{in(min)}$) of 5 V and a diode voltage (V_D) of 0.7, the maximum duty cycle (D_{max}) is 0.73. So that the value of the inductor L_1 and L_2 is 18 μH .

The peak currents in the inductor ($I_{L1(peak)}$) and inductor 2 ($I_{L2(peak)}$) can be determined by (5) and (6).

$$I_{L1(peak)} = I_{out} \times \frac{V_{out} + V_D}{V_{in(min)}} \times \left(1 + \frac{25\%}{2}\right) \quad (5)$$

$$I_{L2(peak)} = I_{out} \times \left(1 + \frac{25\%}{2}\right) \quad (6)$$

The Peak current in inductors L1 and L2 is 30.8 A and 11.25 A.

• Capacitor Selection

In a Sepic converter, there are coupling capacitors and output capacitors. Determination of the value of the C_C depends on the I_{RMS} and ripple voltage peak to peak capacitor. The I_{RMS} in the C_C called $I_{CC(rms)}$ is given by (7).

$$I_{CC(rms)} = I_{out} \times \sqrt{\frac{V_{out} + V_D}{V_{in(min)}}} \quad (7)$$

The ripple voltage in the coupling capacitor (ΔV_{C_C}) is given by (8).

$$\Delta V_{C_C} = \frac{I_{out} \times D_{max}}{C_C \times f_{SW}} \quad (8)$$

With a capacitor's ripple voltage of 0.5 V, a coupling capacitor's value of 470 F can be determined. Parameters that have been calculated and adjusted to the existing market conditions are shown in Table I.

IV. DISCUSSION AND RESULT

A. Simulation Result

The designed Sepic converter was tested through simulation using PSIM as shown in Fig. 3. The duty cycle is generated by the PWM signal generator. Fig. 4 shows the V_{out} and I_{out} signal of the Sepic converter when it is given an V_{in} of 18 V and D of 60%. The resulting output voltage is 30 V. The V_{out} of the response has a fairly large overshoot.

B. Hardware Experimental Result

A simulated sepic converter is created and tested experimentally in a laboratory. PWM pulses are generated by the Arduino Uno embedded system which will adjust the PWM pulse frequency and duty cycle. The Sepic converter is designed based on the parameters shown in Table I. Fig. 5 shows the experimental setup of the Sepic converter's circuit in the laboratory. IRF 150 is used as a switching component and the input voltage can be adjusted from 10 V – 36 V.

The switching frequency used in this circuit is 31 kHz and The duty cycle can be varied within a certain range of 10% - 90%. The resulting PWM output signal is shown in Fig. 6, while the output voltage of the Sepic converter is shown in Fig. 7.

TABLE I. PARAMETERS OF SEPIC CONVERTER

No.	Parameters	Value
1.	Switching frequency	31 KHz
2.	Diode (D)	20SQ045
3.	Mosfet (S)	IRF150
4.	Inductors (L1)	20 μ H
5.	Inductors (L2)	20 μ H
6.	Coupling Capacitor (Cc)	470 μ F
7.	Output Capacitor (Cout)	4700 μ F

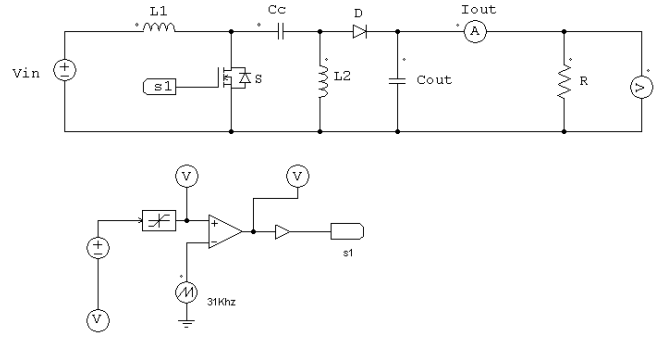


Fig. 3. Simulation of Sepic Converter.

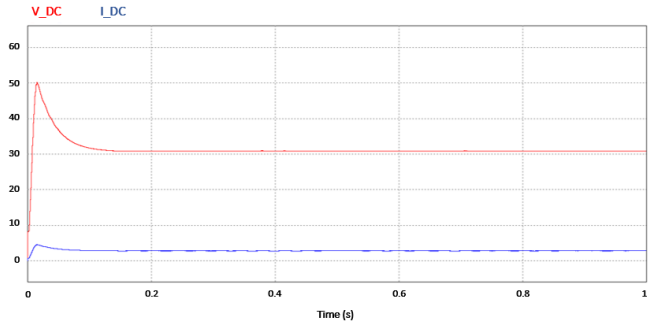
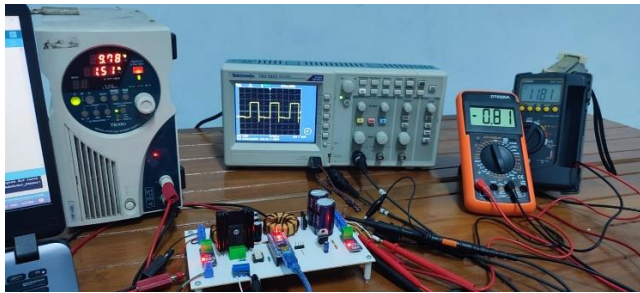


Fig. 4. Current and Voltage Output Signal when V_{in} 18 Volt and Duty Cycle 60%.

At an input voltage of 10 V with a duty cycle of 60% and a resistive load of 14 Ω , the Sepic converter will produce V_{out} of 15.89 V and I_{out} of 1.16 A. To test the circuit's performance, a test is carried out by providing several changes in the duty cycle at a certain input voltage. The values of the inductors and capacitors used are shown in Table I. Fig. 7 shows the output voltages produced experimentally and simulated with changes in the duty cycle at the input voltage of 10 V. The experimental results are close to the simulation output voltage's values. At a duty cycle below 50%, the output voltage is lower than 10 V and at a duty cycle above 50%, it produces a voltage higher than the input voltage. Based on (1), with a duty cycle of 60% and an input voltage of 10 V, it will produce an output voltage of 15 V. The experimental results with an input voltage of 10 V and a duty cycle of 60% produce an output voltage of 15.89 V, while the simulation results produce 16.5 V.



(a)



(b)

Fig. 5. (a) Sepic Converter Circuit, (b) Experimental Setup of Sepic Converter Circuit.



(a)



(b)

Fig. 6. (a) PWM Signal with Duty Cycle 20%, (b) PWM Signal with Duty Cycle 60%.

The sepic converter test is also carried out by providing a change in the input voltage within a range between 10 V to 32 V. Fig. 8 shows the experimental results in the form of changes in the output voltage from the experimental results against the duty cycle for several input voltages. The resulting output voltage for the input voltage variation is in accordance with the plan. The greater the input voltage and the duty cycle, the greater the output voltage.

Fig. 9 displays the experimental results in relation to variations in the Sepic converter's output power and duty cycle. At the input voltage of 32 V, the Sepic converter can produce output power above 100 W. The Sepic converter circuit has worked according to the plan and it can produce an output power of 100 W.



Fig. 7. Sepic Converter Output Voltage.

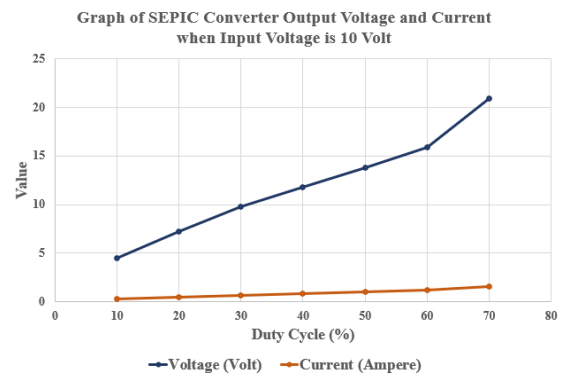


Fig. 8. Change of Output Voltage to Duty Cycle.

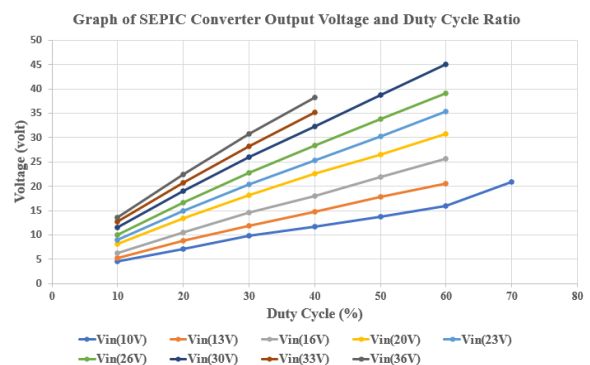


Fig. 9. Results of the Experiment with Various Input Voltages and Changing Output Voltage to Duty Cycle.

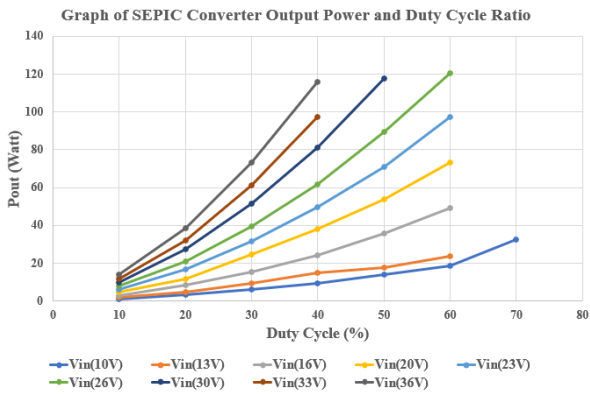


Fig. 10. Experiment Result of Output Power and Duty Cycle.

V. CONCLUSION

The Sepic converter design for applications in renewable energy systems has been described in this article. The determination of component parameters used is based on calculations and values of existing components. The Sepic converter performance testing is done by using simulation and testing in the laboratory for the prototype hardware made. By using PSIM, the Sepic converter is simulated and the hardware prototype is made to be driven by a microcontroller as a PWM generator. The duty cycle given to the switching component determines the Sepic converter's output voltage. If the duty cycle is less than 50%, the output voltage is less than the input voltage; whereas if the duty cycle is more than 50%, the output voltage will be greater than the input voltage. In the hardware prototype, the duty cycle is regulated through the embedded system microcontroller which produces a PWM signal with a switching frequency of 31 kHz. Based on the simulation and experimental results, the Sepic converter works well and can produce the highest output power of 100 W. The resulting voltage depends on the given duty cycle. In future research, control of Sepic converter for renewable energy system will be designed to increase systems efficiency.

ACKNOWLEDGEMENT

The authors would like to thank the Ministry of Education, culture, research and technology, Indonesia and the State Polytechnic of Malang which sponsored this research.

REFERENCES

- [1] Ministry of Energy and Mineral Resources, "Indonesia_Energy_Outlook_2013.pdf." [On line]. Available: <https://www.esdm.go.id>
- [2] Mumtaz F, Yahaya NY, Meraj ST, Singh B, Kannan R, "Review on non-isolated DC-DC Converter and their control techniques for renewable energy applications", *Ain Shams Engineering Journal*, Volume 12, Issue 4, December 2021, Pages 3747-3763.
- [3] Kajiwaru K, Kazuki Tsuji, et.al. "Performance Mechanism of Active Clamp Resonant Sepic Converter in Renewable Energy Systems". 8th International Conference On Renewable Energy Research And Applications. Romanian. 3-6 Nov. 2019.
- [4] Kumar K, Ramesh BN, Prabhu KR "Design and Analysis of an Integrated Cuk-Sepic Converter With MPPT for Standalone Wind/PV Hybrid System". *International Journal of Renewable Energy Research*. Vol. 7. No.1. 2017.
- [5] Arumugam N, Sakthivel A, Devendran D. "Modeling and Simulation of Sepic Converter For Hybrid Energy System". *IOP Conference Series: Materials Science and Engineering* 955. 2020.
- [6] Maroti Kiran P, Padmanaban S, et.al, "New Structure of High Voltage Gain Sepic Converter for Renewable Energy Applications". *IEEE Access*. Vol. 7. June 2019.
- [7] Goyal R & Sharma SK, "Sandwich Topology of Converters for Maximum Power Point Tracking in Hybrid Wind-PV-Wind System", *International Journal of Research Publication and Review*, Vol. 2, Issue 1, 2021, Page 19-31.
- [8] Sivaramakrishnan. M, Marthanda AVG, et al. "Simulation of PV and WECS Using Cuk and Sepic Converter". 2021 5th International Conference on Intelligent Computing and Control Systems (ICICCS), 2021.
- [9] Moradpour R, Ardi H, Tavakoli A. "Design and implementation of a new SEPIC based high step-up DC/DC converter for renewable energy applications". *IEEE Trans Ind Electron* 2017;65(2):1290–7.
- [10] Ardi H, Ajami A. Study on a high voltage gain SEPIC-based DC-DC converter with a continuous input current for sustainable energy applications. *IEEE Trans Power Electron* 2018;33(12):10403–9
- [11] Haghghian SK, Tohidi S, et al. " Design and Analysis of A Novel SEPIC-Based Multi-Input DC/DC Converter. *IET Power Electronics*. Vol 10. Iss.12. pp. 1393-1402. 2017.
- [12] Kumari R, Pandit M, Sherpa KS "Modelling and Comparison of Conventional Sepic Converter With Cascaded Boost-Sepic Converter". *Journal of The Institution Engineers Series B*: 102. PP. 99-109. 2021.

Business and Sociological Perspective Review for Smart Farming Application

Insani Sekar Wangi

Department of Electrical Engineering
Faculty of Engineering
Universitas Indonesia
Kampus Baru UI Depok, Depok, Indonesia
insani.sekar@ui.ac.id

Catur Apriono

Department of Electrical Engineering
Faculty of Engineering
Universitas Indonesia
Kampus Baru UI Depok, Depok, Indonesia
catur@eng.ui.ac.id

Abstract— Digitalization in smart farming is becoming a trend with technological developments such as big data, AI/ML, IoT, and blockchain. Objective transformation in the agricultural sector can increase productivity and create sustainable digital agriculture. Parameters from business and sociological aspects are needed to achieve this purpose. An online intervention is required to improve the farmer's mental health and well-being. The starting point must consider the previously existing business models to prepare the business model for digital transformation, such as user demand and the entire supply chain, including stakeholders. There are three approaches to preparing a business model in digital transformation: internal approach, external, and direct approach. This article presents a systematic review of the business and sociological aspects of the implementation of smart farming by applying the PSALSAR (Protocol, Search, Appraisal, Synthesis, Analysis, Report) review method. This study concludes the scope and applications related to business and sociological perspective review of smart farming classified into smart farming service, infrastructure development, business and technology.

Keywords—smart farming, productivity, transformation

I. INTRODUCTION

Digitalization, the socio-technical process of applying digital innovations, is an increasingly ubiquitous trend. Digitalization comprises phenomena technologies such as big data, the Internet of Things, Augmented Reality, Robotics, sensors, 3D printing, system integration, extreme connectivity, AI/ML, digital twins and blockchain. Digitalization has transformed everyday life and productive processes in agriculture radically. In the agricultural sector, several concepts have emerged to express different forms of digitization in agricultural production systems, such as Smart Farming, Smart Precision, and Decision Agriculture. Regardless of the term used, digitization implies that there are management functions on-farm and out-farm that focus on data types such as location, weather, and energy used to monitor animals, plants, and people. The data is necessary to interpret the history of the past and predict the future to make a more precise and accurate decision [1].

Farming is a dangerous occupation, physically and psychologically. In Australia, the prevalence of mental illness among rural and metropolitan populations is frequently reported. However, farmers' suicide rates also have consistently been higher. What makes agriculture different from other occupations is that a farm is often both

a farmer's workplace and home and is seen as a job and a way of life, earning something from work; the roles of the household and family are related. Farmers also experience stress beyond their control caused by prolonged drought and widespread forest fires that negatively impact their well-being. Farmers are also facing unique and structural barriers to accessing healthiness and mental health [2]. Digital agriculture will likely change production processes inside and outside agriculture and broader social and institutional aspects using digital technology. It is also unknown how knowledge about agriculture can support or provide organizations such as advisory and scientific organizations that can understand and respond to digital agriculture [3].

This paper will discuss the recommended parameters to implement smart farming that focuses on business and sociological aspects to create sustainable digital agriculture.

II. MATERIALS AND METHODS

According to Dawn Craig's lecture material from the Institute of Health & Society at Newcastle University, the systematic review includes two words, namely:

1. Systematic which means doing or serving according to a plan or system that has been planned or methodical
2. Review means a critical appraisal of a book, show, or other work (including a journal or research article)

This study considers a systematic review with the following steps, from now on, abbreviated as PSALSAR:

- Protocol: defines the scope of research
- Search: define a search strategy
- Appraisal: assessing the quality of the papers that have been obtained through the filtering process
- Synthesis: processing and categorizing the information that has been obtained
- Analysis: analyze data that has been categorized
- Report: make a report on the results of the analysis in the form of a table or narration

A. Protocol

The scopes discussed in this review paper are the factors related to the business model, technology, infrastructure readiness, and user readiness in adopting the search strategy.

B. Search

The data used for analysis is from the search results in the ScienceDirect database. The search strategy is to use the

keyword "Smart Farming" combined with the keywords "business" and "sociology". The search time was on May 29, 2022. Table I shows the results of the complete recapitulation of this step.

C. Appraisal

After obtaining related articles, the next step is to evaluate each article. This step is carried out and declared at the beginning as a form of the selection criteria transparency. Table II lists the requirements; inclusion defines the paper decisions taken, and exclusion represents the paper decisions that are not accepted.

D. Synthesis

After successfully filtering the data in the appraisal step, it moves to the synthesis step. At this step, the selected articles will be categorized iteratively and further to be used in the next step. Articles are categorized based on their relevance to business processes and the sociological situation of the farmers.

TABLE I. SEARCH STRING AND ITS RESULTS

Search String	Result
"Smart Farming" AND "Business"	4,256
"Smart Farming" AND "Sociology"	563
"Smart Farming" AND "Business" AND "Sociology"	419

E. Analysis

After the articles are categorized, the next step is analysis. At this stage, the themes that have been previously tagged are deepened. The result of the analysis form of a narrative or a table. The analysis results will be presented narratively in the next section.

TABLE II. APPRAISAL RULE

Criteria	Decision
While there are keywords related to the search string in the title, keywords or abstract	Inclusion
Paper in English or Indonesian	Inclusion
Paper types of the review article and research articles	Inclusion
Paper cannot be access	Exclusion
Duplicated paper	Exclusion
Paper in the year <2017	Exclusion

E Report

After the article analysis, the next step is the report. The results are concluded and used as recommendations for a more comprehensive reader. Information from this research will be described in this article. Conclusions, potentials, and recommendations will be presented at the end.

III. RESULT AND DISCUSSION

From the search results in the ScienceDirect database and using the search string configuration as in table I, the

results obtained are 5,238 articles. The articles that moved to the next step were taken from the combination of the keywords "Smart Farming" AND "Business" AND "Sociology" as many as 419 articles. The appraisal step was done through filtering from the ScienceDirect website, and 170 articles were obtained. Then the abstract, title, keyword, and relevance check steps are carried out manually. The first 20 articles are taken to be classified, analyzed, and reported in the following steps.

TABLE III. FINAL RESULT INCLUSION

No.	Ref.	Summary
1	Klerkx, L., <i>et al.</i> 2019. Netherlands [1]	This paper contributes 17 articles that discuss socio-economic dynamics, digital agriculture, and smart farming
2	Shang, L., <i>et al.</i> 2021. Germany [4]	This paper develops a conceptual framework that incorporates evidence of adoption rates among farmers with a systematic perspective on technology diffusion
3	Musat, G.A., <i>et al.</i> 2018. Romania [5]	This paper presents an intelligent platform that helps farmers manage the greenhouses efficiently and a platform for interacting with other farmers
4	Keshavarz, M. <i>et al.</i> 2021. Iran [6]	This paper discusses a survey of 224 families in Iran who work as farmers to show their level of resilience to climate change
5	Kampker, A. <i>et al.</i> 2019. Germany [7]	This paper presents a morphological framework based on a literature review and expert interviews to develop a product service system business model
6	Clayton, S. <i>et al.</i> 2020. United States [8]	This paper discusses a survey aimed at developing a scale of concern related to climate change
7	Rijswijk, K. <i>et al.</i> 2019. Netherlands [3]	This paper discusses the survey through 29 semi-structured interviews with various parties such as agricultural researchers, advisors, science organizations, and technology providers. The result shows that knowledge and innovation of farming systems should be better to support researchers in agriculture to understand digital and developing digitalization
8	Jerhamre, E. <i>et al.</i> 2022. Sweden [9]	This paper presents a literature review and interview study that discusses the opportunities and obstacles when implementing Artificial Intelligence (AI) in agricultural business
9	Janker, J. <i>et al.</i> 2021. Finland [10]	This paper examines the relationship between farmer well-being and entrepreneurial identification
10	Bagheri, A. <i>et al.</i> 2022. Iran [11]	This paper discusses a study that uses the theory of planned behavior to model the adoption of SWC (Soil and Water Conservation) practices by farmers in the HERIS District in Iran

TABLE III. FINAL RESULT INCLUSION (CONT.)

No.	Ref.	Summary
-----	------	---------

11	Barun, A.T., <i>et al.</i> 2018. Germany [12]	This paper discusses how innovative supply chain management in the industrial era 4.0 provides a way to solve problems and provides a key for developing new forms of work and business models for the Agriculture 4.0 sector.
12	Vaz, E.D., <i>et al.</i> 2020. Germany [13]	This paper provides a solution to increase grain storage capacity in areas of Brazil that don't have adequate storage capacity. A survey was conducted on farmers to identify the impact of attitudes, norms, and perceived behavioral control on farmer's intention to adopt a silo-on farm
13	Oostendorp, R. <i>et al.</i> 2019.[14]	This paper provides a quick overview of the part of financial inclusion as an inherent component and synergy of the inclusive agribusiness model
14	Rodriguez, J.P., <i>et al.</i> 2021. Columbia [15]	This paper implements a Smart Farming System based on 3 layers of architecture (Agriculture Perception, Edge Computing, and Data Analytics).
15	Castillo, G.M.L., <i>et al.</i> 2021. [16]	This paper proposes a socio-psychological model that is built on the Theory of Planned Behavior and social capital variables to examine how psychological construction and its interaction with the environment and farmer's background influence the adoption of irrigation technology
16	Ayre, M. <i>et al.</i> 2019. Australia [17]	This paper shows how to design a process to support expert farmers in adapting digi-ware smart farming practices to their work in providing agricultural consultancy
17	Gerli, P., <i>et al.</i> 2022 [18]	This paper explains how psychological factors such as emotions, attitudes, beliefs, and information seeking influence skill development in the context of smart farming
18	O'Shaughnessy, S.A., <i>et al.</i> 2021 [19]	This paper compares the smart farming approach in the US and Korea in terms of agricultural productivity and technical aspects/social challenges related to agricultural production
19	Adnan, N., <i>et al.</i> 2020.[20]	This paper examines the ability of rice farmers in terms of productivity in Malaysia
20	Gunn, K.M., <i>et al.</i> 2021. Australia [2]	This paper aims to determine farmers' preferences, especially in internet use, in the context of online delivery, mental health, and interventions that focus on well-being.

The classification results revealed that the scope of smart farming services is more concerning to the researchers, with a presentation of 55%. Research related to the adoption of smart farming technology can be seen in the table with a percentage of 30%; this condition shows that the factors that encourage people/farmers to use smart farming are the things researchers study. Then smart farming application in terms of the attitude of the farmers towards the change in the way of working has the same percentage as the business and technology aspects, which is 25%.

TABLE IV. CLASSIFICATION RESULTS TABLE OF SCOPE AND APPLICATION

Scope	Application	References	Total	Percentage (%)
Smart Farming Service	Attitude toward Change	[2], [6], [8], [18], [20]	5	25
	Technology Adoption	[1], [3], [11], [13], [16], [19]	6	30
Infrastructure Development	Platform Creation	[5], [7], [15], [17]	4	20
Business and Technology	Business Development Potential	[4], [9], [10], [12], [14]	5	25

A. Effects of Digitization on Identity, Farmer Skills, and Psychological Aspects

Digitalization in smart farming has an impact on farming methods. The old ways are no longer applied as there is digitization. This condition requires farmers to have different knowledge, skills, and job management [2]. Digital literacy and innovation are also needed for researchers in agriculture, institutional organizations, and advisors/experts to understand and support digitalization in agriculture [8]. The decision-making process for adopting smart farming technology is also supported by the intention and actions taken by farmers. The comprehension related to technology adoption by farmers also leads to the suggestion of incentives related to more targeted policies to accelerate the technology adoption process by farmers in a more inclusive manner [16]. Climate change, human resources entering unproductive age, and environmental problems are challenges for applying smart farming technology [19]. This condition is the right moment to offer farmers online interventions to improve their well-being and mental health. To achieve and cover the maximum coverage, website developers also need to pay attention to diverse internet access and the need for fast resources [2].

B. Smart Farming Business and Infrastructure

Technology in the agricultural sector has evolved over the last few decades, but the shift from smart farming to data-driven agriculture is a significant transition. The application of Artificial Intelligence in agriculture has the potential to optimize and streamline agricultural activities. Data-based decision-making can help farmers increase agricultural yields in quantity and quality. This solution has the effect of reducing carbon emissions, reducing working hours, and increasing profits. For the commercial enterprise sector and government agencies, this transition makes it possible to update supply chain and planning models and improve the agricultural industry at a macro level. Companies, regulatory authorities, and research institutions have an important role in increasing the use of AI in agriculture in the future. From a business perspective, the development of smart farming is no longer a problem but how to solve the challenges and which stakeholders will benefit from this transformation [9]. An association was found between a strong entrepreneurial identity and higher well-being. The design of digital transformation business models in agriculture requires a combination of sustainable economic benefits. The starting point must consider the previously existing business models to prepare the business

model for digital change, such as user demand and the entire supply chain, including stakeholders. From this point of view, three basic approaches can be described, namely:

1. The internal approach defined that products, services, and internal value creation would change. Expansion of product offerings on digital platforms such as online sales of agricultural products or use of technology to reduce costs across each supply chain.
2. The external approach to digitizing agricultural business models involves digital transformation channels, customer relations, and partner collaboration. Improved customer experience is also considered through consumer behavior analysis using various channels such as smartphones and social media.
3. The direct approach defined that the two paths are carried out in parallel. This business model is digitally transformed in all aspects

Collaboration using the new ways along the agricultural supply chain allows the development of synergies and symbiotic effects between stakeholders. It creates a competitive advantage for all partners involved [12].

IV. CONCLUSIONS

From this research, various factors influence the adoption of smart farming technology. There are challenges to applying smart farming technology such as climate change, human resources entering an unproductive age, and environmental problems, especially climate change. It is the right momentum to offer online interventions to improve farmers' well-being and mental health. Farmers also need various aspects, especially digital literacy related to the implementation of smart farming, so that they can propose more targeted policies. From a business perspective, the development of smart farming is no longer become a problem. Still, how to solve the challenges and which stakeholders will benefit from this transformation. The starting point must consider the previously existing business models to prepare the business model for digital change, such as user demand and the entire supply chain, including stakeholders. From this point of view, three basic approaches can be described: internal, external, and direct. Collaboration using the new ways along the agricultural supply chain allows the development of synergies and symbiotic effects between stakeholders. It may create a competitive advantage for all partners involved.

ACKNOWLEDGEMENT

Universitas Indonesia supports this research through International Indexed Publication (PUTI) Q1 Grant, the year 2022, number: NKB-501/UN2.RST/HKP.05.00/2022

REFERENCES

- [1] Klerkx, L., Jakku, E., & Labarthe, P. (2019). A review of social science on digital agriculture, smart farming and agriculture 4.0: New contributions and a future research agenda. *NJAS - Wageningen Journal of Life Sciences*, 90–91(October), 100315. <https://doi.org/10.1016/j.njas.2019.100315>
- [2] Gunn, K. M., Barrett, A., Hughes-Barton, D., Turnbull, D., Short, C. E., Brumby, S., Skaczkowski, G., & Dollman, J. (2021). What farmers want from mental health and well-being-focused websites and online interventions. *Journal of Rural Studies*, 86(September 2020), 298–308. <https://doi.org/10.1016/j.jrurstud.2021.06.016>
- [3] Rijswijk, K., Klerkx, L., & Turner, J. A. (2019). Digitalisation in the New Zealand Agricultural Knowledge and Innovation System: Initial understandings and emerging organisational responses to digital agriculture. *NJAS - Wageningen Journal of Life Sciences*, 90–91(October), 100313. <https://doi.org/10.1016/j.njas.2019.100313>
- [4] Shang, L., Heckelei, T., Gerullis, M. K., Börner, J., & Rasch, S. (2021). Adoption and diffusion of digital farming technologies - integrating farm-level evidence and system interaction. *Agricultural Systems*, 190. <https://doi.org/10.1016/j.agry.2021.103074>
- [5] Musat, G. A., Colezea, M., Pop, F., Negru, C., Mocanu, M., Esposito, C., & Castiglione, A. (2018). Advanced services for efficient management of smart farms. *Journal of Parallel and Distributed Computing*, 116, 3–17. <https://doi.org/10.1016/j.jpdc.2017.10.017>
- [6] Keshavarz, M., & Moqadas, R. S. (2021). Assessing rural households' resilience and adaptation strategies to climate variability and change. *Journal of Arid Environments*, 184 (July 2020), 104323. <https://doi.org/10.1016/j.jaridenv.2020.104323>
- [7] Kampker, A., Stich, V., Jussen, P., Moser, B., & Kuntz, J. (2019). Business models for industrial smart services - the example of a digital twin for a product-service-system for potato harvesting. *Procedia CIRP*, 83, 534–540. <https://doi.org/10.1016/j.procir.2019.04.114>
- [8] Clayton, S., & Karazsia, B. T. (2020). Development and Validation of a measure of climate change anxiety. *Journal of Environmental Psychology*, 69 (October 2019), 101434. <https://doi.org/10.1016/j.jenvp.2020.101434>
- [9] Jerhamre, E., Carlberg, C. J. C., & van Zoest, V. (2022). Exploring the susceptibility of smart farming: Identified opportunities and challenges. *Smart Agricultural Technology*, 2 (August 2021), 100026. <https://doi.org/10.1016/j.atech.2021.100026>
- [10] Janker, J., Vesala, H. T., & Vesala, K. M. (2021). Exploring the link between farmers' entrepreneurial identities and work well-being. *Journal of Rural Studies*, 83 (March), 117–126. <https://doi.org/10.1016/j.jrurstud.2021.02.014>
- [11] Bagheri, A., & Teymouri, A. (2022). Farmers' intended and actual adoption of soil and water conservation practices. *Agricultural Water Management*, 259 (October 2021), 107244. <https://doi.org/10.1016/j.agwat.2021.107244>
- [12] Braun, A. T., Colangelo, E., & Steckel, T. (2018). Farming in the Era of Industrie 4.0. *Procedia CIRP*, 72, 979–984. <https://doi.org/10.1016/j.procir.2018.03.176>
- [13] Vaz, E. D., Gimenes, R. M. T., & Borges, J. A. R. (2020). Identifying socio-psychological constructs and beliefs underlying farmers' intention to adopt on-farm silos. *NJAS - Wageningen Journal of Life Sciences*, 92 (February), 100322. <https://doi.org/10.1016/j.njas.2020.100322>
- [14] Oostendorp, R., van Asseldonk, M., Gathiaka, J., Mulwa, R., Radeny, M., Recha, J., Wattel, C., & van Wessenbeek, L. (2019). Inclusive agribusiness under climate change: a brief review of the role of finance. *Current Opinion in Environmental Sustainability*, 41 (May), 18–22. <https://doi.org/10.1016/j.cosust.2019.09.014>
- [15] Rodríguez, J. P., Montoya-Munoz, A. I., Rodríguez-Pabon, C., Hoyos, J., & Corrales, J. C. (2021). IoT-Agro: A smart farming system to Colombian coffee farms. *Computers and Electronics in Agriculture*, 190 (October), 106442. <https://doi.org/10.1016/j.compag.2021.106442>
- [16] Castillo, G. M. L., Engler, A., & Wollni, M. (2021). Planned behavior and social capital: Understanding farmers' behavior toward pressurized irrigation technologies. *Agricultural Water Management*, 243 (September 2020), 106524. <https://doi.org/10.1016/j.agwat.2020.106524>
- [17] Ayre, M., Mc Collum, V., Waters, W., Samson, P., Curro, A., Nettle, R., Paschen, J. A., King, B., & Reichelt, N. (2019). Supporting and practising digital innovation with advisers in smart farming. *NJAS - Wageningen Journal of Life Sciences*, 90–91(November 2018), 100302. <https://doi.org/10.1016/j.njas.2019.05.001>
- [18] Gerli, P., Clement, J., Esposito, G., Mora, L., & Crutzen, N. (2022). Technological Forecasting & Social Change The hidden power of emotions: How psychological factors influence skill development in smart technology adoption. *Technological Forecasting & Social Change*, 180 (November 2021), 121721. <https://doi.org/10.1016/j.techfore.2022.121721>
- [19] O'Shaughnessy, S. A., Kim, M., Lee, S., Kim, Y., Kim, H., & Shekailo, J. (2021). Towards smart farming solutions in the US and South Korea: A comparison of the current status. *Geography and*

Sustainability, 2(4), 312–327.
<https://doi.org/10.1016/j.geosus.2021.12.002>
[20] Adnan, N., Nordin, S. M., & Anwar, A. (2020). Transition pathways for Malaysian paddy farmers to sustainable agricultural practices: An

integrated exhibiting tactics to adopt Green fertilizer. Land Use Policy, 90 (May 2019), 104255.
<https://doi.org/10.1016/j.landusepol.2019.104255>

Clustering of the 2018 Lombok Earthquakes using an Agglomerative Hierarchical Clustering Algorithm

Cipta Ramadhani
Dept. of Electrical Engineering
University of Mataram
Mataram, Indonesia
cipta.ramadhani@unram.ac.id

Rosmaliati
Dept. of Electrical Engineering
University of Mataram
Mataram, Indonesia
rosmaliati@unram.ac.id

Abdullah Zainuddin
Dept. of Electrical Engineering
University of Mataram
Mataram, Indonesia
abdullahzain@unram.ac.id

Teti Zubaidah
Dept. of Electrical Engineering
University of Mataram
Mataram, Indonesia
tetizubaidah@unram.ac.id

Abdul Natsir
Dept. of Electrical Engineering
University of Mataram
Mataram, Indonesia
natsir.amin@unram.ac.id

Abstract—Lombok Island is located between the Indo-Australian subduction zone and the Flores back-arc thrust, makes it vulnerable to earthquake. During July to August 2018, significant earthquakes occurred in Lombok Island region and led to severe damages in the northern area. In this study, we propose hierarchical clustering of historical earthquakes that occurred in Lombok region during July 2018 to December 2018 and model the clustering of earthquakes. We used spatial and non-spatial attributes in three different conditions. The results show that the most homogenous seismic sources were achieved by using spatial attributes.

Keywords—earthquakes, clustering, agglomerative, spatial attributes

I. INTRODUCTION

Lombok is an island, located in West Nusa Tenggara province, Indonesia. It is a part of the Lesser Sunda Island region, lies between Bali island in the West and Sumbawa island in the East. In 2018, Indonesian Meteorology, Climatology and Geophysical Agency (Badan Meteorologi Klimatologi dan Geofisika/BMKG) reported that several significant earthquakes shook Lombok [1]. This earthquake sequence began with an Mw 6.4 earthquake on 28 July 2018, followed by earthquakes on 5 August (Mw 6.8), 9 August (Mw 5.8) and 19 August (Mw 6.9). The detailed parameters of earthquakes are listed in Table I, and locations of earthquakes are depicted in Fig. 1. The earthquakes that occurred from 5 to 19 August 2018 in the West-, East-, and North Lombok reached the maximum intensity of VIII-IX and were strongly felt by all residents in the whole of Lombok [2].

The Seismicity of Lombok island mainly controlled by two major geological structures, i.e. the Flores back-arc thrust in the North and the Indo-Australian subduction zone to the South [3], [4]. A unique feature of geomagnetic anomaly pattern in Lombok consists of contiguous negative–positive anomalies are closely related to this subduction. A strong dipolar magnetic anomaly was found in the southern region of Lombok could be associated with a large magnetic body or a discontinuity in the geological structure (e.g. potentially local fault) [5]. Another stronger one was found in the northern region, which was formerly identified as formations of young lavas of Mount Rinjani, but later on it

could also be identified related with a new mature subduction along the Flores thrust [6].

Earthquakes and effort to reduce the hazard have attracted the attention of many researchers. Mitigation plans of seismic hazard and risk play an important role particularly for decision makers to prepare an earthquake mitigation in an optimal way [7], [8]. One of step in any seismic hazard analysis is the ability of modeling the earthquake source [9], [10]. A potential single earthquake that occurred in one place is supposed to be uniform. The chance of one earthquake to be occurred with certain magnitude is the same through the source, which may be linear or areal [10].



Fig. 1. The relatives Location of The 2018 Lombok Earthquakes.

TABLE I. PARAMETER FOR THE MAINSHOCKS OF LOMBOK 2018 EARTHQUAKES

Date	Time (UTC)	Latitude (°N)	Longitude (°E)	Magnitude (Mw)	Depth (km)
July 28 th	22:47:38.491	8.35	116.50	6.4	13
August 5 th	11:46:37.363	8.35	116.47	6.8	32
August 9 th	05:25:32.601	8.44	116.21	5.8	14
August 19 th	14:56:27.086	8.37	116.70	6.9	18

Modeling of earthquake sources is a fundamental in creating hazard maps and estimating the probability of upcoming earthquake that will be occurred with different magnitude in the future [11]. Using database collection of historical earthquakes has made it possible to compose these sources more efficient. However, seismologists construct the boundary of seismic sources manually based on tectonic features and historical earthquakes without using standard method [12]-[14]. Furthermore, since the size of historical earthquake grows, the manual depiction of source boundaries becomes less accurate and complicated.

Several studies have been conducted to cluster earthquakes sources. A study for earthquake preparedness in the Istanbul city has used K-means clustering method to create the training dataset for earthquakes vulnerability analysis [15]. Another study in the Sea of Marmara region has used high-resolution seismicity catalog and the nearest-neighbor earthquake cluster approach for identification of clusters seismicity [16]. Using this method, they could identified whether the events of earthquake are foreshocks, mainshocks and aftershocks. More recent study has been conducted in the area of Corinth Gulf, Greece to identify evolution of mainshock–aftershock sequences and swarms, along with periods of seismic quiescence using Markovian Arrival Process (MAP) [17]. The study could identify selected seismic sequences and the hidden states and found their close relationships with mainshock–aftershock and swarm-like sequences.

Agglomerative Hierarchical Clustering (AHC) algorithm has been proposed to overcome clustering problem. Authors [18] proposed AHC algorithm to cluster Linear Ordinal Ranking (LOR) information and used it to illustrate online financial product recommendation. Distance measure and the aggregation method have been proposed under the framework of AHC. Meanwhile authors [19] used AHC as a data mining procedure to provide a simplified optimization of economic, environmental and energy (3E) in assessing of building retrofit on a macro-scale. Based on set performance target, an innovative framework for a facile and holistic assessment can be offered to investors with a broader range of retrofit alternatives.

AHC has been applied also in the power transmission network investment [20]. Demand patterns are extracted from hourly demand data based on the Elbow’s rule and a linkage criterion. Three different categories (i.e. seasonal, monthly, and weekly) are used to test the representative demand curves, thereby a 24 hours demand pattern can be provided.

II. DATA AND METHOD

The work of this paper is focused to generate clusters of earthquakes based on seismic sources from historical earthquakes. In order to achieve this task, we used an agglomerative clustering algorithm to generate clustering of the 2018 earthquakes in Lombok Island. We interpreted that AHC algorithm can cluster the earthquake without predetermined the number of clustering as an input parameter.

Spatial (latitude and longitude) and non-spatial attributes (depth, magnitude, and occurrence date) are used in this work. Table II shows the description of each attribute used in the dataset.

TABLE II. AVAILABLE ATTRIBUTES FOR EARTHQUAKES.

Variable	Description
Latitude	Decimal degrees Latitude
Longitude	Decimal degrees Longitude
Depth	Depth of the earthquake in kilometers.
Magnitude	The magnitude for the event
DOY	Day of years

A. Data

Earthquake data with magnitude from M_w 1.7 to M_w 6.9 in Lombok Island from July to December 2018 were collected from the official BMKG website for earthquake repository (<http://repogempa.bmkg.go.id/>). The Data set contains 1400 earthquakes.

The occurrence day of earthquake is used based on Day of Years which means that we count the day from 1 to 365 days in one year.

B. Method

Hierarchical clustering algorithm can be either divisive or agglomerative. In this case, the AHC algorithm does not require us to predetermine the number of clusters. Bottom-up algorithms initially consider each piece of data as a singleton cluster before subsequently combining pairs of clusters into a single cluster that contains all the data.

Hierarchical clustering creates a (usually binary) tree through the data. The leaves are individual data objects, but the root is a single cluster that contains all of the data. Individual pieces of data make up the leaves, but the root is a single cluster that contains all of the data. Intermediate clusters that contain parts of the data are placed between the root and the leaves. The main goal of hierarchical clustering is to build upward-moving "clusters of clusters." To make a tree, there are primarily two conceptual methods. AHC merges groups together from the bottom up, starting with each datum in its own singleton cluster. Divisive clustering begins with all of the data in a single large group and then separates it into singletons for each piece of data. In this paper, we consider to use AHC as our method.

Fig. 2 represents the AHC technique. The clusters with just one element are labeled as leaves. The internal nodes depict the division of parent node (division), or the union of their two children (agglomeration). The root is a single cluster that contains the entire element in the collection. The AHC in agglomerative clustering is defined by a hierarchy structure for the data, which are usually deterministic. The advantage of hierarchical clustering is that the number of clusters is not required as an input variable. In comparison with partitional algorithm, it provides more detail information than using the unorganized set.

In order to cluster the earthquake sources, we used three different approaches:

- Clustering based on spatial variables.

In this approach, we clustered the earthquakes based on their location (latitude and longitude). Because the distance of both variables is compatible and compensate each other, the variables do not need to be normalized for this clustering.

- Clustering based on non-spatial variables.

In non-spatial variables, the earthquakes are grouped based on occurrence date, magnitude and depth. We hypothesize that the earthquakes which a similar depth, magnitude and occurrence date are likely to be related to the same cluster. Because the range of occurrence date is larger than the range of both depth and magnitude so that all non-spatial data is normalized to ensure that data is similar across all records.

- Clustering based on all variables.

For the last clustering approach, we used all variable (latitude, longitude, depth, magnitude, and occurrence date) to see their dependency to cluster the earthquakes.

In order to create a cluster among the earthquake sources, first we measured the distance between the earthquakes using the Euclidean technique. This technique is used to calculate the distance between two objects. Euclidean distance is determined between both the center of the source object and the centers of all surrounding objects. The Euclidean distance can be computed using (1).

$$D(x, y) = \sqrt{(x_1 - y_1)^2 + (x_2 - y_2)^2 + \dots + (x_n - y_n)^2} \quad (1)$$

where:

- $D(x, y)$: The distance between the earthquake x and y
- x_n : number variable from the earthquake x
- y_n : number variable from the earthquake y

Next step, we used agglomerative clustering with ward's method with pandas and Sklearn library in Python programming. The goal of Ward's Method is to reduce variance within a single cluster of objects. Errors Sum of square (ESS) between the two clusters is used to calculate the distance between the two clusters created using Ward's approach. Only when there are multiple element objects in the cluster can Ward's be determined [21]. The Ward's method of agglomerative clustering algorithm can be measured using (2).

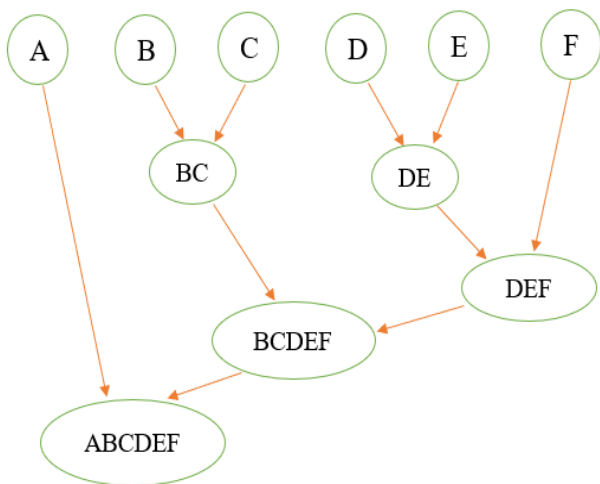


Fig. 2. Agglomerative Hierarchical Clustering Technique.

$$ESS = \sum_{j=1}^P \left(\sum_{i=1}^n X_{ij}^2 - \left(\frac{1}{n} \sum_{i=1}^n X_{ij} \right)^2 \right) \quad (2)$$

where:

- X_{ij} : value for the object to-i in the cluster to-j
- P : number of parameter calculated
- N : the number of objects made into the the cluster

The goal of Ward's Method is to select the subsequent clustering steps with the least amount of ESS increase possible. The sum of the squares in the two clusters for each variable is the distance between the two clusters. This strategy uses a variance analysis approach to determine the distance between clusters [22].

III. RESULT AND DISCUSSION

In this section, we present the results of earthquakes clustering that occurred in Lombok Island from July to December 2018 using agglomerative Hierarchy algorithm. As mentioned in the previous section, the result will be presented in three different approaches. First, we cluster the earthquakes based on spatial variables. The second clustered is modeled based on non-spatial variables. The last model, we used all variable to see their dependences in clustering model.

Fig. 3 represents the size of cluster based on spatial attribute. Meanwhile, Fig. 4 and Fig. 5 represent the size of cluster based on non-spatial attribute and all variable in our dataset, respectively. Based on observation, earthquakes that occurred in Lombok Island are distributed uniformly in a few clusters when spatial attribute are used as variables. Although, in terms of depth, magnitude and occurrence date, the earthquakes are mostly in two classes and one small class.

By referring to Fig. 3, it was found that the earthquakes are clustered around three homogenous seismic sources ranging from 448 to 497 numbers of earthquakes. This result is in-line with three significant earthquakes that shook the Lombok island in 2018. On the other hand, both Fig. 4 and Fig. 5 are opposite. In Fig. 4, the sizes of each clustering value are 162, 639, and 616, respectively. Furthermore in Fig. 5, the clustering pattern is similar; with size of the three clustering models are of 166, 676, and 575, respectively. Based on these results, we interpret that clustering might work only on spatial attributes rather than non-spatial attributes.

Fig. 6 shows the number of clustering that are colored based on spatial attribute (longitude and latitude). In Fig. 7, the number of clustering is depicted based on non-spatial attribute (depth, magnitude, and occurrence date). Meanwhile, Fig. 8 depicts the number of clusters based on all attributes that were already mentioned in the previous section. All of these figures depict earthquakes that occurred at least 1400 times on Lombok island from June to December 2018.

When earthquakes are clustered according to spatial attributes (see Fig. 6), the geographical distribution of clusters seems uniform and their geographic distribution appears uniform and follow the pattern of mainshocks (see Table I). In other words, each cluster is located near by the

three significant earthquakes that shook Lombok Island in 2018. This cluster gave similar result which was conducted by [23]. On the other hand, when earthquakes are clustered according to non-spatial attributes (see Fig. 7), their geographic location grouping appears random and does not correspond to the locations of main earthquakes. It means that the earthquakes of one cluster potentially occur in different parts of the region. In the last approach, when both non-spatial and spatial attributes of earthquakes are considered as clustering process (see Fig. 8), these additional attributes does not affect the geographical distribution of clusters. In other words, non-spatial attributes seem not be appropriate for use as attributes for the clustering process.

IV. CONCLUSION

This research clustered earthquakes based on spatial and non-spatial attributes that occurred in Lombok Island from July to December 2018. The clustering pattern can be seen when the earthquakes are clustered based on their location. Three clustering patterns of earthquakes represented three significant earthquakes that shook Lombok Island in 2018. However, the result of clustering pattern using non-spatial attributes is opposite. The distribution of clustering in certain locations seems random and does not follow the pattern of the significant earthquakes. This observation implies that clustering earthquakes is feasible only for spatial attributes rather than non-spatial attributes. However, this hypothesis needs further investigation and is a subject for future research.



Fig. 3. The Size of cluster based on spatial variables.

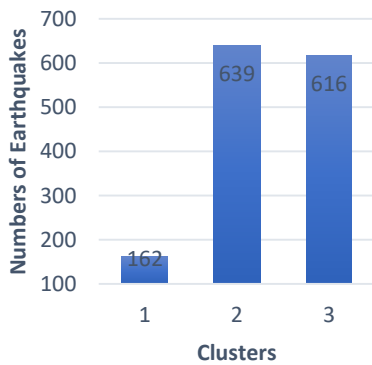


Fig. 4. The Size of cluster based on non-spatial variables.

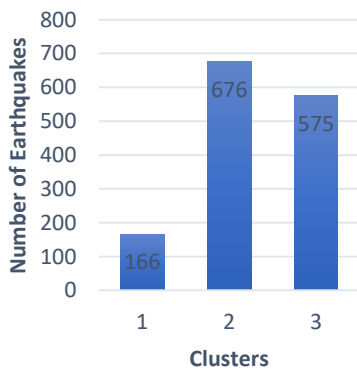


Fig. 5. The Size of cluster based on all variables.

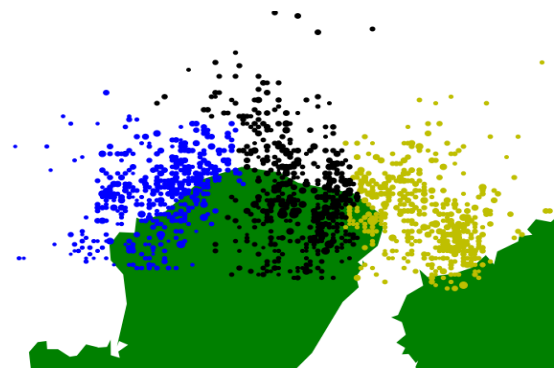


Fig. 6. Earthquakes clustering based on spatial attributes

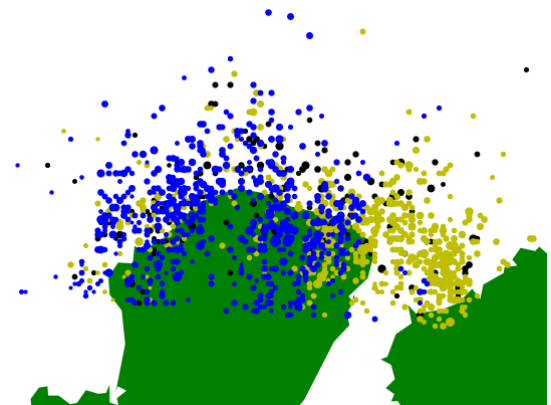


Fig. 7. Earthquakes clustering based on non-spatial attributes

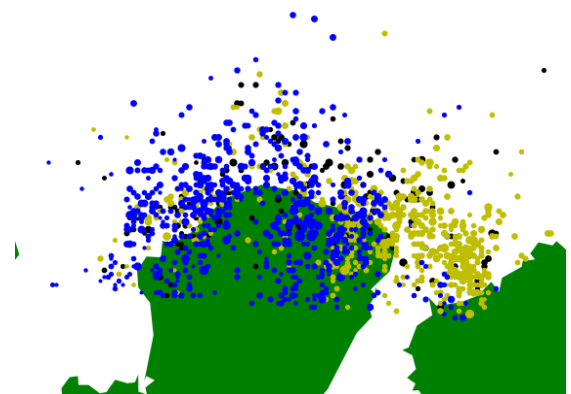


Fig. 8. Earthquakes clustering based on spatial and non-spatial attributes

ACKNOWLEDGMENT

This research is funded by Universitas Mataram under Hibah Dana PNBP 2022 program entitled “Pengelompokan (Clustering) Kejadian Gempa Pulau Lombok Zona Backarc Thrust untuk Mitigasi Bencana”. The data that has been presented in this paper is collected from Indonesian Meteorology, Climatology, and Geophysical Agency (BMKG). Our appreciation is presented to BMKG as their effort to promote high standard earthquakes repository (<http://repogempa.bmkg.go.id/>).

REFERENCES

- [1] U. Sutiyono et al., Katalog Gempa Bumi Signifikan dan Merusak Tahun 1821–2018. Jakarta: Pusat Gempa Bumi dan Tsunami Kedeputian Bidang Geofisika Badan Meteorologi Klimatologi dan Geofisika, 2019.
- [2] R. Robiana, A. Minarno, S. Hidayati, S. Supartoyo, and F. Nurfalah, *Gempa Lombok Tanggal 29 Juli 2018 dan Dampaknya*. Kajian Rangkaian Gempa Lombok Provinsi Nusa Tenggara Barat, Pusat Penelitian dan Pengembangan Perumahan dan Pemukiman, Badan Penelitian dan Pengembangan, Kementerian Pekerjaan Umum dan Perumahan Rakyat, 2018.
- [3] W. Hamilton, “Subduction in the Indonesian region,” 1977, pp. 15–31. doi: 10.1029/ME001p0015.
- [4] W. B. Hamilton, “Tectonics of the Indonesian region,” Washington, D.C., 1979.
- [5] T. Zubaidah, M. Korte, M. Manda, Y. Quesnel, B. Kanata, “Geomagnetic field anomalies over the Lombok Island region: an attempt to understand the local tectonic changes,” *Int. J. Earth Sci.*, Vol. 99, pp. 1123–1132, July 2010, doi: 10.1007/s00531-009-0450-4.
- [6] T. Zubaidah, M. Korte, M. Manda, M. Hamoudi, “New insights into regional tectonics of the Sunda-Banda Arcs region from integrated magnetic and gravity modelling,” *J. Asian Earth Sci.*, Vol. 80, pp. 172–184, 2014. <http://dx.doi.org/10.1016/j.jseae.2013.11.013>.
- [7] C. H. Scholz, “Large Earthquake Triggering, Clustering, and the Synchronization of Faults,” *Bulletin of the Seismological Society of America*, vol. 100, no. 3, pp. 901–909, Jun. 2010, doi: 10.1785/0120090309.
- [8] J. G. Anderson and K. Nanjo, “Distribution of Earthquake Cluster Sizes in the Western United States and in Japan,” *Bulletin of the Seismological Society of America*, vol. 103, no. 1, pp. 412–423, Feb. 2013, doi: 10.1785/0120100212.
- [9] C. A. Cornell, “Engineering seismic risk analysis,” *Bulletin of the Seismological Society of America*, vol. 58, no. 5, pp. 1583–1606, Oct. 1968, doi: 10.1785/BSSA0580051583.
- [10] Reiter, L., *Earthquake hazard analysis: issues and insights*. New York: Columbia University Press, 1990.
- [11] T. Anagnos and A. S. Kiremidjian, “A review of earthquake occurrence models for seismic hazard analysis,” *Probabilistic Engineering Mechanics*, vol. 3, no. 1, pp. 3–11, Mar. 1988, doi: 10.1016/0266-8920(88)90002-1.
- [12] M. Hashemi, A. A. Alesheikh, and M. R. Zolfaghari, “A spatio-temporal model for probabilistic seismic hazard zonation of Tehran,” *Comput Geosci*, vol. 58, pp. 8–18, Aug. 2013, doi: 10.1016/j.cageo.2013.04.005.
- [13] M. Erdik, Y. A. Biro, T. Onur, K. Sesetyan, and G. Birgoren, “Assessment of earthquake hazard in Turkey and neighboring,” *Annals of Geophysics*, vol. 42, no. 6, Dec. 1999, doi: 10.4401/ag-3773.
- [14] M. Erdik, M. Demircioglu, K. Sesetyan, E. Durukal, and B. Siyahi, “Earthquake hazard in Marmara Region, Turkey,” *Soil Dynamics and Earthquake Engineering*, vol. 24, no. 8, pp. 605–631, Sep. 2004, doi: 10.1016/j.soildyn.2004.04.003.
- [15] M. Shafapourtehrany, P. Yariyan, H. Özener, B. Pradhan, and F. Shabani, “Evaluating the application of K-mean clustering in Earthquake vulnerability mapping of Istanbul, Turkey,” *International Journal of Disaster Risk Reduction*, vol. 79, p. 103154, Sep. 2022, doi: 10.1016/j.ijdr.2022.103154.
- [16] P. Martínez-Garzón, Y. Ben-Zion, I. Zaliapin, and M. Bohnhoff, “Seismic clustering in the Sea of Marmara: Implications for monitoring earthquake processes,” *Tectonophysics*, vol. 768, p. 228176, Oct. 2019, doi: 10.1016/j.tecto.2019.228176.
- [17] P. Bountzias, E. Papadimitriou, and G. Tsaklidis, “Earthquake clusters identification through a Markovian Arrival Process (MAP): Application in Corinth Gulf (Greece),” *Physica A: Statistical Mechanics and its Applications*, vol. 545, p. 123655, May 2020, doi: 10.1016/j.physa.2019.123655.
- [18] N. Liu, Z. Xu, X.-J. Zeng, and P. Ren, “An agglomerative hierarchical clustering algorithm for linear ordinal rankings,” *Inf Sci (N Y)*, vol. 557, pp. 170–193, May 2021, doi: 10.1016/j.ins.2020.12.056.
- [19] Y. Hong, C. I. Ezech, H. Zhao, W. Deng, S.-H. Hong, and Y. Tang, “A target-driven decision-making multi-layered approach for optimal building retrofits via agglomerative hierarchical clustering: A case study in China,” *Build Environ*, vol. 197, p. 107849, Jun. 2021, doi: 10.1016/j.buildenv.2021.107849.
- [20] N. González-Cabrera, J. Ortiz-Bejar, A. Zamora-Mendez, and M. R. Arrieta Paternina, “On the Improvement of representative demand curves via a hierarchical agglomerative clustering for power transmission network investment,” *Energy*, vol. 222, p. 119989, May 2021, doi: 10.1016/j.energy.2021.119989.
- [21] A. N. Fathia, R. Rahmawati, and T. Tarmo, “Analisis Klaster Kecamatan Di Kabupaten Semarang Berdasarkan Potensi Desa Menggunakan Metode Ward Dan Single Linkage,” *Jurnal Gaussian*, vol. 5, no. 4, pp. 801–810, Oct. 2016.
- [22] C. Suhaeni, A. Kurnia, and R. Ristiyanti, “Perbandingan Hasil Pengelompokan menggunakan Analisis Cluster Berhierarchy, K-Means Cluster, dan Cluster Ensemble (Studi Kasus Data Indikator Pelayanan Kesehatan Ibu Hamil),” *JURNAL MEDIA INFOTAMA*, vol. 14, no. 1, Feb. 2018, doi: 10.37676/jmi.v14i1.469.
- [23] A. T. Sasmi et al., “Hypocenter and Magnitude Analysis of Aftershocks of the 2018 Lombok, Indonesia, Earthquakes Using Local Seismographic Networks,” *Seismological Research Letters*, vol. 91, no. 4, pp. 2152–2162, Jul. 2020, doi: 10.1785/0220190348.

Calcium Carbonate Scale Inhibition Program on Two-Phase Geothermal Well in Indonesia

Nur Choiri Amin
Regional Manager
SOLENIS NEU Kimya A.Ş.
Jakarta, Indonesia
nchoiriamin@solenis.com

Kuzey Karasu
Sales and Operation Director
SOLENIS NEU Kimya A.Ş.
Istanbul, Turkey
kkarasu@solenis.com

Abdurrahman Ünal
Technical Manager
SOLENIS NEU Kimya A.Ş.
Istanbul, Turkey
aunal@solenis.com

Y. Tuğçe Yüksel
R&D Executive
SOLENIS NEU Kimya A.Ş.
Istanbul, Turkey
ytugceyuksel@solenis.com

Abstract—The formation of calcium carbonate (calcite) is a major scaling problem that occurs in geothermal wells around the world, leading to a quick decline in well output, reduced power plant production, increased maintenance frequency and operating costs. More than 80% of geothermal operation has calcium carbonate scale. Several methods can be used to prevent calcite scale and to rehabilitate affected production wells. At the Solenis (previously known as NEUCHEMIE a Solenis company) customer's geothermal field, the scale prevention program was conducted by continuous online injection of the NEU GUARD PW920 scale dispersant until it reached the total well depth. The scale dispersant was injected through capillary tubing with a special dosing pump using a method called downhole scale inhibition (DSI). During the project trial period, we took water samples and analyzed several minerals' parameters to detect the extent of the effect of the scale dispersant injection through the capillary tubing. Using the data from the plant trial, the water analyses, and the scale coupon monitoring program, we determined that an optimum dosage of scale dispersant is 8 ppm. Throughout the implementation process, the total removed calcium was 479 kg/day or, stated another way, over an approximately 3-months (84-day) period as much as 40.24 tons of potential calcite was removed from the well.

Keywords—Calcite, Calcium Carbonate scale, Downhole Scale Inhibition, Scale Prevention, Scale Inhibition, Chemical Treatment, Two-Phase Geothermal Well, Indonesian Geothermal

I. INTRODUCTION

Calcite can be formed because of hydrolysis, boiling of geothermal fluids, and heating of colder environmental geothermal fluids. In a boiling environment, layered calcite precipitates in open areas upon loss of carbon dioxide, mostly with pH-controlling carbonate species [1].

Calcium carbonate scales (in the crystalline forms of calcite or aragonite) are common in wells with reservoir temperatures of 140–240 °C and are primarily found at the depth where the water starts to boil in the well [2].

According to the research, calcite incrustation is quite common in the range of 140–280 °C. For example, the Ribeira Grande geothermal field, with an estimated temperature of 235–245 °C, is in this category. In these types of reservoirs, geothermal fluids are often saturated

with calcite and become saturated inside the wells. After boiling and flashing to lower temperatures, the aqueous Carbon dioxide is reduced as it turns into the gas phase. Therefore, the Carbon dioxide leaving as gas phase increases the pH and carbonate concentration of the water phase. Thus, the increase in calcite concentration results in a transition of the calcite solubility phase from a saturated to a supersaturated state and causes precipitation [3].

The chemical composition of the geothermal fluid has a significant effect on the formation of calcite deposits in boreholes. Chemical inhibition is the best option to avoid the expensive work-overs associated with reaming or chemically cleaning of wells and out of service periods [3].

One of the most common techniques for controlling carbonate scaling involves the use of chemical additives (crystal growth or scale inhibitors, anti scalant). These substances are usually moderately large molecules that are readily adsorbed on the growth-active sites of the crystal surfaces, thus retarding nucleation and crystal growth, and distorting the crystal structure of the scale. The various inhibitors are considered to act according to one (and usually more than one) of the following main mechanisms of interference with crystal growth:

1. *Threshold effect*: the inhibitor acts by retarding salt precipitation.
2. *Crystal distortion effect*: the inhibitor interferes with crystal growth by producing an irregular structure (usually rounded surfaces) with poor scaling potential.
3. *Dispersion*: inducing a charge on the crystal surface results in the repulsion between neighboring crystals.
4. *Sequestration or chelation*: the binding with certain cations (Fe, Mg, etc.) to form soluble complexes [4].

Fig. 1 shows the main scale inhibition system that is used for chemical injection in the wells. This system's equipment includes a metering pump for continuous injection of a low-dose scale dispersant (up to 59 bar); a lubricator set, consisting of a 5-meter, 3-inch steel pipe with a stuffing box mounted on the top and a ram BOP

(blowout preventer valve) connected on the bottom. Lubricant allows the installation of the downhole equipment in the well under pressure. Downhole equipment consists of an inhibitor injection chamber (high pressure valve) and a sinker rod. Nickel–iron–chrome capillary tubing is used (0.25 in outer diameter (OD)) to transport the inhibitor from the surface to the downhole equipment [3].

Calcite inhibition performance is monitored by several useful chemical and physical parameters, of which the wellhead pressure, discharge enthalpy and total flow rate are important. Potential of hydrogen (pH) levels and calcium and bicarbonate content are often measured because changes in the composition of the chemical species involved in the formation of calcium carbonate are significant. In addition, dynamic pressure-temperature (PT) records and production tests are performed periodically to keep production data up to date [1].

Well-A is one of the most important wells in the customer’s field, which was completed at the end of 2021. The well, with high enthalpy and high flow capacity, produces in two phases as steam and brine. This well, which contributes 22 MW to the power plant, must be reliably operated because it contributes significant profits to the customer.

When Well-A was put into production, the customer implemented a scale mitigation program to minimize scale-related production losses from this well. We, as experts in this field, were appointed as the preferred partner to provide innovative solutions to the current scale and corrosion issue at the customer’s field. We collected the well chemistry information from the customer and chose the best scale dispersant to solve the problem. Also, we used the best capillary tubing metallurgy for an aqueous, corrosive environment. At the end, we applied our downhole scale inhibitor (DSI program at Well-A and succeeded in preventing scale formation in the well. We started implementing the project on 18 January 2022 and continued through 15 April 2022.

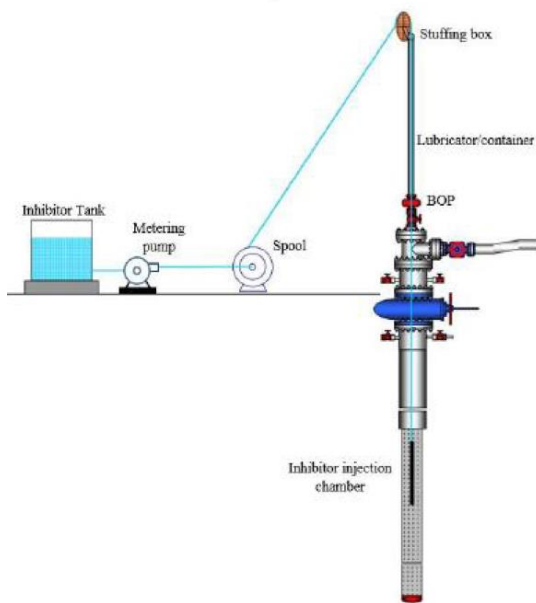


Fig. 1. DSI system installed in production wells [3].

While monitoring the performance of the DSI program, we noted and investigated signs of corrosion at the well. We reported the corrosive tendency of Well-A and several other observations that provided evidence of active corrosion to our customer because this corrosion could impair future well production and result in costly maintenance.

II. PREPARATION FOR DOWNHOLE SCALE INHIBITION (DSI) – DATA COLLECTION AND ANALYSIS

Before we implemented the DSI trial project, we collected from the customer information regarding the chemical and physical data of Well-A. We conducted an extensive and wide-ranging study to determine the suitability of the geothermal well for the implementation of a downhole chemical inhibition system.

By using the two-phase flowing data, the flowing pressure-temperature-spinner (PTS) survey data and the casing tally, we determined the steam zone, transition zone and liquid zone for the calculation of the injection depth and weight of the sinker bar to be used. That calculation was the most important safety aspect of the operation.

After evaluating the non-condensable gas analysis and brine water analysis data, we decided which scale dispersant to use in the well. In addition, metallurgical requirements of the capillary tubing and sinker bar were determined.

The preliminary data collection about the chemical, physical and historical information of the well helped us provide the best operating conditions throughout the project.

A. Two-Phase Flowing Data

In 2021, Well-A, shown in Fig. 2, started to produce approximately 65 kg/s total mass flow, with a flowing enthalpy of approximately 2117 kJ/kg and a wellhead steam fraction of about 58%. According to the information provided by the customer, Well-A produced liquid from the deepest three feed zones and the well was then fed with steam from two shallower feed zones. The ground elevation of Well-A is 1720 meters above sea level.

Depth m MD	Elev mASL	TMF Cont kg/s	Steam Cont kg/s	Pwf bara	Twf degC	Steam Cont %	TMF Contribution %	Preservoir bara	Hres kJ/kg	dP bar	PI kg/s/bar
1140	623	45	45.0	31	235	92%	69%	50.7	2800	20	2.250
1509	272	1	0.6	39	248	1%	2%	63	2000	24	0.041
1680	103	1	0.1	44	255	0%	2%	75	1100	31	0.032
2001	-217	3	0.4	67	255	1%	5%	99	1100	31	0.096
2124	-339	15	2.8	77	273	6%	23%	108	1180	31	0.478
Total		65						Total			2.898

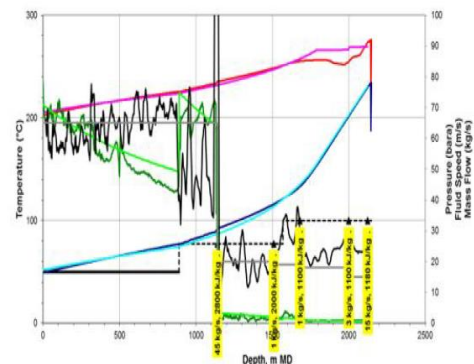


Fig. 2. Two-phase flow characteristics of Well-A.

B. PTS Flowing Data

Flowing pressure survey indicates that liquid flow starting from the deepest depth flashes at approximately 1700 mMD and produces two-phase flow at the surface. Static and flowing temperature surveys, shown in Fig. 3 and Fig. 4, demonstrate that the maximum flowing temperature is the flashing point depth, which is 252 °C and reduces to 190 °C at the surface. Because of the static and flowing PT surveys, we decided to implement the chemical injection within the liquid zone, under 1900 mMD, and the customer agreed. Pressure and temperature values at that depth were used for chemical durability tests in the laboratory to determine the best scale dispersant. Also, these values were used for the design of the dosing systems and to set the monitoring parameters.

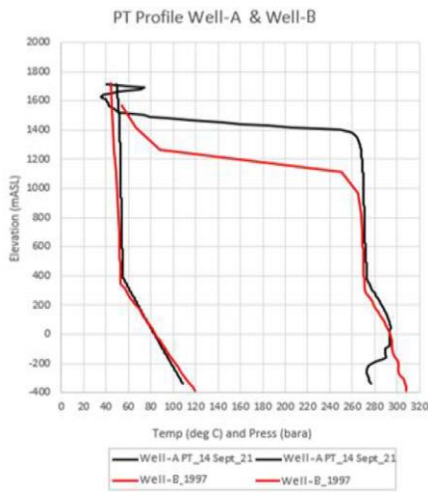


Fig. 3. Static pressure-temperature survey of Well-A (black line).

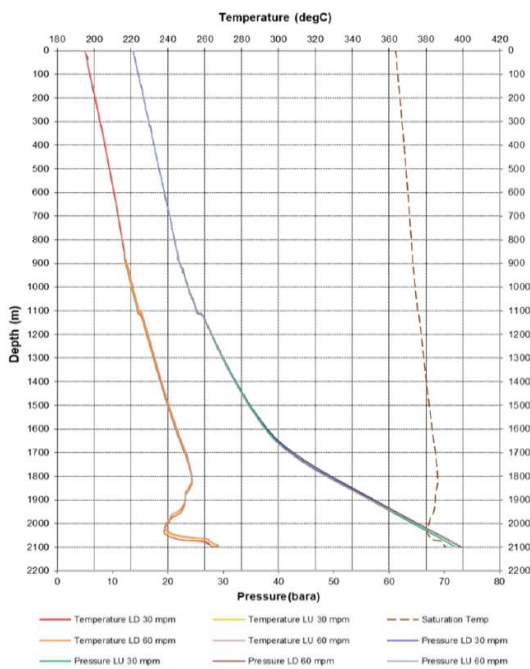


Fig. 4. Flowing pressure-temperature survey of Well-A (Jan 2022).

C. Casing Tally

The schematic of Well-A, shown in Fig. 5, indicates that this well contains a tie-back casing. Generally, tie-back casings are used to fix well integrity problems such as bad-cementing or corrosivity issues. Our capillary tubing was set at 1900 mMD in an 8.625-inch Production liner-2. Diameter information is used for the sinker bar calculations. Tally information is used for the run-in hole and pull out of hole (RIH-POOH) speed plan and safety of the operation.

D. Non-Condensable Gas Analysis Data

We collected two samples of gas analysis reports from the customer in 2021. In the gas analysis report of Well-A that is shown in Fig. 6, non-condensable gas (NCG) consisted mainly of carbon dioxide, which is typical in most geothermal wells. Also, the presence of hydrogen sulfide was relatively low. However, because gaseous corrosivity should generally be taken into consideration in geothermal applications, we chose nickel-chrome-molybdenum metallurgy for the capillary tubing.

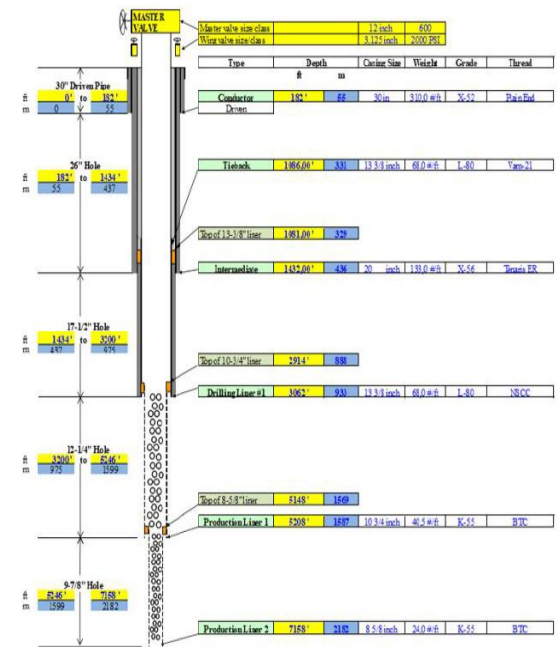


Fig. 5. Well schematic and casing tally of Well-A.

Gas Analysis Report

Type of sample: Gas
 Sampling date: 28-Jul-21
 Wellhead press.: 16 barg

Component	Dry gas (mole%)	n.mole/100mole H ₂ O	Gas in steam (wt%)	Method
Carbon Dioxide	9.36E+01	9.42E+02	2.30E+00	Titrimetric
Hydrogen Sulfide	2.39E+00	2.40E+01	4.55E-02	Iodometric
Ammonia	8.59E-01	8.62E+00	8.16E-03	Ion Selective Electrode
Nitrogen	2.70E+00	2.71E+01	4.21E-02	Gas Chromatography
Methane	2.09E-02	2.10E-01	1.87E-04	Gas Chromatography
Helium	2.05E-02	2.06E-01	4.58E-05	Gas Chromatography
Hydrogen	1.87E-01	1.88E+00	2.10E-04	Gas Chromatography
Argon	2.07E-03	2.08E-02	4.62E-05	Gas Chromatography
TGG			2.400	Calculation

Fig. 6. A gas analysis report of Well-A for preparation of DSI project (Jul-2021).

Water Analysis Report

Type of sample: Separated water
 Sampling date: 23-Jul-21
 Wellhead press.: 16 barg

Component	Value	Unit	Method
pH	4,807		pH (Electrometric)
SiO ₂	-	mg/kg	Spectrophotometric
B	392,983	mg/kg	Titrimetric with Mannitol
Fe	-	mg/kg	Spectrophotometric
Li	0,068	mg/kg	Ion Chromatography
Na	7619,326	mg/kg	Ion Chromatography
K	1495,240	mg/kg	Ion Chromatography
Ca	117,337	mg/kg	Ion Chromatography
Mg	79,928	mg/kg	Ion Chromatography
F	0,037	mg/kg	Ion Chromatography
Cl	9798,009	mg/kg	Ion Chromatography
SO ₄	7388,552	mg/kg	Ion Chromatography
HCO ₃	8,494	mg/kg	Titrimetric
TDS	26506,99	mg/kg	TDS (Electrometric)

Fig. 7. A water analysis report of Well-A for preparation of DSI project (Jul-2021).

E. Brine Water Analysis Data

Fig. 7 shows a water analysis report of Well-A before the implementation of the DSI project.

Based on a simple equilibrium model, the wellhead brine was at saturation with respect to amorphous silica, indicating that amorphous silica deposition was not expected under these operating conditions in the Well-A well-bore or wellhead, but silica deposition could occur at relatively lower temperatures within the downstream of the power plant system (e.g., after flashing to lower pressure/temperature or possibly at the re-injection well). The low fluid pH would cause delay silica precipitation kinetics. Thus, indications of silica deposition in the well bore and wellhead may be expected rarely, only in transient conditions such as well start-ups or shutdowns.

We used a program to model the downhole conditions, where steam and brine was mixed to equilibrium conditions with gasses included at 192 °C. The equilibrium model indicated that calcium was under saturated with respect to calcite. This is commonly observed when calcite precipitation has occurred downhole, depleting the solution in calcium and carbonate alkalinity.

The brine was extremely high in sulfate, and this resulted in the fluid being supersaturated with respect to Calcium sulphate anhydrous. However, the kinetics of anhydrous precipitation were slow; therefore, we did not expect to see anhydrous scale in the well bore or power plant. Amorphous silica was slightly under-saturated at wellhead temperature, but this quickly reached saturation as the brine cooled through the brine piping system, resulting in silica deposition. As expected, calcite was under-saturated, because of the shallow, high enthalpy steam entries. This shallow steam mixes with the deep brine (reservoir pH level was probably about (6–7) and the acidic Carbon dioxide depresses the wellhead brine pH to 4.8. Most likely the deep liquid entries were supersaturated with respect to calcite, resulting in deposition of calcite at the downhole section.

Commonly, a caliper survey can identify the depth and severity of calcite deposition occurring in the well bore. Application of a calcite scale dispersant below the depth of calcite deposition was necessary to mitigate this condition.

In the first technical proposal we submitted to the customer, we warned them about the need for the application of an appropriate corrosion inhibitor that could be considered due to the low pH level (4.8) and the high chloride content. We installed deposit and corrosion coupons at the wellhead during the 3-month trial period. These coupons were analyzed to determine the types and mechanisms of scale deposition and/or corrosion occurring in this area. We promised to report and discuss results with the customer and recommend future actions if required.

After evaluating this information, we chose to use a scale dispersant as the pilot scale inhibitor into the well-bore liquid zone and Inconel 625 for the capillary tubing material. The selected scale dispersant is a proven calcium carbonate scale inhibitor used in hot temperature geothermal wells. Inconel 625 capillary tubing is a high nickel-molybdenum-cobalt alloy material that is durable to aqueous corrosive environments containing high chloride levels and low pH or acidic conditions.

III. IMPLEMENTATION OF THE DSI SYSTEM

Downhole scale inhibition is the process of preventing the formation of scale from blocking or hindering fluid flow through pipelines, valves, and pumps used in oil and geothermal production and processing. Scale inhibitors (SIs) are a class of specialty chemicals that are used to slow or prevent scaling in liquid phase of systems.

a. Installation

The DSI dosing system, shown in Fig. 8, includes:

1. a dosing pump skid, which delivers scale inhibitor to a capillary tubing. a proper chemical storage tank.
2. a proper type of capillary tubing.
3. a pack-off mounted lubricator on the wellhead.
4. a BOP.

The bottom hole assembly, including inhibitor dosing nozzle and weight bars, deployed to the appropriate depth in the well.

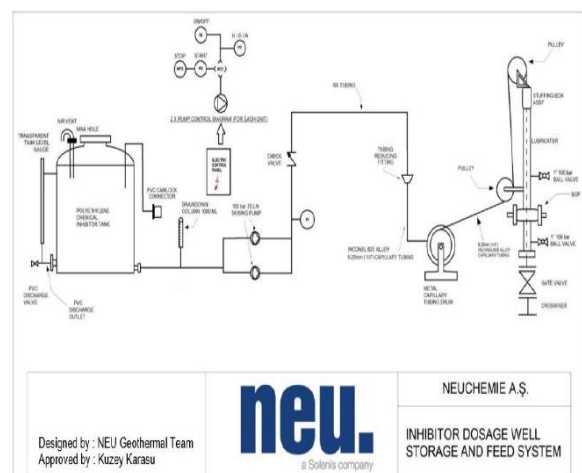


Fig. 8. Inhibitor dosage well storage and feed system for DSI system on Well-A.

The pump skid required to inject the scale dispersant to Well-A was designed specifically for the customer. The skid included two chemical diaphragm metering pumps (max pressure: 100 bars, capacity: 35 liter/h), one 5.000-liter cross-linked polyethylene chemical storage tank, chemical filters, a draw-down tube to measure dosage rate, associated tubing, valves, a dampener (to keep pressure of chemical injection consistently), and complete instruments.

For the chemical storage tank, we used a 5.000-liter capacity, cross-linked polyethylene inhibitor tank, with a 10-mm wall thickness, red colored tank. The tank is equipped with a manual fluid level gauge for easy and continuous monitoring. Inhibitor tank chemical output was made from the side of the tank to the dosing system with appropriate fittings and chemical resistant hoses close to the lower limit. A manhole cover with a 42-cm diameter provided access to the inhibitor tank.

For the capillary tubing, we needed 2200 meters, and we selected Inconel 625 (UNS N06625, B163) seamless tubing with a 0.25inch OD and a 0.035-inch wall thickness. Inconel 625 was selected for this application because it is a corrosion and oxidation resistant nickel alloy with high strength and outstanding aqueous corrosion resistance. Inconel 625 has excellent fatigue strength and stress-corrosion cracking resistance to chloride ions compared to the less expensive alternatives 316L stainless steel or 2205 duplex stainless steel tubing.

To hold the bottom hole assembly (BHA) and capillary tubing in place before the run-in hole (RIH) and after the pull out of hole (POOH) operations, a 16-foot carbon steel lubricator, as shown in Fig. 9, was used at the wellhead of Well-A. The lubricator included a hydraulic stuffing box (sealing box) at the top. To ensure smooth movement of the capillary tubing, two aluminum pulleys (sheaves) were mounted on the lubricator, one at the top and one near the bottom. The upper pulley could be moved in all directions. There was more than one 1-inch OD or ID, 316 stainless-steel, ball type relief valve on the lubricator. A thread-operated BOP was placed under the lubricator to be used in emergency conditions. The BOP had Viton® parts to prevent damage to the capillary tubing when closed. Flange types between the BOP and the wellhead crown valve were synchronized with a crossover sub.



Fig. 9. Lubricator with hydraulic stuffing box and crown pulley on the wellhead of Well-A.

TABLE I. SCALE DISPERSANT DILUTION AND DOSAGE TABLE OF WELL-A

ppm	Flow (kg/s)	Neat (g/m in)	Chem density (g/cm ³)	Concentration (%)	SoL Density (g/cm ³)	Neat (ml/min)	SoL (ml/min)	Time for 200 cc (s)
50	65	195	1,2	16,67	1,03	188,7	1132	10,6
40	65	196	1,2	16,67	1,03	151	905,6	13,3
35	65	136,5	1,2	16,67	1,03	132,1	792,4	15,1
30	65	117	1,2	16,67	1,03	113,2	679,2	17,7
25	65	97,5	1,2	16,67	1,03	94,4	566	21,2
20	65	78	1,2	16,67	1,03	75,5	452,8	26,5
15	65	58,5	1,2	16,67	1,03	56,6	339,6	35,3
10	65	39	1,2	16,67	1,03	37,7	226,4	53
5	65	19,5	1,2	16,67	1,03	18,9	113,2	106

From top to bottom, the 13-foot bottom hole assembly (BHA) consists of a 6-inch stainless-steel capillary tubing holder, a 7-foot tungsten hollow bar, a 5-foot stainless-steel solid bar and a 6-inch stainless-steel bull-nose.

The scale dispersant selected for the control of calcite and other calcium scales in Well-A is a proven polymer blend that effectively inhibits precipitation of calcium carbonate, calcium oxalate, calcium sulfate and other low solubility salts. It has excellent chelation, low threshold inhibition and lattice distortion ability. In geothermal brine, it reduces scale formation, particularly for calcium carbonate. We conducted a thermal stability test of the scale dispersant to assure its performance in hot temperature and pressure well conditions.

The scale dispersant was diluted in 1:4 scale dispersant/dilution water and applied to the well-bore at a depth of 1900 mMD. The dosage rate was measured continuously by using a gradual cylinder, calculating the time of 200 cc consuming on a gradual cylinder. Table I shows detailed information regarding the application of the scale dispersant.

b. Monitoring

Proper monitoring program is essential to ensure that the DSI trial program were successfully. Along the trial process we collect data from brine water analyses and scale coupon analysis.



Fig. 10. Sampling point location (left), on-site sampling process (center) and on-site lab support (right).

1) Brine analysis monitoring

Water samplings were collected from the water phase from the flow line. To achieve accurate results, the best point on the pipeline was selected, as shown in Fig. 10. A sampling mini separator was installed, and the pressure and temperature of the separator was adjusted according to the flow. This way, flow-line simulation could be achieved within the separator. We prepared two sets of samples for separate analysis by our laboratory scientists and by our customer, and then shared our results.

The exact required dosage was established during the field test. This was determined and optimized within a few days of start-up. The optimization process was started with the trial using a maximum of 50 ppm, and all dosages of 10, 20, 30 and 40 ppm were tried every 2 days. At the end of the optimization process, an 8-ppm dosage was determined to be the optimum rate. The detail analysis result will be seen on the Fig. 12.

2) Scale coupon monitoring

In Well-A, we conducted a scale coupon analysis, to examine the results of scaling as another effective way. We saw the scaling and corrosion effects of the Well-A, visually and numerically with the scale coupon analysis. Since the beginning of the project, we had been taking photos of the scale coupon to collect evidence of scaling on the coupon.

Benefits of the visual observation of the coupon included observing any traces of:

1. scaling, which allowed us to maintain a double-check for chemical injection optimization.
2. plugging holes, which allowed us to see if anything else was produced from the well-bore.
3. corrosion, which allowed us to understand the type of corrosion.

The scale coupon, as shown in Fig. 11, that was used in Well-A for the DSI Trial project had a carbon steel tip.

We determined the sampling frequency of the scale coupon as more frequently of the DSI chemical treatment project. That time interval was the optimization period of the chemical dosage. Then, we decreased the frequency of analysis.



Fig. 11. Scale/corrosion coupon used in Well-A for the DSI project.

IV. BRINE ANALYSIS RESULTS FOR WELL-A

Throughout the project, we recorded the results of chemical sampling analysis and created a trend-line of the calcium removal performance, shown in Fig. 12, of the scale dispersant in Well-A. Within the 84-day period between 21 Jan to 15 April 2022, we managed to remove 40.24 tons of calcium from the system. Currently, we have no proper way to measure the calcite deposition rate in the system because no standardized method exists to predict or measure the scale deposition on the metal surfaces of geothermal wells. However, what we could do and predict was the mineral removal amount from the system based on hardness level analysis. In our case, the scaling mineral is a calcium-based scale.

Throughout the project, calcium hardness levels were in a decreasing trend-line, although the scale dispersant dosage rate was stable at 8 ppm. To determine whether the decreasing trend-line was independent of the chemical treatment, we also looked at the conductivity level trend-line of the geothermal fluid. The trend-line angle of the conductivity was the same as the trend-line angle of the calcium hardness, as shown in Fig. 13. These results prove that the scale dispersant still was able to prevent calcium scaling at its optimum rate.

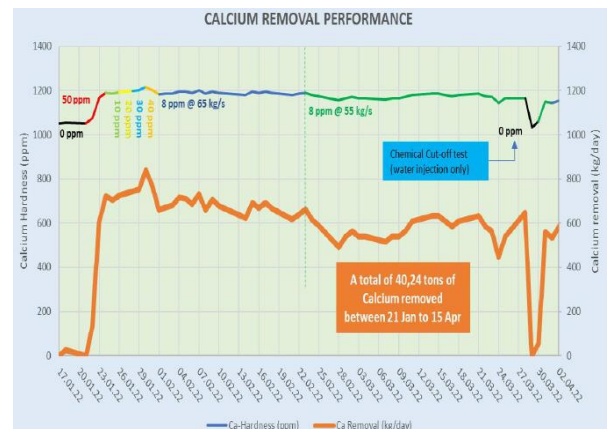


Fig. 12. Calcium removal performance of scale dispersant in Well-A.



Fig. 13. Calcium hardness versus conductivity values, proving the decreasing trend is natural.

V. CONCLUSION

In January 2022, Solenis embarked on a joint project with a customer to fix the scaling problems in Well-A in the customer's geothermal field in Indonesia. As agreed by both parties, the project was named the downhole scale inhibition program (DSI) and preparations were started. Input data, including gas chemical analysis, water chemical analysis, historical information, feed zone data, well schematic, well static, and flowing pressure-temperature-spinner (PTS) surveys were collected. Using the data collected from the customer, Solenis completed the calculations and material selections and then supplied the necessary subsurface and surface equipment for the DSI project in Well-A.

During the DSI project, we successfully mitigated calcium scale in Well-A by removing from the system a total of 40.24 tons of potential calcium carbonate in the downhole system.


REFERENCES

- [1] Jacob, P., Guerra, E., Cartagena, H. and Hernández, B.: Calcite Inhibition in The Ahuachapan Geothermal Field, El Salvador, Proceedings, Presented at "Short Course on Geothermal Development and Geothermal Wells," Santa Tecla, EL SALVADOR (2012).
- [2] Problems in Geothermal Operation-Scaling and Corrosion, Einar Gunnlaugsson, Halldór Ármannsson², Sverrir Thorhallsson² and Benedikt Steingrímsson² I Orkuveita Reykjavíkur (2014).
- [3] Pereira, V.V.: Calcium Carbonate Scaling Control in Geothermal Well Pv8 in Sao Miguel, Azores, Combining Chemical Inhibition and Mechanical Reaming, Geothermal Training Program 33, (2014).
- [4] Corrosion and Scaling, Nikos Andritsos, Pierre Ungemach, Petros Koutsoukos, "Short Course VI on Utilization of Low- and Medium-Enthalpy Geothermal Resources and Financial Aspects of Utilization," organized by UNU-GTP and LaGeo, in Santa Tecla, El Salvador, March 23-29, 2014.



**The 3rd AEMT
Center of Excellence
in Science and Technology "Geomagnetic"**

Contact:

 Building B 3rd Floor Engineering Faculty,
University of Mataram, West Nusa Tenggara - Indonesia
 <https://aemt-geomagnetic.org/aemt/>
 aemt@unram.ac.id

